Synthesis of hydroxyapatite-based nanocomposites and their application in electrochemical sensors

Feng Gao

September, 2017

Shimane University, Japan

Synthesis of hydroxyapatite-based nanocomposites and their application in electrochemical sensors

CONTENTS

Abstract of the Thesis

Electrochemical sensors are a type of modern devices that can effectively transforms the molecule recognition events into the detectable electronic signals. Due to their advantages of remarkable detectability, experimental simplicity and low cost, they have found a number of interesting applications in the areas of environmental, industrial, food and clinical analyses. With the development of nanoscience and nanotechnology, it is found that the reasonable incorporation of nanomaterials into electrochemical sensors can greatly enhance the analytical performance of the sensors. Hydroxyapatite (HAp) is a calcium phosphate similar to the human hard tissues in morphology and composition, and the nanosized HAp presents some outstanding properties like good biocompatibility, high stability, rich active sites, and so on, which enable it can be served as an excellent nanomaterial for electrochemical sensing application. In this thesis, the nanosized HAp and its composites with carbon nanotubes (CNTs) and graphene were synthesized, and then be utilized as electrochemical sensing materials for the selective and sensitive determination of heavy metal ions, drug molecule of luteolin, and industrial pollutant of hydrazine.

The thesis consists of 5 chapters, and the abstracts of each chapter are mentioned as follows.

Chapter 1: The brief introduction of electrochemistry; calcium hydroxyapatite; carbon material were described. Moreover, some questions of the previous studies were pointed out and the significance and purpose of this study were stressed.

Chapter 2: The uniform rod-like HAp particles were synthesized through a simple wet method, which was characterized by X-ray diffraction (XRD), Fourier-transform infrared (FTIR) and transmission electron microscopy (TEM). The composite of HAp-Nafion was then prepared and used as a matrix for simultaneous determination of Hg^{2+}, Cu^{2+}, Pb^{2+} and Cd^{2+} by differential pulse anodic stripping voltammetry (DPASV). The good dispersibility, large specific surface area, rich active sites, and strong adsorption property of the composite contributed to the enhanced stripping signals of the four heavy metal ions. Under the optimized experimental conditions, the calibration curves for Hg^{2+} covered two linear ranges from 0.1 to 1.0 μM and from 3.0

to 10.0 μM. For Cu^{2+}, Pb^{2+} and Cd^{2+}, the linear calibration curves ranged from 0.1 μM to 10.0 μM. Based on a signal-to-noise ratio characteristic of 3, the detection limits of Hg^{2+}, Cu^{2+}, Pb^{2+} and Cd^{2+} were estimated to be 0.030 μM, 0.021 μM, 0.049 μM and 0.035 μM, respectively. The developed method was also utilized for the detection of Hg^{2+}, Cu^{2+}, Pb^{2+} and Cd^{2+} in real water samples, and satisfactory results were obtained.

Chapter 3: A nanocomposite of HAp-CNT was synthesized by in-situ transformation of CNT-calcium phenyl phosphate (CaPP) with the assist of enzyme such as alkaline phosphatase at pH = 9 and 37°C. The nanocomposite was characterized by XRD, FTIR and TEM. Then the HAp-CNT was cast onto a glassy carbon electrode (GCE) and used as a sensing platform for the electrochemical determination of luteolin. The electrochemical experiments indicated that the HAp-CNT modified GCE (HAp-CNT/GCE) could greatly enhance the electrochemical response of luteolin. A series of experimental parameters including the type and pH value of supporting electrolyte, accumulation time and accumulation potential were optimized. The electrochemical parameters such as electron transfer rate constant and electron transfer coefficient of luteolin at the HAp-CNT/GCE were also investigated. Under the optimal conditions, the reduction peak currents presented a good linear relationship with the concentration of luteolin in the range of 4.0×10^{-7} to 1.2×10^{-5} M. The detection limit was estimated to be 8.0×10^{-8} M.

Chapter 4: Chemical reduction and thermal treatment are the most promising approaches for large-scale synthesis of graphene. However, the toxic/hazardous reducing agents or large energy consumption are necessary for these two methods. In this work, it is unexpectedly found that, the in-situ growth of HAp on graphene oxide (GO) under a moderate temperature (85°C) can effectively trigger the reduction of GO, which is testified by XRD, FTIR, electronic adsorption spectra, Raman spectroscopy and electrochemistry. Such a reduction process needs neither extra reducing agents nor high-temperature thermal treatment. The TEM experiment further demonstrates that the rod-like HAp nanoparticles are uniformly attached on the surface of reduced GO

(rGO) to form the composite. Electrochemical sensing assays show that the synthesized HAp-rGO nanocomposite presents excellent electrocatalytic capacity for the oxidation of a toxic reducing agent of hydrazine. Based on this, an electrochemical sensor for hydrazine detection was developed, which displays outstanding performance in the index of low fabrication cost, short response time ($\sim$ 2 s), wide linear range (2.50×10^{-6} M$\sim$$1.16\times10^{-3}$ M), low detection limit (4.27×10^{-7} M), and good selectivity. When the sensor was utilized for detection of hydrazine in real water samples of industrial wastewater satisfactory results were achieved.

Chapter 5: Conclusions and scope of these studies were described.

Chapter 1

General Introduction

1.1 Background and introduction

1.1.1 Electrochemical Sensor

Electrochemical methods have been regarded as one of the most promising techniques in analytical chemistry due to their many advantages of less expensive, more selective and high sensitive, highly reproducible and less time consumption. Glucose biosensors used widely in glucometers and pH electrodes are the important and known examples of the electrochemical sensors. In general, electrochemical sensors include two basic components, *i. e.*, a chemical (molecular) recognition system and a physicochemical transducer [1]. The recognition system is the most critical part for an electrochemical sensor, since all the sensing chemical reactions occur at this part, which decides the performance of a sensor such as sensitivity, specificity, linear range, response time, and so on. The transducer is a device that converts the chemical recognition response into a signal that can be detected by modern electrical instrumentations composed of a biological recognition element, the so-called bioprobe (of either a DNA single strand, an enzyme, a protein, and so on) which is properly conjugated with a transducer component that converts biomolecular interactions into signals. The sensing process can be illustrated as Scheme 1.1. As seen, when the target analyte in the sample approaches and adsorbed by the recognition layer, the microenvironment of the sensing interface was changed, and thus the transducer can respond to the event and transformed it to the measurable electrochemical signals.

Scheme 1.1 Illustration for the constitution and working principle of an electrochemical sensor.

In addition, to obtain readable sensing information, the electrochemical analyzer is linked to a three-electrode system, namely the working electrode that contains the recognition system and the physicochemical transducer, the reference electrode (such as Ag/AgCl, saturated calomel electrode) that act as reference in measuring and controlling the working electrode's potential, and the auxiliary electrode (such as Pt wire) that passes all the current needed to balance the current observed at the working electrode.

Therefore, the working electrode is the core part in an electrochemical sensor, which usually adopts precious metal (gold, platinum), carbon with different forms (*i.e.* glassy carbon, pyrolytic graphite, graphite powder) as the basic material. However, the limited specific area, less active sites and weak adsorption of these conventional working electrodes always lead to poor recognition ability and high over-potential, which will greatly lower the performance of the electrochemical sensor. In contrast, the use of the chemical modified electrodes can greatly improve the efficiency of accumulating target analytes without interference from other species. Much effort has been devoted in developing advanced materials that have outstanding electrochemical properties to modify common working electrodes [2-6].

1.1.2 Application of nanomaterial in electrochemical sensors

Nanomaterials refers to the materials which have the feature unit of 1-100 nm, encompassing from quantum dots, nanoparticles, nanowire, nanorods and graphene to carbon nanotubes. They have a nanometer scale length in at least one-dimension, and due to their size, exhibit distinctively different properties from bulk materials, resulting from the quantum size effect. Their unique electric, optical, thermal and magnetic properties are determined by the dimensionality. According to difference of the elementary units, nanomaterials are usually grouped into three categories:

Zero dimensional (0-D) nanometer materials: the material have a nanometer scale length at three-dimension *i. e.* quantum dot, atomic cluster.

One dimensional (1-D) nanometer materials: the material have a nanometer scale

length at two-dimension *i. e.* nanowire, nanorod, and nanotube that were all called nano-fibre.

Two dimensional (2-D) nanometer materials: the material have a nanometer scale length at one-dimension *i. e.* ultrathin film, multilayer film, superstructure. Among all the nanomaterials, 2-D nanomaterial has oldest and mature nanotechnology and is the basis for synthesis other dimensional materials.

Because of their structure features of high porosity, small size, and active surface area, nanoscale materials present many novel properties such as surface effects, volume effect, quantum size effect, macroscopic quantum tunneling effect etc., and they were widely used in various fields such as electronics, chemical engineering, nuclear technology, aviation, light industry, medicine and so on.

Over the recent decades, numberous nanomaterials have also been widely employed as modifier in electrochemical sensor. During the detection process, these nanomaterials exhibit great effective catalytic activity, fast electron transfer kinetics, active large surface area, and control over the microenvironment of electrodes [7]. For example, metal-based nanomaterials have excellent catalytic properties combining the intrinsic catalytic properties of the metal with the nanoparticulate properties of high surface area/volume ratio. The introduction of nanoparticles with catalytic properties into electrochemical sensors and biosensors can decrease over potentials of many analytically important electrochemical reactions, and even realize the reversibility of some redox reactions, which are irreversible at common unmodified electrodes. For instance, Co-CeO$_2$ nanoparticles has been synthesized and applied for discrimination and simultaneous determination of xanthine, hypoxanthine and uric acid as an efficient promoter to enhance the kinetics of the electrochemical process [8]. R. Ahmad group have fabricated ZnO modified electrode for detection of hydrazine, and the sensor showed an excellent sensitivity, long-term stability, and good reproducibility [9]. S. H. Kim et al. have prepared rose-like CuO nanostructures and used as effective electron mediators to fabricate highly sensitive non-enzymatic glucose sensor which shows very high sensitivity of ~4.640 μA mM^{-1} cm^{-2} and an experimental detection limit ~0.39 mM with correlation coefficient (R) of 0.9498 in short response time [10].

9

Some of the non-metal nanoparticles that have special catalytic properties can also been applied in electrochemical analysis systems. For example, graphene (GR)-based nanoparticles have been widely used for modification of electrochemical sensor. As a typical 2-D nanomaterial, GR exhibit excellent electrical conductivity, large theoretical specific surface area, and strong mechanical strength in detection of various analytes. T. Wu group have synthesized graphene/palladium nanoparticles and applied it in electrochemical sensor for detection of triclosan [11], A. Afkhami group synthesized zinc ferrite/graphene nanocomposite and used it as a modifier for fabrication of a sensitive electrochemical sensor for determination of omeprazole in real samples [12]. M. Cheng group have prepared graphene-molybdenum disulfide and modified it on the electrode for highly sensitive detection of dopamine [13], C. Zhang et al. have prepared Graphene-Supported Tin Oxide Nanocluster and used it as sensing material for nonenzymatic detection of hydrogen peroxide. [14]. Carbon Nanoture (CNT)-based nanocomposite is another extensively used non-metal nanoparticle in electrochemical sensor. As a typical 1-D nanomaterial, CNT shows excellent unique properties such as thermal conductivity, unique electronic properties and thermal stability. M. Elyasi group have prepared Pt/CNTs nanocomposite and modified it on carbon paste electrode for determination of Sudan I in food samples. [15] Y. Liao et al. have fabricated Nbim/CNT composite modified electrode for selective determination of luteolin in the flavonoids [16]. T. Madrakian group have prepared Fe_3O_4 nanoparticle/multiwall carbon nanotube-modified glassy carbon electrode for determination of rizatriptan benzoate in real samples [17].

1.1.3 HAp and its nanocomposites

Hydroxyapatite (HAp) is a mineral form of calcium apatite with the formula $Ca_{10}(PO_4)_6(OH)_2$. The chemical composition of HAp is similar to natural bone such as teeth and bones in human and animal organism. So it is well kwon as an important material for biomedical implants. The crystal structure of HAp belongs to hexagonal ($P6_3/m$) or monoclinic ($P2_1/b$) crystal structure, with the parameters of unit cell of

a=b=0.942 nm, c=0.6882 nm, containing 10 Ca^{2+}, 6 PO_4^{3-} and 2 OH^- ions [18] (Fig. 1. 1). Also, it can be seen that the HAp crystal grows toward **a** and **b** axes or, **c** axis, and the **ac** or **bc** face and **ab** one possess different atomic elements, numbers and arrangements, and thus the morphology of synthetic and natural HAp materials is commonly rod-like of plate-like shape. On the other hand, because the **ac** or **bc** face and **ab** one of HAp have different crystal structure, so the different crystal face exposing on the particle surface presents various property. Thus, the controlling of the morphology of HAp particles is an important factor to use this material in various applications.

The methods for synthesis HAp particles are generally classified to two groups. One is called solid phase reaction method and the other is called wet phase reaction method including tiny latex methods, hydrothermal methods, sol-gel methods, liquid-phase deposit methods and electrodeposited methods. The characteristic of HAp depends on the method of synthesis which influences particle size distribution and morphology. For the dry process via the solid phase reaction reported by Yoshiota group [19]:

$$(CaPO_3)_2 + 4Ca(OH)_2 = Ca_{10}(PO_4)_6(OH)_2 + CaO$$
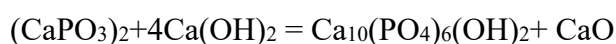
the particle shape becomes irregular and the size of this material is very big (> 1 mm). Hence, the wet processes such as tiny latex methods, hydrothermal methods and sol-gel methods are widely used for preparation of regular and nanometer HAp particles. Based on this, T. Hattori group have prepared HAp with a diameter of less than 200 nanometers using hydrothermal methods by mixing CaO and calcium pyrophosphate as precursor solution [20]. S. Bose et al. have synthesized needle shape spherical morphology of HAp nanopowder by emulsion technique [21]. D. W. Kim group have prepared large-scale HAp nanoparticles by in situ crystallization process using a fairly simple reaction of $Ca(OH)_2$ and H_3PO_4 [22].
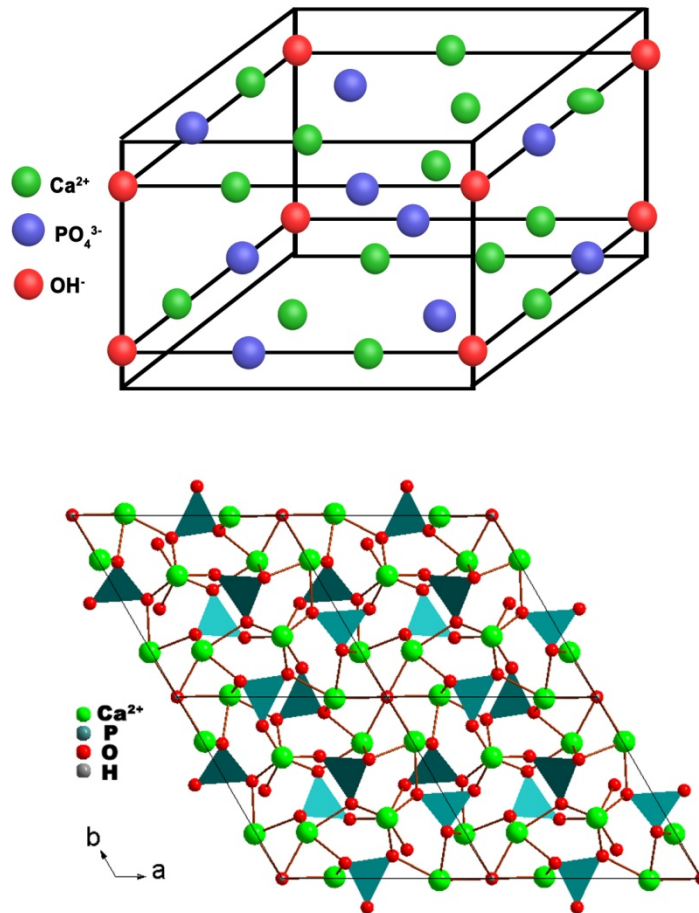
Fig. 1.1 Illustration of (A) crystal structure of HAp and (0001) surface

structure in the projection of hydroxyapatire.

Generally, preparation of highly crystalline HAp particles is required at high temperature above 80 ℃. On the contrary, in human body HAp with high crystallinity is produced at 37 ℃ and pH = 7.4. This process fully copy the human body for generating the new bones, and the fact is very interesting. But the detail of the formation mechanism is very complex, and till now there is no very clear discussion on it.

During the last decades, HAp or HAp-based composite has been widely applied in various areas due to their easy preparation, stereoscopic structure, excellent biocompatibility, rich active sites, good ion-exchange and adsorption capacity. For example, Hokkanen's group have prepared HAp microfibrillated cellulose composite and applied it as a potential adsorbent for the removal of Cr (VI) from aqueous solution [23]. Opre et al. synthesized Ru-HAp nanocomposite and used it as catalyst for the fast and highly selective oxidation of alcohols with oxygen [24]. P. N. Lima group has synthesized magnesium-calcium/hydroxyapatite (Mg-Ca/HA) composites with enhanced bone differentiation properties and applied it as filling material in orthopedic surgery [25].

In recent years, based on the regular three-dimensional structure, rich active sites and excellent biocompatibility, the nanosized HAp have also been synthesized and utilized as functional materials in fabrication of modified electrodes in electrochemical sensor..Kanchana et al. have fabricated a HAp nanoparticles modified electrode and used it for the electrochemical determination of uric acid [26]. And they also developed a HAp modified sensor for electrochemical detection of folic acid [27]. But the poor tensile strength, fracture toughness, and low electronic conductivity of pure HAp crystals limit their application in wider detection species. One approach for address these problems are to adopt other materials *e. g.* polymers [28, 29], carbonaceous nanomaterial [30], metal/metal oxide [31], or organic molecule [32] as modifier to enhance the performance of HAp.

1.1.4 Carbon nanomaterials of graphene and carbon nanotubes

There is an attractive and fascinating family called carbon-based materials. In this family, various members have their distinct character including the naturally abundant and cost-effective graphite, and also the most rare and valuable diamond. When a new member is discovered in this family, a revolutionary progress will be made in material science and technology, *e. g.* fullerene in 1985 [33], carbon nanotubes (CNTs) in 1991 [34] and graphene in 2004 [35]. Till now, carbon-based materials refer to carbon black, graphite, graphene, CNT, and fullerene. These materials are not isolated from each other, but in close relationship. For example, graphene, the latest member in this family, is an atomically thick, two-dimensional (2-D) sheet, regarded as the building block of all other graphitic carbon allotropes with different dimensionality [36]. 3-D graphite is made of graphene sheets stacked on top of each other with a spacing distance of 3.37 Å; 1-D CNT may be made by rolling graphene sheets; 0-D fullerenes (buckyballs) may be envisioned to be made by wrapping a part of graphene sheet (0-D refers to the lack of translational symmetry in any dimension). Due to their extraordinary intrinsic properties and ability to be dispersed in various polymer matrices, carbon-based materials have been widely used in fabricating polymer compos-ites/nanocomposites in order to improve the mechanical, thermal, gas barrier, conductivity, and flame retardant performances. Especially, with high specific surface area, subtle electron properties and abundant surface atoms, they have shown great potentials in the applications of bioelectronics devices such as electrochemical biosensors, field effect transistor base biosensors, piezoelectric devices, and super capacitors.

Carbon Nanotubes (CNTs), as one of the most important nanomaterials with one-dimensional and hollow structure have attracted much attention since they were discovered by Iijima in 1991 [34]. A great deal of investigations has been carried out to explore the potential applications of CNTs since then. Up to date, due to the unique electronic properties, excellent thermal conductivity, thermal stability and high mechanical strength, CNTs have attracted worldwide attentions in various fields

including materials science [37], transistors [38], sensors [39], energy storage [40] and field-emission display [41]. The excellent characters make CNTs ideal candidates to enhance stiffness, strength and electronic conductivity of the composite materials. As a result, CNTs are also expected for the fabrication of biosensors and electrochemical sensors [42, 43].

Graphene is another representative of the carbon-based family nanomaterials. In fact, the existence of graphene has been theoretically studied for many years and was thought to be impossible until it was actually made by "scotch-tape" method in 2004 [35]. Therefore, the primeval synthesis method of graphene is mechanical exfoliation, which can produce the best quality of graphene in terms of structural integrity. However, this technique is only limited for scientific research due to its uncontrollable, thus large scale production and applications are limited. In recent years, a lot of research has been done for large-scale preparation of graphene using chemical vapor deposition or reduction of graphene oxide (GO) solutions. GO is typically synthesized through a Hummers' method invented many years ago [44] or other modified method based on it [45]. Generally speaking, graphite powders are first oxidized by severe chemical energy. This process was quite easy because of the interaction of water with the oxygen-containing functional groups (such as epoxide and hydroxyl) introduced during the oxidation process. Then, GO can be substantially reduced to graphene network by chemical reducing agents treatment, which is usually referred as reduced graphene oxide (rGO) [46]. Up to date, lots of strategies including electrochemical reduction, microwave irradiation, photocatalytic reduction, thermal treatment and chemical reaction have been developed for the transformation of GO to the reduced counterpart. Among these methods, the chemical reduction based on the reducing agents of hydrazine or hydrazine hydrate is mostly utilized, since the synthesis route of such method is mature, and the reduction efficiency by the method is relatively high. However, the reducing agents of hydrazine and its derivative are highly toxic and explosive. Therefore, the development of highly effective and environmental-friendly approach to prepare rGO is still of great challenge.

1.2 Research purpose

1.2.1 Electrochemical sensor for environmental pollutants

In the last decades, due to the industrial globalization and the rise in population, the increasing amount of hazardous compounds that have high impact on human well being and environmental health have been of increasing concern.

Among them, the pollution to water by the release of heavy metals into ecosystem has been causing worldwide concern because of their toxicity and potential accumulation in living creatures. As a result, the heavy metal ions entered food chain and contaminate the ecosystem. Many tragedies such as Minamata poisoning, Bhopal disaster, arsenic poisoning, and Sandoz disaster [47] are some of the historic evidences for the loss of human lives and economy due to the consumption of metal ion contaminated water. In view of these disasters, organizations such as Centre for Disease Control (CDC), International Agency for Research on Cancer (IARC), World Health Organization (WHO) have put forth limitations in permissible levels for various heavy metal ions [48-50]. Intake of heavy metal ions beyond these permissible levels lead to reproductive toxicity, respiratory disorders, impaired neurologic development, cardiovascular diseases, and pulmonary fibrosis and behavioural issues [51]. Hence, rapid and reliable detection of these heavy metal ions in water sample is of great emergency.

Among the heavy metal pollutants, lead (Pb), mercury ion (Hg), cadmium ion (Cd), and copper ion (Cu) are the four most common heavy metal pollutants; presence of which even in low concentrations (sub micro-molar range) can be severely dangerous to human health. Living beings can be exposed to these heavy metal ions while coming in contact with contaminated air, water, soil etc., which can cause acute deathly diseases and other health problems. For example, accumulation of Pb^{2+} in the human body has diverse detrimental effects on human health as it can induce renal tumors, increased blood pressure as well as neurological and behavioral effects [52,

53]. Pb^{2+} has even more severe effects in children during their developmental stage, as it leads to reduced intelligence and other neuropsychological defects [54]. Mercury is the best-known and most puzzling heavy metal pollutants in the environment [55]. It is a causative agent of various sorts of disorders, including neurological, nephrological, immunological, cardiac, reproductive and even genetic. The US Environmental Protection Agency (EPA) has set the concentration limit of Hg^{2+} down to 10 nM in drinking water [56]. Cd^{2+} ions are also known to be carcinogenic and exposure of this to human body can cause toxic $OH°$ radical formation which can lead to cancer [57]. Cu^{2+} is an essential element to human bodies, but the excessive copper can seriously destroy tissue since it can interact with lipid hydroxyperoxides to produce some DNA-damaging agents such as malondialdehyde and 4-hydroxynonenal [58]. Therefore, development of simple detection technique which can detect and quantify those environmental hazards is of great importance to the scientific community. Considering the above mentioned, permanent effective control over the presence of these compounds in the environment and foodstuff appears to be extremely important for nature protection and improvement of life quality. Conventional methods of high-precision analysis of heavy metals, *i. e.* gas and liquid chromatography, spectrophotometry, numerous chemical and physical techniques, require high-skilled personnel, complex and expensive equipment [59]. Besides, complicated sample pretreatment is necessary that makes the procedure more time- and costs-consuming. That is why, the development of easy-to-use, accurate, selective, fast and cheap method of analysis of heavy metal concentration in the samples of ambient environment and foodstuff appeared at present to be such actual problem.

Hydrazine (N_2H_4) is another one of the most poisonous chemical material which is widely used in the fields of corrosion inhibitor, antioxidant, dynamite, emulsifier, pesticide and insecticide, rocket fuels, and so forth [60-62]. It is water-soluble, volatile and colorless liquid which has strong reducibility and corrosivity [63]. Large amount use of N_2H_4 that leads to short and long-term exposure to related potential hazards could cause damage to all living races and environment. N_2H_4 is can be easily

absorbed by oral, dermal, and inhalation routes of exposure, which may result in the irritation of throat, nose and eyes, headache, nausea and coma in humans. Furthermore, it is harmful to the central nervous system, lungs, liver, and kidney, and N_2H_4 is corrosive that may produce dermatitis from skin contacts in humans and animals. Presently, many countries have formulated the drinking water standard according to the content of hydrazine for example the EPA identified hydrazine as a potential carcinogen with a threshold limit value of 10 ppb [64]. Due to all the damages N_2H_4 may cause, it is of great importance to develop a simple, accurate, inexpensive and reliable method to determinate N_2H_4.

1.2.2 Electrochemical sensor for medicine

There are many kinds of pharmic molecules *i. e.* dopamine, ascorbic acid, luteolin etc., which exhibit a wide variety of biochemical and pharmacological effects including antioxidant free-radical scavenging, anti-inflammatory, anti-carcinogenic and other beneficial properties on human health. For example, dopamine plays a significant role in the function of the central nervous, renal and hormonal system as an important neurotransmitter [65]. Ascorbic acid, also called vitamin C, is a vital vitamin in human body and it has also been used for the treatment of mental illness, cancer, common cold, infertility and for improving the immunity. Luteolin, 3', 4', 5', 7-tetrahydroxyflavone, is a common flavonoid that exists in many types of plants including fruits, vegetables and medicinal herbs [66]. The pharmacological activities of luteolin could be functionally related to each other. For instance, the anti-inflammatory effect of luteolin also may be linked to its anticancer function. The anticancer property of luteolin is associated with inducing apoptosis, which involves redox regulations, DNA damage, and protein kinases in inhibiting proliferation of cancer cells and supporting metastasis and angiogenesis. Furthermore, luteolin sensitizes a variety of cancer cells to therapeutically induced cytotoxicity through suppressing cell survival pathways and simulating apoptosis pathways. Notably, luteolin is blood–brain barrier permeable, rendering it applicable to the therapy of

central nerve system diseases, including brain cancer [67]. In addition, recent studies have attributed a cancer prevention potential to luteolin [68]. The wide use of luteolin in the treatment of several diseases requires application of analytical procedures for monitoring the levels of drug in dosage forms and in biological fluids. The development of analytical methodologies for monitoring the occurrence of luteolin is demanded since this compound is a concern for human health and environment. So far, a great deal of methods has been reported for the determination of luteolin including liquid chromatography–mass spectrometry (LC–MS) [69], high-performance liquid chromatography (HPLC) [70], gas chromatography (GC) [71], spectrophotometry [72], fluorimetry [73] and capillary electrophoresis (CE) [74]. Although these methods have advantages of sensitivity and accuracy, most of them have their own shortcomings, such as time-consuming, high cost or complicated operation. The electrochemical technique with the merits of sensitivity, accuracy, simplicity and ease of on-site determination, has attracted considerable attention for the analysis of these pharmic molecules.

1.3 Research contents

As mentioned above, it is of great emergency for construct high selective and sensitive electrochemical analytic method for various analyte in every field, and the key point of the work is to search novel nanomaterial for modification of the working electrode. HAp and HAp-based nanocomposite have many excellent properties such as easy preparation, stereoscopic structure, excellent biocompatibility, rich active sites, good ion-exchange and adsorption capacity, which enable them to be acted as advanced functional materials for electrochemical sensor fabrication.

Therefore, the aims of the present study were to synthesis of HAp and HAp-based nanocomposite, and then applied these materials for modification of these the working electrode for detection of various species.

Chapter 2: Rod-like HAp was synthesized by a facile wet method, and the morphology

and structure of the obtained HAp were characterized. Then HAp-Nafion composite was prepared and used for the fabrication of modified electrode for detecting of Hg^{2+}, Cu^{2+}, Pb^{2+} and Cd^{2+} by differential pulse anodic stripping voltammetry. The results show that the four heavy metal ions present independent and strong stripping peaks on the HAp-Nafion modified electrode, suggesting that the obtained electrode is capable of being used for the simultaneous and sensitive detection of the four ions.

Chapter 3: HAp-CNT was synthesized by an alkaline phosphatase assisted hydrolysis reaction. Then the nanocomposite was anchored on the working electrode for examining the electrochemical behaviors of luteolin. Electrochemical characterization experiments showed that the modified electrode could greatly enhance the electrochemical signal of luteolin as compared to bare electrode and other modified electrodes, which could be ascribed to the synergistic amplification effects of the nanocomposite film.

Chapter 4: HAp-rGO was prepared by *in-situ* HAp on GO surface through chemical wet-method. The whole process can be completed under a moderate temperature (85 °C) situation, without the assistance of any extra reducing agent. When HAp-rGO modified electrode was utilized as an electrochemical for detection of hydrazine, the results exhibited an outstanding performance for electrocatalytic oxidation of hydrazine, due to the synergic effect of HAp with rich active site for hydrazine adsorption and rGO with large surface area and high electronic conductivity.

1.4 References

[1] F. Faridbod, V. K. Gupta and H. A, Zamani, *International Journal of Electrochemistry*, **2011**, 1 (2011).

[2] G. Maduraiveeran and W. Jin, *Trends in Environmental Analytical Chemistry*, **13**, 10 (2017).

[3] X. J. Bo, M. Zhou and L. P. Guo, *Biosens. Bioelectron.*, **89**, 167 (2017).

[4] S. A. Zaidi and J. H. Shin, *Talanta*, **149**, 30 (2016).

[5] Y. Zhang, Y. H. Zhao, S. S. Yuan, H. G. Wang and C. D. He, *Sensor. Actuat. B-Chem.*, **185**, 602 (2013).

[6] H. Akhter, J. Murshed, M. A. Rashed, Y. Oshima, Y. Nagao, M. M. Rahman, A. M. Asiri, M. A. Hasnat, M. N. Uddin, and I. A. Siddiquey, *J. Alloy. Compd.*, **698**, 921 (2017).

[7] R. Ahmad, N. Griffete, A. Lamouri, N. Felidj, M. M. Chehimi and C. Mangeney, *Chem. Mater.*, **27**, 5464 (2015).

[8] N. Lavanya, C. Sekar, R. Murugan and G. Ravi, *Mat. Sci. Eng. C-mater.*, **65**, 278 (2016).

[9] R. Ahmad, N. Tripathy, M. Ahn, Y. Hahn, *J. Colloid Interf. Sci.*, **494**, 153 (2017).

[10] S. H. Kim, A. Umar and S. Hwang, *Ceram. Int.*, **41**, 9468 (2015).

[11] T. X. Wu, T. T. Li, Z. G. Liu, Y. J. Guo and C. Dong, *Talanta*, **164**, 556 (2017).

[12] A. Afkhami, A. Bahiraei and T. Madrakian, *J. Colloid. Interf. Sci.*, **495**, 1 (2017).

[13] M. M. Cheng, X Zhang, M. X. Wang, H. Y. Huang and J. J. Ma, *J. Electroanal. Chem.*, **786**, 1 (2017).

[14] L. Li, J. Ju and W. Chen, *Electrochim. Acta*, **210**, 181 (2016).

[15] M. Elyasi, M. A. Khalilzadeh and H. Karimi-Maleh, *Food Chem.*, **141**, 4311 (2013).

[16] Y. Liao, N. Wang, Y. Ni, J. Xu and S. J. Shao, *J. Electroanal. Chem.,* **754**, 94 (2015).

[17] T. Madrakian, S. Maleki, M. Heidari and A. Afkhami, *Mat. Sci. Eng C-mater.*, **63**, 637 (2016).

[18] T. Kokubo, M. Shigematsu, Y. Nagashima and S. Higashi, *Bull. Inst. Chem. Res. Kyoto Uniu.*, **60**, 260 (1982).

[19] Y. Ota, T. Iwashita, T. Kasuga and Y. Abe, *J. Am. Ceram. Soc.*, **81**, 1665 (1998).

[20] T. Harrori and Y. Lwadate, *J. Am. Ceram. Soc.*, **73**, 1803 (1990).

[21] S. Bose and S. K. Saha, *Chem. Mater.*, 15, 4464 (2003).

[22] D. W. Kim, I. S. Cho, J. Y. Kim, H. L. Jang, G. S. Han, H. S. Ryu, H. Shin, H. S. Jung, H. Kim and K. S. Hong, *Langmuir*, **26**, 384 (2010).

[23] S. Hokkanena, A. Bhatnagarb, E. Repoa, S. Louc and M. Sillanpää, *Chem. Eng. J.*, **283**, 445 (2016).

[24] Z. Opre, J. D. Grunwaldt, M. Maciejewski, D. Ferri, T. Mallat and A. Baiker, *J. Catal.*, **230**, 406 (2005).

[25] P. N. Lima, R. N. Lama, Y. F. Zhengb and E.S. Thiana, *Mater. Lett.*, **172**, 193 (2016).

[26] P. Kanchana and C. Sekar, *Mat. Sci. Eng C-mater.*, **42**, 601 (2014).

[27] P. Kanchana and C. Sekar, *Spectrochim. Acta A*, **137**, 58 (2015).

[28] C. Yang, C. Lin and S. Chiu, *Desalination*, **233**, 137 (2008).

[29] S. U. Maheshwaria, V. K. Samuelb and N. Nagiah. *Ceram. Int.*, **40**, 8469 (2014).

[30] H. Suping, H. Baiyun, Z. Kechao and L. Zhiyou, *Mater. Lett.*, **58**, 3582 (2004).

[31] K. Kaviyarasu, A. Mariappan, K. Neyvasagam, A. Ayeshamariam, P. Pandi, R. Rajeshwara Palanichamy, C. Gopinathan, G. T. Mola and M. Maaza, *Surfaces and Interfaces*, **6**, 247 (2017).

[32] H. Nie and C. H. Wang, *J. Control. Release*, **120**, 111 (2007).

[33] W. Kroto, J. Heath, S. O'Brien, R. Curl and R. Smalley, *Nature*, **318,** 162 (1985).

[34] S. Iijima, *Nature*, **354**, 56 (1991).

[35] K. S. Novoselov, A. K. Geim, S. V. Morozov, D. Jiang, Y. Zhang, S. V. Dubonos, I. V. Grigorieva and A. A. Firsov, *Science*, **306**, 666 (2004).

[36] L. F. C. Pereira, I. Savić and D. Donadio, *New J. Phys.*, **15**, 105019 (2013).

[37] S. L. Zhang, Z. W. Qi, Y. Zhao, Q. Z. Jiao, X. Ni, Y. J. Wang, Y. Chang and C. Ding, *J. Alloy. Compd.*, **694**, 309 (2017).

[38] Q. H. Tana, Q. J. Wang, Y. K. Liu, J. S. Shi, S. Q. Jiang and H. L. Yan, *Mater.*

Design, **100**, 241 (2016).

[39] A. S. Alshammari, M. R. Alenezi, K. T. Lai and S. R. P. Silva, *Mater. Lett.*, **89**, 299 (2017).

[40] C. Baykasoglu, Z. Ozturk, M. Kirca, A. T. Celebi, A. Mugan and A. C. To, *Int. J. Hydrogen Energ.*, **41**, 8246 (2016).

[41] S. J. Chunga, S. H. Lima, C. H. Leeb and J. Jang, *Diam. Relat. Mater.*, **10**, 248 (2001).

[42] R. Y. A. Hassan, R. O. El-Attar, H. N. A. Hassan, M. A. Ahmed and E. Khaled, *Sensor. Actuat. B-Chem.*, **244**, 565 (2017).

[43] Z. T. Zhao, Y. J. Sun, P. W. Li, W. D. Zhang, K. Lian, J. Hu and Y. Chen, *Talanta*, **158**, 283 (2016).

[44] W. Hummers Jr, R. Offeman, *J. Am. Chem.*, 1958.

[45] D. C. Marcano, D. V. Kosynkin, J. M. Berlin, A. Sinitskii, Z. Z. Sun, A. Slesarev, L. B. Alemany, W. Lu and J. M. Tour, *ACS Nano*, **4**, 4806 (2010).

[46] S. J. Park and R. S. Ruoff, *Nat. Nanotechnol.*, **4**, 217 (2009).

[47] M. B. Gumpua, M. Veerapandianc, U. M. Krishnand and J. B. B. Rayappan, *Talanta*, **162**, 574 (2017).

[48] M. B. Gumpu, S. Sethuraman, U. M. Krishnan and J. B. B. Rayappan, *Sens. Actuators B Chem.*, **213**, 515 (2015).

[49] Ü. Anık, S. Timur, M. Çubukçu and A. Merkoçi, *Microchim. Acta*, **160**, 269 (2008).

[50] Y. Bonfil and E. Kirowa-Eisner, *Anal. Chim. Acta*, **457**, 285 (2002).

[51] Y. Lin, D. Gritsenko, S. L. Feng, Y. C. Teh, X. N. Lu and J. Xu, *Biosens. Bioelectron.*, **83**, 256 (2016).

[52] M. Li, L. B. Liu, Y. P. Xiong, X. T. Liu, A. Nsabimana, X. J. Bo and L. P. Guo, *Sens. Actuators B Chem.*, **207**, 614 (2015).

[53] H. Bagheria, A. Afkhamib, H. Khoshsafarb, M. Rezaeib and A. Shirzadmehrb, *Sens. Actuators B Chem.*, **186**, 451 (2013).

[54] A. Afkhami, F. Soltani-Felehgari, T. Madrakian, H. Ghaedi and M. Rezaeivala, *Analytica. Chimica. Acta*, **771**, 21 (2013).

[55] M. Gochfeld, *Ecotox. Environ. Safe.*, **56**, 174 (2003).

[56] F. Zahir, S. J. Rizwi, S. K. Haq and R. H. Khan, *Environ. Toxicol. Phar.*, **20**, 351 (2005).

[57] A. Afkhamia, H. Ghaedi, T. Madrakian and M. Rezaeivala, *Electrochim. Acta*, **89**, 377 (2013).

[58] Y. Zhang, Z. L. Zhang, D. L. Yin, J. Li, R. G. Xie and W. S Yang, *ACS Appl. Mater. Inter.*, **5**, 9709 (2013).

[59] B. K. Bansod, T. Kumar, R. Thakur, S. Rana and I. Singh, *Biosens. Bioelectron.*, **94**, 443 (2017).

[60] S. Amlathe and V. Gupta, *Analyst*, **113**, 1481 (1988).

[61] S. Garrod, M. E. Bollard, A. W. Nicholls, S. C. Connor, J. Connelly, J. K. Nicholson and E. Holmes, *Chem. Res. Toxicol.*, **18**, 115 (2005).

[62] S. K. Mehta and A. Umar, *Talanta*, **85**, 2411 (2011).

[63] J. W. Wu, T. T. Zhou, Q. Wang and A. Umar, *Sens. Actuators B Chem.*, **224**, 878 (2016).

[64] S. Goswami, S. Das, K. Aich, B. Pakhira, S. Panja, S. K. Mukherjee, and S. Sarkar, *Org. Lett.*, **15**, 5412 (2013).

[65] Y. Kima, S. Bonga, Y. Kanga, Y. Yanga, R. K. Mahajanb, J. S. Kimc and H. Kim, *Biosens. Bioelectron.*, **25**, 2366 (2010).

[66] Ziaullah and H. P. Vasantha Rupasinghe, *Applications of NMR Spectroscopy*, **2**, 3 (2015).

[67] H. Ibrahim and Y. Temerk, *Sens. Actuators B Chem.*, **206**, 744 (2015).

[68] J. L. Li, X. D. Cheng, Y. Chen, W. M. He, L. Ni, P. Xiong and M. G. Wei, *Int. J. Pharmaceut.*, **512**, 262 (2016).

[69] D. A. van Elswijk, U. P. Schobel, E. P. Lansky, H. Irth and J. van der Greef, *Phytochemistry*, **65**, 233 (2004).

[70] Q. L. Zhang, J. Li, C. Wang, W. Sun, Z. T. Zhang and W. M. Cheng, *J. Pharmaceut. Biomed.*, **43**, 753 (2007).

[71] C. S. Liu, Y. S. Song, K. J. Zhang, J. C. Ryu, M. Kim and T. H. Zhou, *J. Pharmaceut. Biomed.*, **13**, 1409 (1995).

[72] Baranowska and D. Rarog, *Talanta*, **55**, 209 (2001).

[73] G. Favaro, C. Clementi, A. Romani and V. Vickackaite, *J. Fluoresc.*, **17**, 707 (2007).

[74] X. Q. Xu, L. S. Yu and G. N. *Chen, J. Pharmaceut. Biomed.*, **41**, 493 (2006).

Chapter 2

Rod-like HAp and Nafion Nanocomposite as an Electrochemical Matrix for Simultaneous and Sensitive Detection of Hg^{2+}, Cu^{2+}, Pb^{2+} and Cd^{2+}

2.1 Introduction

Heavy metal contamination is a major concern in environmental pollution due to their serious toxic effects on plants, animals and human bodies [1, 2]. Among various heavy metals, mercury (Hg), lead (Pb), cadmium (Cd), and copper (Cu) are the most probable causes for the heavy metal-related diseases [3, 4]. For example, both inorganic and organic mercury can be absorbed through the gastrointestinal tract, resulting in the damage to the nervous system and the kidneys [5]. Copper is an essential element to human bodies, but the excessive copper can seriously destroy tissue since it can interact with lipid hydroxyperoxides to produce some DNA-damaging agents such as malondialdehyde and 4-hydroxynonenal [6]. Lead has high affinity to sulfhydryl group; therefore it can strongly bind to many sulfhydryl proteases like aminolevulinic acid dehydratase and glutathion reductase [7], and seriously inhibit their activities. Cadmium is also considered as one of the most toxic elements in the environment, with a wide range of organ toxicity and long elimination half-life. The epidemiological studies showed that the abnormity of cadmium in bodies may contribute to various cancers [8]. Therefore, the fast and convenient detection of these four metal ions at trace level is of great concern.

The electrochemical technique has been considered as a promising method for the detection of heavy metal ions due to its advantages of low cost, high sensitivity and good portability [9-11]. Among the current developed electrochemical approaches, anodic stripping voltammetry (ASV) have been widely accepted as one of the most simple and efficient technique, since it can be operated easily and can analyze several heavy metal ions simultaneously [12, 13]. The ASV is usually accomplished by two steps: the preconcentration step and the stripping step. During the preconcentration step, a low potential was applied, from which the metal ions are concentrated on the working electrode, and then reduced to the reduction state. During the stripping step, the potential was scanned from the low potential to the high potential, from which the reduced metal ions are changed to the oxidation state, and the reduced metals are stripped from the electrode surface into the solution as the ion forms. From the

stripping peak potential and current, the metal ions can be qualitatively and quantitatively determined.

However, the common bare electrode in ASV tests often suffered the poor selectivity and inferior sensitivity due to its limited specific area, less active sites and weak adsorption. In contrast, the use of the chemical modified electrodes can greatly improve the efficiency of accumulating target analytes without interference from other substances. With the development of nanoscience, many nanomaterials such as carbon nanotube [14, 15], graphene [16-18], NiO [19], and Co_3O_4 [20] have been utilized for the ASV detection of the heavy metals owing to their inherently merits of large surface area, high mechanical strength and excellent electronic conductivity. But these modification materials are either expensive or require tedious synthesis processes.

HAp is a major component of biological hard tissues such as teeth and bones in animal organism [21]. It has attracted considerable scientific interest in the past decades due to its easy preparation, excellent biocompatibility, rich active sites, good ion-exchange and adsorption capacity [22]. For example, it has been used as adsorbent for chromatographic separation of protein and enzyme [23], as catalyst for alcohols dehydration [24], and as basic material for artificial teeth and bones preparation [25]. In recent years, based on the rich active sites and excellent biocompatibility, the nanosized HAp has also been synthesized and utilized as a functional material in fabrication of modified electrodes for detecting various species. Pang et al. [26] have fabricated a graphene nanosheets and HAp nanocomposite modified electrode and used it for the electrochemical determination of luteolin in peanut hulls. Zhang et al. [27] have utilized HAp derived from natural fish scales as an electrode material for the electrochemical detection of KIM-1, an ideal biomarker for acute kidney injury diagnosis. Also the HAp modified electrodes have also been applied for the detection of heavy metal ions of Pb^{2+} [28], Cd^{2+} [29] *etc*. However, to the best of our knowledge, we have not found the application of HAp as an electrochemical matrix for the simultaneous detection of the four heavy metal ions of Hg^{2+}, Cu^{2+}, Pb^{2+} and Cd^{2+}.

In this chapter, a uniform rod-like HAp was synthesized via a simple and facile wet method, and then the homogeneous HAp dispersion was prepared using Nafion as a

dispersent and stabilizer. Nafion is a sulfonated tetrafluoroethylene-based fluoropolymer-copolymer, which has been extensively applied as an electrode modifier due to its excellent antifouling capacity, high ion-conductivity, good film-forming ability, high permeability and strong adsorption ability [30, 31]. In addition, the hydrophilic negatively charged sulfonate group in Nafion film enables selective accumulation of positively-charged drugs or ions through electrostatic interaction, thus improving the selectivity and sensitivity of electrode interface [32, 33]. Then the composite material of HAp-Nafion was applied as an electrode material for the simultaneous detection of four heavy metal ions, including Hg^{2+}, Cu^{2+}, Pb^{2+} and Cd^{2+}. The result showed that the composite film of HAp-Nafion have high stability on the electrode. Electrochemical stripping experiments showed that four independent and intense stripping peaks corresponding to the oxidation of the deposited Hg^{2+}, Cu^{2+}, Pb^{2+} and Cd^{2+} were observed at HAp-Nafion modified electrode, which could be ascribed to the synergy of HAp and Nafion. In addition, the developed electrode was utilized for the detection of the four heavy metals in real tap water samples, and satisfactory results were achieved, proving a promising strategy for the convenient and fast monitoring of heavy metal ions in environment.

2.2 Experimental

2.2.1 Materials and apparatus

Calcium hydroxide $Ca(OH)_2$ and phosphoric acid (H_3PO_4) were purchased from Wako Pure Chemical Industries Co., Ltd. (Japan). $HgCl_2$, $Cu(NO_3)_2$, $Pb(NO_3)_2$, $CdSO_4$, and the other metal salts were provided by Xilong Chemical Company (China). Nafion (5 wt% solution in low aliphatic alcohols) was purchased from Aldrich (China). Different pH values of NaAc-HAc buffer solutions were prepared through mixing sodium acetate (NaAc) and acetic acid (HAc) with different ratios. All the other chemicals were of analytic reagent grade and obtained commercially. Doubly distilled water (DDW) was used throughout the experiments.

Powder X-ray diffraction (XRD) patterns of the materials were obtained from a Rigaku Miniflex-II diffractometer with a Ni-filtered Cu Kα radiation (30 kV and 15 mA, Japan). The morphology of the HAp was recorded by a TOPCON EM-002B transmission electron microscopy (TEM, Japan). The scanning electron microscopic (SEM) images were gained by a JSM-60-10LA field-emission scanning electron microscopy (Japan). Fourier transform infrared (FTIR) spectra were recorded by a KBr method using a JASCO FTIR-660 plus spectrometer with a resolution of 4 cm^{-1} (Japan). Electrochemical measurements were carried out on CHI 650C electrochemical analyzer (China) in connection with a conventional three-electrode system: a glassy carbon electrode (GCE, diameter=2 mm) modified with different materials was used as the working electrode, Ag/AgCl electrode as the reference electrode, and Pt wire as the counter electrode.

2.2.2 Preparation of rod-like HAp and HAp-Nafion dispersion

The rod-like HAp particles were prepared by a simple wet method. In brief, 0.039 mol of Ca(OH)$_2$ were dissolved into 2.0 L of DDW free from CO$_2$ in a sealed Teflon vessel. After stirring at room temperature for 1 h, 16.7 mL 10% H$_3$PO$_4$ solution was added and the formed suspension was stirred for further 1 h at room temperature. Then, the suspension was aged in an air oven at 85 ℃ for 24 h. At last, the obtained particles were filtered off, thoroughly washed with DDW and dried in an air oven at 85 ℃ overnight.

The nanocomposite of HAp and Nafion (HAp -Nafion) was prepared as follows: 1.0 mg of synthesized HAp was added into 10 mL DDW and ultrasonicated for 5 min. Then 100 μL 5% Nafion was dissolved into 900 μL absolute ethyl alcohol and also ultrasonicated for 5 min to form a 0.5 wt% Nafion solution. Followed by, 100 μL the above prepared HAp dispersion was mixed with 100 μL Nafion solution and ultrasonicated for 5 min to obtain a well-dispersed HAp-Nafion dispersion.

2.2.3 Fabrication of the modified electrode

Before modification, a GCE surface was mechanically polished to mirror-like with 1.0, 0.3, and 0.05 μm alumina slurry, respectively, and then sonicated in ethanol and DDW for 5 min to achieve a cleaned GCE. After that, 10 μL of the prepared HAp-Nafion dispersion was cast onto the freshly cleaned GCE surface and dried at room temperature. And then, the modified electrode was carefully rinsed with DDW to remove the loosely absorbed material, thus the modified electrode of HAp-Nafion/GCE was achieved. For comparison, the Nafion/GCE was also prepared by the same method.

2.2.4 Electrochemical measurements

Electrochemical characterization of HAp-Nafion/GCE was carried out by cyclic voltammetry (CV) in a mixture solution containing 1.0 mM $K_3[Fe(CN)_6]/K_4[Fe(CN)_6]$ and 0.1 M KCl. Electrochemical analysis of Hg^{2+}, Cu^{2+}, Pb^{2+} and Cd^{2+} on HAp-Nafion/GCE was carried out by differential pulse anodic stripping voltammetry (DPASV) in 0.1 M NaAc-HAc. The pre-accumulation potential was -1.3 V and the pre-accumulation time was 120 s. After each measurement, the modified electrode was washed with DDW and then scanned in NaAc-HAc until the electrochemical signals of Hg^{2+}, Cu^{2+}, Pb^{2+} and Cd^{2+} were totally disappeared. All experiments were conducted at room temperature ($25 \pm 2°C$) in air atmosphere.

2.3 Results and discussion

2.3.1 Characterization of rod-like HAp nanoparticles and HAp-Nafion modified electrode

The synthesized HAp was firstly characterized by XRD, and the result was shown in Fig. 2.1A. It was obvious that HAp has the typical characteristic peaks located at

$2\theta=25.9°$, $31.74°$, $39.84°$, $46.68°$, $49.52°$, $53.3°$ and $64.14°$, which was consistent with the XRD result of HAp in literature [34], suggesting that the pure HAp products had been successfully synthesized. The constitution of HAp was identified by FTIR. From the result as displayed in Fig. 2.1B, one can clearly see that the bands at 572 cm^{-1} and 602 cm^{-1} attributable to O-P-O deformation vibration modes of PO_4^{3-}, two pronounced bands at 1050 cm^{-1} and 1097 cm^{-1} corresponding to P-O stretching vibration of PO_4^{3-} groups and 3572 cm^{-1} relate to the lattice OH^- groups were visible [35]. This result further confirmed the successful synthesis process of HAp. Fig. 2.1C shows the TEM image of the HAp particles. From the image, it was found that that large amount of independent particles were observed, suggesting high yield of HAp by the proposed synthesis method. Meanwhile, no aggregation was happened for the HAp during the synthesis process. From the microscopy, it was also found that the HAp particles showed uniform rod shape with the average length of 100 nm and width of 20 nm.
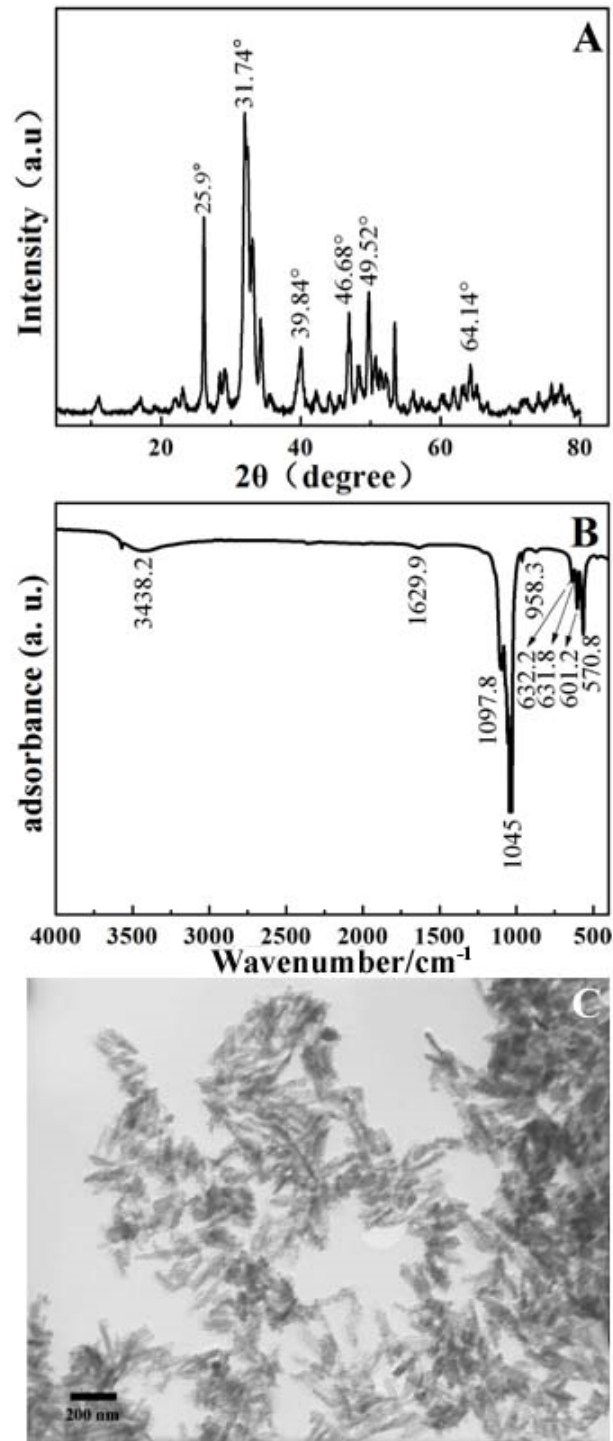
Fig. 2.1 XRD (A), FT-IR (B) and TEM image (C) of HAp.

The surface morphology of the bare GCE, Nafion/GCE and HAp-Nafion/GCE were recorded through SEM, and the results were displayed in Fig. 2.2A-C. It was observed that a smooth surface was observed for the bare GCE (Fig. 2.2A). For the Nafion/GCE, also a smooth surface but with some wrinkles was found (Fig. 2.2B), suggesting good film-forming capacity of the Nafion. However, for the HAp-Nafion composite modified electrode, many particles were distributed on the electrode surface (Fig. 2.2C). The high-magnification SEM further showed that the particles were linked by the Nafion film (inset of Fig. 2.2C). In addition, from the element mapping analysis, all the main elements of C, O, Ca, P and F corresponding to constituents of HAp and Nafion could be clearly detected from the electrode surface (Fig. 2.3), demonstrating that the composite material of HAp-Nafion had been successfully modified on the electrode surface.
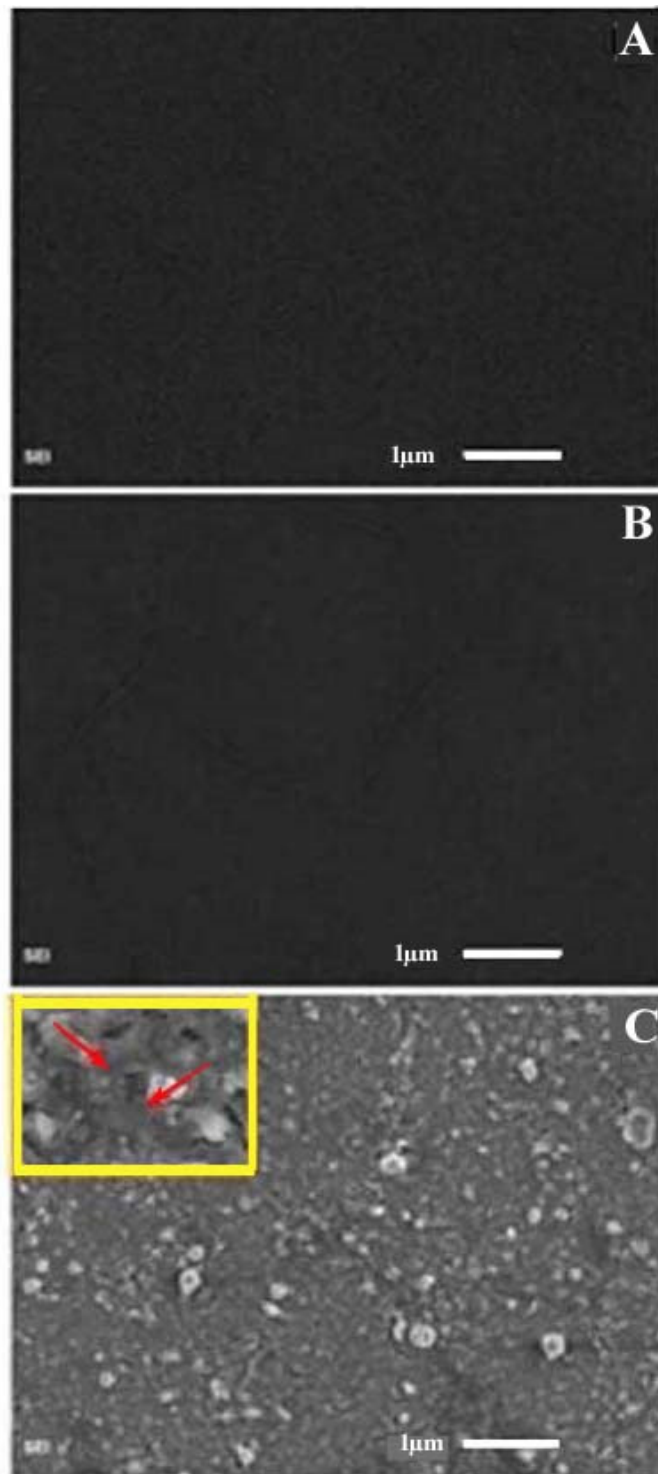
Fig. 2.2 SEM images of bare GCE (D), Nafion/GCE (E) and HAp-Nafion/GCE (F).
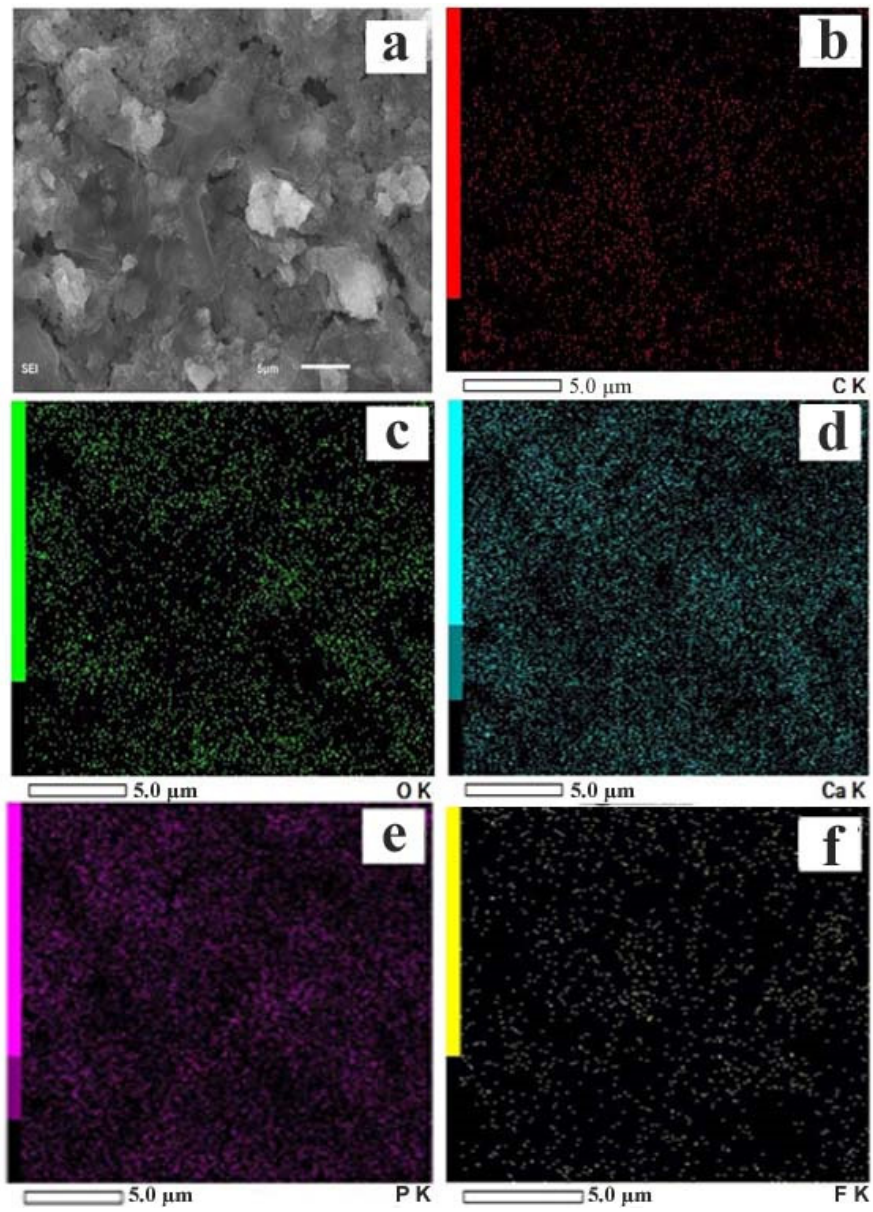
Fig. 2.3 Magnified SEM image (a) of HAp-Nafion film and element mappings of C (b), O (c), Ca (d), P (e), F (f).

2.3.2 Electrochemical stripping voltammetric response of Hg^{2+}, Cu^{2+}, Pb^{2+} and Cd^{2+} at HAp-Nafion/GCE.

Fig. 2.4 illustrates the differential pulse anodic stripping vlotammograms (DPASVs) of HAp-Nafion/GCE in 0.1 M NaAc-HAc (pH 3.0) without and with 5.0×10^{-5} M Hg^{2+}, Cu^{2+}, Pb^{2+} and Cd^{2+}. As shown, no any electrochemical Faradic response was observed for blank solution at HAp-Nafion/GCE (curve c), suggesting that the modified electrode itself is electro-inactive under the measured conditions. However, when the mixture solution of Hg^{2+}, Cu^{2+}, Pb^{2+} and Cd^{2+} were present in the buffer solution, four strong oxidation peaks at 0.120 V, -0.132 V, -0.496 V and -0.696 V were clearly observed (curve b). According to the peak potentials, the four peaks can be ascribed to the stripping process of reduced Hg^{2+}, Cu^{2+}, Pb^{2+} and Cd^{2+} [36-38]. The enough large peak-to-peak separations of the four ions also suggest that the four ions could be detected simultaneously without interference from each other. In addition, in order to probe the effect of HAp on the electrochemical response of the four metal ions, the electrode of Nafion/GCE was prepared and used for the determination of the four metal ions. The result was displayed in curve a of Fig. 2.4. Through comparison, it is clearly observed that the stripping voltammetric response of the four ions were obviously smaller than those at HAp-Nafion/GCE. This result suggests that the HAp-Nafion hybrid material is superior to the single-component of Nafion for the sensitive detection of the four heavy metal ions, which could be ascribed to the unique properties of the HAp nanomaterial including high specific surface areas and rich adsorbing sites of PO_4^{3-} and -OH for the deposition of large amount of metal ions. Therefore, it could be concluded that the HAp-Nafion/GCE could be applied as a high-powered platform for the simultaneous and highly sensitive detection of Hg^{2+}, Cu^{2+}, Pb^{2+} and Cd^{2+}.
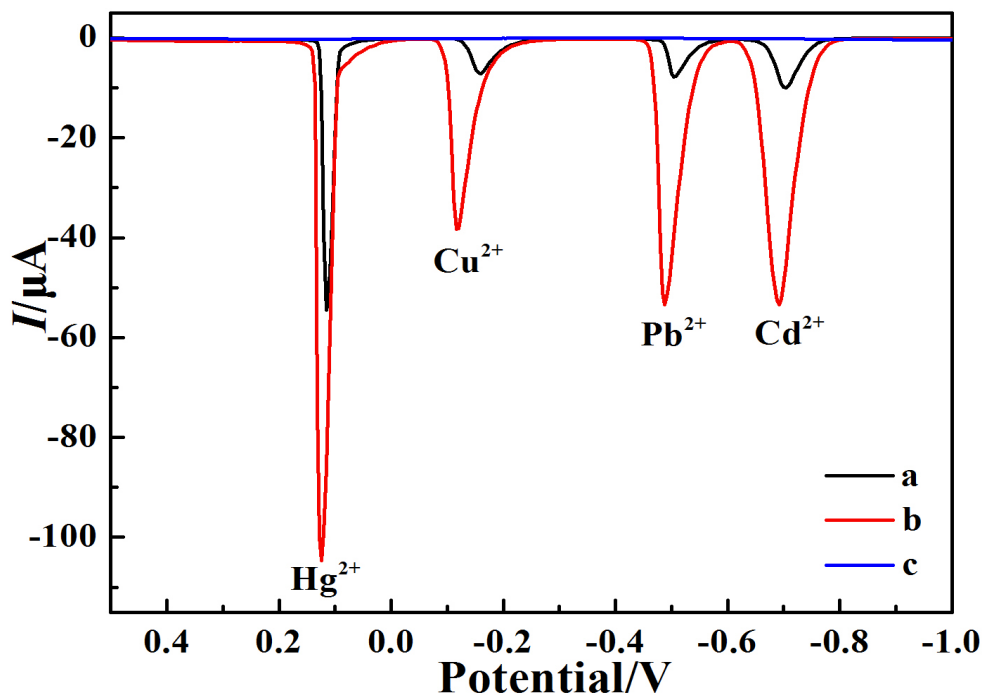
Fig. 2.4 DPASVs of Hg^{2+}, Cu^{2+}, Pb^{2+} and Cd^{2+} at Nafion/GCE (a), HAp-Nafion/GCE (b). Curve c is the DPASV curve of HAp-Nafion/GCE in the blank buffer solution without above four ions. The concentrations of all the ions are 1.0×10^{-5} M. Supporting electrolyte: 0.1 M NaAc-HAc (pH 3.0); Accumulation potential: -1.3 V; Accumulation time: 60 s.

2.3.3 Optimization of experiment conditions

In order to obtain the optimal voltammetric responses of of Hg^{2+}, Cu^{2+}, Pb^{2+} and Cd^{2+} on the HAp-Nafion/GCE, several experimental parameters such as the species and pH values of the supporting electrolyte, the deposition potential and deposition time were optimized. Fig. 2.5 shows the histograms of the DPASV peak currents of Hg^{2+}, Cu^{2+}, Pb^{2+} and Cd^{2+} in different supporting electrolytes including Tris-HCl, B-R and NaAc-HAc. It was found that the four heavy metal ions had the largest stripping peak currents (I_p) in NaAc-HAc solution as compared to Tris-HCl and B-R buffer solution under the same pH value and concentration. Therefore, NaAc-HAc was used as the supporting electrolyte in the following experiment.

The effect of the pH values of the NaAc-HAc buffer solution on the stripping signals of Hg^{2+}, Cu^{2+}, Pb^{2+} and Cd^{2+} was further studied. Fig. 2.6A displays the relationships of the stripping peak currents (I_p) of the four ions with the pH values of NaAc-HAc buffer ranging from 2.5 to 4.5. It was clearly seen that the peak currents of these four metal ions increased in the initial part of pH range and then decreased with the increase of pH value. The low stripping signals at low pH can be explained by the weak adsorption of the heavy metal ions at the protonated modified film, but when the pH values were too high, the heavy metal ions tended to hydrolyze, resulting in the reduction of the accumulating ions. In this work, the largest peak currents could be achieved at the pH value of 3.0 for Hg^{2+} and Pb^{2+}; while at pH 3.5 for Cu^{2+} and Cd^{2+}. Considering that the heavy metal ions are easy to be hydrolyzed at the higher pH, pH 3.0 was chosen as the optimal acidity for the following analysis.

In stripping analysis, the application of adequate deposition potential is very important to achieve the best sensitivity. Thus, the effect of the deposition potential on the stripping responses of Hg^{2+}, Cu^{2+}, Pb^{2+}, and Cd^{2+} over the potential range from -0.9 V to -1.4 V was explored and the results were showed in Fig. 2.6B. It could be clearly observed that all the peak currents of the four ions showed an increasing trend with the decrease of the deposition potential from -0.9 V to -1.3 V, suggesting that the deposition amount of the four ions increased with decrease of the potentials. For Hg^{2+}

and Cd^{2+}, when the deposition potentials further decreased to -1.4 V, the stripping peak currents were constant and slightly weakened. For the Cu^{2+} and Pb^{2+} ions, the peak currents further increased when the deposition potential was changed from -1.3 V to -1.4 V, but the increase in amplitude is slight in comparison with Hg^{2+} and Cd^{2+}. Therefore, according to the overall features of the four ions, the deposition potential of -1.3 V was selected.

Under the optimal deposition potential, the effect of the deposition time on stripping the response of the four ions was further investigated. Fig. 2.6C demonstrated the relationships of the stripping peak currents with the deposition time in the range from 30 to150 s. As seen, with the increase of the deposition time from 30 to 120 s, all the peak currents of these four ions increased accordingly, indicating that the longer deposition time would profit the deposition of more metal ions on the surface of HAp-Nafion/GCE. When the deposition time was longer than 120 s, the peak currents increased slightly or even leveled off, which could be ascribed to the deposition saturation of the surface active sites of HAp-Nafion toward the ions. Therefore, the pre-accumulation time of 120 s was chosen for the following experiments.
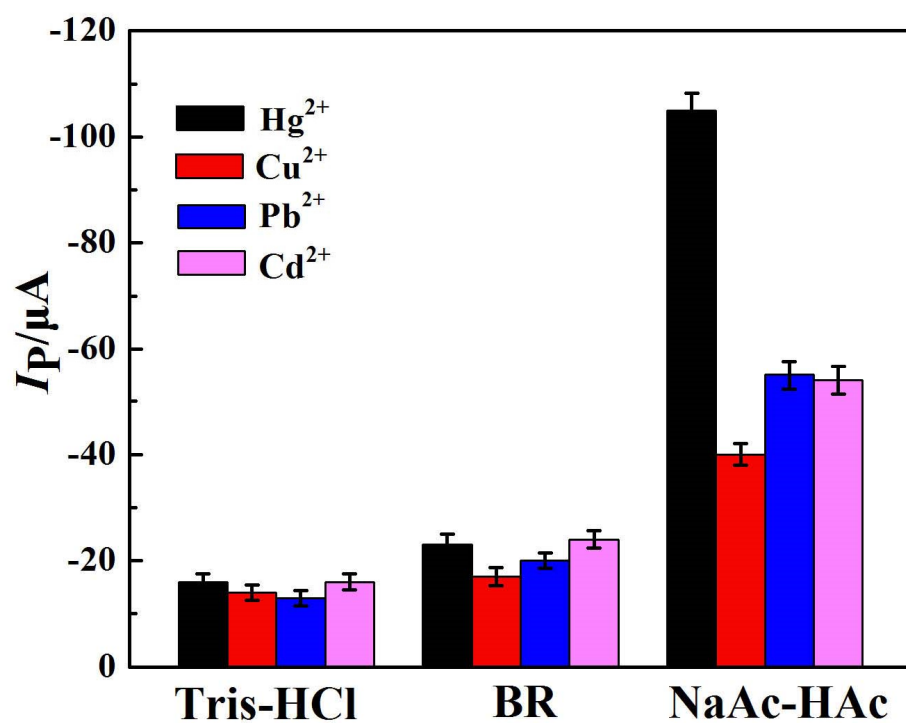
Fig. 2.5 Histogram of stripping peak current (I_p) of Hg^{2+}, Cu^{2+}, Pb^{2+} and Cd^{2+} in Tris-HCl, B-R and NaAc-HAc. All the four heavy metal ion concentrations are 1.0×10^{-5} M.
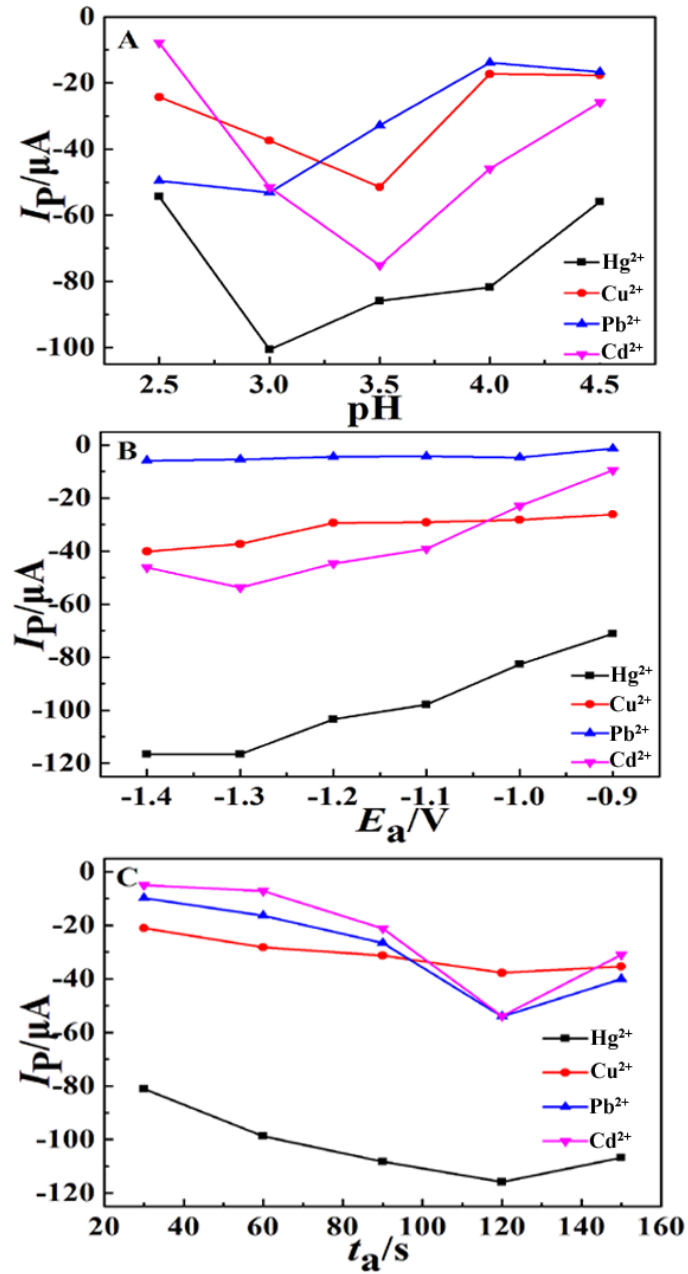
Fig. 2.6 Relationships of stripping peak current (I_p) versuspH values of NaAc-HAc (A), accumulation potential, E_a (B) and accumulation potential, t_a (C). All the four heavy metal ion concentrations are 1.0×10^{-5} M.

2.3.4 Analytical performance for Hg^{2+}, Cu^{2+}, Pb^{2+}, and Cd^{2+}

Under the optimized operational parameters, the performance of HAp-Nafion/GCE for the simultaneous quantitative analysis of Hg^{2+}, Cu^{2+}, Pb^{2+}, and Cd^{2+} was evaluated by DPASV. As shown in Fig. 2.7, four well-defined sharp peaks increased gradually with the increase of the metal ions concentrations in the range from 1.0 to 100 μM for the four heavy metal ions, showing that increasing amounts of deposited metals were formed at the electrode surface with increase of the ion concentrations. Fig. 2.8 shows the linear relationship between stripping peak currents (I_p) and concentrations (C) of the four ions. For Hg^{2+}, two linear parts were observed at the concentrations ranging from 0.1 to 1.0 μM with the regression equation of I_p/μA =-81.370-3.781C (μM), R=0.942, and from 3.0 to 10 μM with the regression equation of I_p/μA=6.344-55.543C (μM), R=0.981. For Cu^{2+}, Pb^{2+}, and Cd^{2+}, the I_p exhibited linear relationships with the ions concentrations over the range from 0.1 to 10 μM with the following regression equations:

Cu^{2+}: I_p/μA=-0.280-6.516C(μM), R=0.994;

Pb^{2+}: I_p/μA=1.440-9.310C (μM), R=0.992;

Cd^{2+}: I_p/μA=0.761-9.511C(μM), R=0.995.

Based on a signal-to-noise ratio characteristic of 3 (S/N=3), the detection limit of Hg^{2+}, Cu^{2+}, Pb^{2+}, and Cd^{2+} were estimated to be 0.03 μM, 0.021 μM, 0.049 μM and 0.035 μM, respectively. The analytical performances of Hg^{2+}, Cu^{2+}, Pb^{2+}, and Cd^{2+} by the proposed approach were also compared with other previously reported modified electrodes and the results were summarized in Table 2.1. From the results, one can find that the developed electrode has superior or comparable detection limits and/or linear ranges with respective to the other materials modified electrodes, exhibiting outstanding analytical performance of the composite of HAp-Nafion.
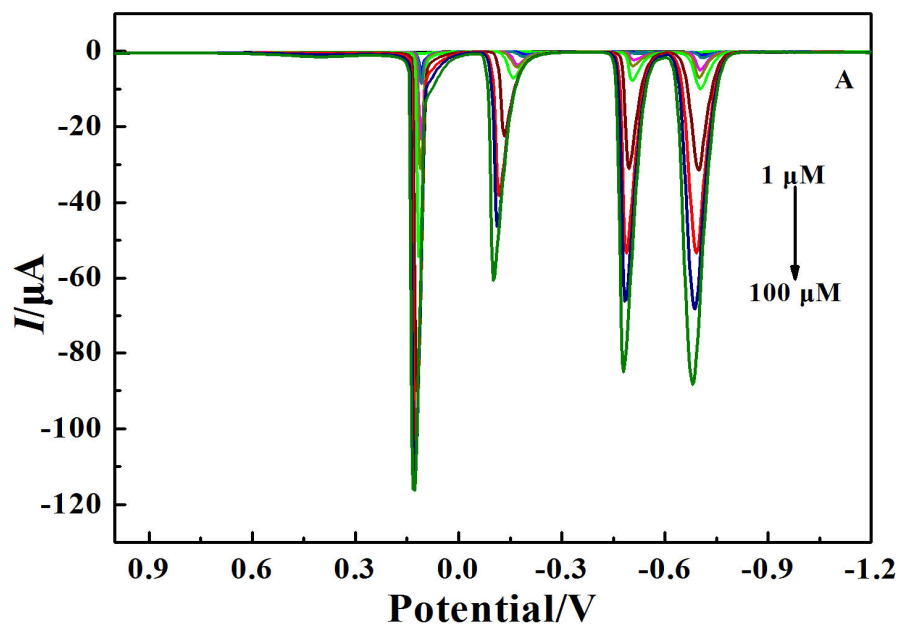
Fig. 2.7 DPASVs of Hg^{2+}, Cu^{2+}, Pb^{2+} and Cd^{2+} mixture solution in concentrations ranging from 1.0 μM to 100 μM recorded on HAp-Nafion/GCE.
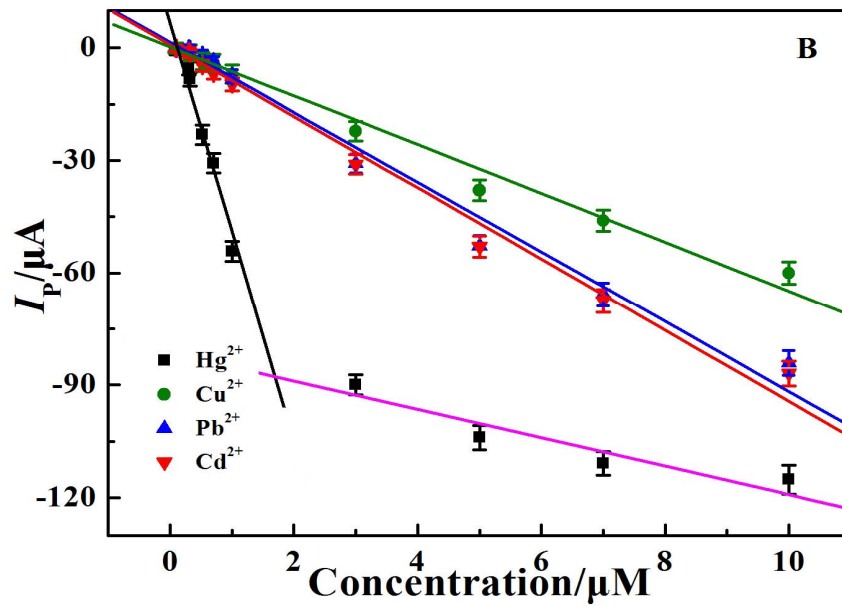
Fig. 2.8 Relationships between stripping peak currents (I_p) and the concentrations (C) of Hg^{2+}, Cu^{2+}, Pb^{2+} and Cd^{2+}.

Table 2.1 Comparison of the analytical performance of electrochemical methods for the determination of heavy metals.

Electrode	Methods	Linear range (µM)				LOD (µM)				Refs.
		Hg^{2+}	Cu^{2+}	Pb^{2+}	Cd^{2+}	Hg^{2+}	Cu^{2+}	Pb^{2+}	Cd^{2+}	
BD-NCD	LSV	1-10	1-22.5	1-22.5	-	0.666	0.102	1.339	-	39
Fe_3O_4	SWASV	1.0-8.0	0.1-1.5	0.04-20.0	0.1-2.0	0.0587	0.221	0.0595	0.213	40
DCD-CPE	DPSV	-	-	0.1-15	0.25-25	-	-	0.01	0.04	41
SBA-15/IL/CPE	DPASV	0.08-50.0	-	0.4-90.0	0.6-30.0	0.01	-	0.04	0.08	42
BT-SBA-15/CPE	DPASV	-	-	0.3-7.0	2.0-10.0	-	-	0.04	0.4	43
Nafion-HAp	DPASV	0.1-1.0; 3.0-10.0	0.1-10.0	0.1-10.0	0.1-10.0	0.030	0.021	0.049	0.035	This work

Notes: -: Not measured; BD-NCD: Boron-doped nanocrystalline diamond; LSV: Linear sweep voltammetry; SWASV: Square wave anodic stripping voltammetry;

DCD-CPE: diacetyldioxime modified carbon paste electrode; BT-SBA-15/CPE: 2-benzothiazolethiol functionalised SBA-15.

Table 2.2 Interference of some metal ions on the stripping peak currents of 1.0×10^{-5} M Hg^{2+}, Cu^{2+}, Pb^{2+} and Cd^{2+} ($n=3$)

Interference ions	Peak currents (μA)				Relative signal change (%)			
	Hg^{2+}	Cu^{2+}	Pb^{2+}	Cd^{2+}	Hg^{2+}	Cu^{2+}	Pb^{2+}	Cd^{2+}
-	-54.24	-7.01	-7.55	-9.70	-	-	-	-
Mg^{2+}	-59.19	-6.51	-6.82	-9.52	9.12	-7.13	-9.66	-1.85
Zn^{2+}	-52.84	-6.72	-7.39	-8.77	-2.58	-4.13	-2.12	-9.58
Ni^{2+}	-51.67	-7.21	-7.36	-9.45	-4.73	2.85	-2.52	-2.58
Na^{+}	-53.74	-6.87	-7.07	-9.93	-6.11	-2.00	-6.36	2.37
Ca^{2+}	-49.31	-7.25	-7.78	-8.86	-9.09	3.42	3.05	-8.66
K^{+}	-53.43	-6.31	-7.69	-10.24	-1.49	-9.98	1.85	5.57

Table 2.3 Determination of Hg^{2+}, Cu^{2+}, Pb^{2+} and Cd^{2+} in tap water (*n=3*)

No.	Added (μM)				Found (μM)				Recovery (%)			
	Hg^{2+}	Cu^{2+}	Pb^{2+}	Cd^{2+}	Hg^{2+}	Cu^{2+}	Pb^{2+}	Cd^{2+}	Hg^{2+}	Cu^{2+}	Pb^{2+}	Cd^{2+}
1	10.0	10.0	10.0	10.0	10.9	10.4	10.4	9.76	109	104	104	97
	20.0	20.0	20.0	20.0	21.4	19.8	20.6	19.7	107	99	103	99
2	10.0	10.0	10.0	10.0	9.4	10.7	9.1	10.1	94	107	91	101
	20.0	20.0	20.0	20.0	19.2	21.8	21.0	21.6	96	109	105	108

2.3.5 Interference study

The interference study was performed by adding the possible interfering common cations including Mg^{2+}, Zn^{2+}, Ni^{2+}, Na^+, Ca^{2+} and K^+ respectively in mixture solution containing 1.0×10^{-5} M Hg^{2+}, Cu^{2+}, Pb^{2+} and Cd^{2+}. The DPASV response current of Hg^{2+}, Cu^{2+}, Pb^{2+} and Cd^{2+} in the absence (I_0) and presence (I_i) of interfering metal ions and the relative signal changes (I_i/I_0-1) are summarized in Table 2.2. It is found that the peak currents of Hg^{2+}, Cu^{2+}, Pb^{2+} and Cd^{2+} in the presence of all the studied interfering ions suffered a little change. It may be a result of the higher affinity of the composite film to target analytes than the interfering ions. The absolute values of relative signal changes were varied from 1.85% to 9.98%, which suggests a satisfying selectivity for the simultaneous determination of Hg^{2+}, Cu^{2+}, Pb^{2+} and Cd^{2+} ions.

2.3.6 Stability, reproducibility and reusability

The stability of the modified electrode for the detection of the four ions was investigated by storage of the prepared electrode in a refrigerator at 4 °C, and then tested the four heavy metal ions with the concentration of 1.0×10^{-5} M under the optimized conditions after storage of 15 days. The results showed that the stripping peak currents only decreased by 2.5%, 5.6%, 4.8% and 5.2% for Hg^{2+}, Cu^{2+}, Pb^{2+} and Cd^{2+}, respectively, showing a good stability of the fabricated electrode. In order to study the reproducibility of the modified electrode, five HAp-Nafion/GCEs based on the same fabrication procedure were prepared and applied to detect 5.0×10^{-5} M Hg^{2+}, Cu^{2+}, Pb^{2+} and Cd^{2+}. The relative standard deviation (RSD) derived from the peak currents from five tests for Hg^{2+}, Cu^{2+}, Pb^{2+} and Cd^{2+} was 6.1%, 3.1%, 4.8%, 4.2% and 5.9%, respectively, indicating that the developed method has a good reproducibility. When the measured electrode was washed with DDW and then electrochemically scanned in NaAc-HAc until the electrochemical signals of all the ions were totally disappeared, it was used for the next run of measurement for Hg^{2+}, Cu^{2+}, Pb^{2+} and Cd^{2+}. The results showed that after five runs of measurement-cleaning,

the signals could remain 85%, 80%, 92%, and 83% of the initial measurement, suggesting a good reusability of the electrode for the detection of the heavy metal ions.

2.3.7 Analysis of real samples

To evaluate its accuracy in practical applications, the developed method was employed to simultaneously determine Hg^{2+}, Cu^{2+}, Pb^{2+} and Cd^{2+} concentrations in tap water that collected from our campus. Before measurements by DPASV, the water samples were filtered with a 0.22 μm membrane and diluted with 0.1 M NaAc-HAc buffer solution (pH 3.0). Then 10.0 μM Hg^{2+}, Cu^{2+}, Pb^{2+} and Cd^{2+} standard solution were simultaneously added into the water samples, and determined by DPASV under the optimal conditions. The found concentrations and the recoveries of the four ions were listed in Table 2.3. From the results, it was clear that the found concentrations were well agreed with the added amounts, and the recoveries for the four ions were 94-109% (Hg), 99-109% (Cu), 91-105% (Pb) and 97-108% (Cd). Therefore it could be concluded that the proposed electrode was promising for heavy metal ion monitoring in the real water samples.

2.4　Conclusions

In summary, the rod-like HAp was synthesized by a facile wet method, and the morphology and structure of the obtained HAp were characterized. Then HAp-Nafion composite was prepared and used for the fabrication of modified electrode for detecting of Hg^{2+}, Cu^{2+}, Pb^{2+} and Cd^{2+} by differential pulse anodic stripping voltammetry. The results show that the four heavy metal ions present independent and strong stripping peaks on the HAp-Nafion modified electrode, suggesting that the obtained electrode is capable of being used for the simultaneous and sensitive detection of the four ions.

2.5 References

[1] J.A. Rodríguez Martína, C. De Arana, J.J. Ramos-Mirasc, C. Gilc, R. Boluda, *Environ. Pollut.* **196** (2015) 156-163.

[2] A. Singh, R.K. Sharma, M. Agrawal, F.M. Marshall, *Food Chem. Toxicol.* **48** (2010) 611-619.

[3] N.V. Solenkova, J.D. Newman, J.S. Berger, G. Thurston, J.S. Hochman, G.A. Lamas, *Am. Heart J.* **168** (2014) 812-822.

[4] M. Adrees, S. Alia, M. Rizwan, M. Zia-ur-Rehman, M. Ibrahim, F. Abbas, M. Farid, M. F. Qayyum, M. K. Irshad, *Ecotox. Environ. Safe.* **119** (2015) 186-197.

[5] M.B. Gumpu, S. Sethuraman, U.M. Krishnan, J.B.B. Rayappan, *Sensor. Actuat. B-Chem.* **213** (2015) 515-533.

[6] S.J.S. Flora, M. Mittal, A. Mehta, *Indian J. Med. Res.* **128** (2008) 501-523.

[7] S.J.S. Flora, *Oxid. Med. Cell. Longev.* **2** (2009) 191-206.

[8] X.L. Wei, J.R. He, Y.L. Cen, Y. Su, L.J. Chen, Y. Lin, B.H. Wu, F.X. Su, L.Y. Tang, Z.F. Ren, *Clin. Chim. Acta* **438** (2015) 80-85.

[9] M.B. Gumpua, S. Sethuraman, U.M. Krishnan, J.B.B. Rayappan, *Sensor. Actuat. B-Chem.* **213** (2015) 515-533.

[10] Q.Y. Liu, B.D. Liu, F. Yuan, H. Zhuang, C. Wang, D. Shi, Y.K. Xu, X. Jiang, *Appl. Surf. Sci.* **356** (2015) 1058-1063.

[11] L. Cui, J. Wu, H. Ju, *Biosens. Bioelectron.* **63** (2015) 276-286.

[12] D. Zhao, X. Guo, T. Wang, N. Alvarez, V.N. Shanov, W.R. Heineman, *Electroanal.* **26** (2014) 488-496.

[13] H. El-Mai, E. Espada-Bellido, M. Stitou, M. García-Vargas, M.D. Galindo-Riaño, *Talanta*, **151** (2016) 14-22.

[14] A. Afkhami, H. Bagheri, H. Khoshsafar, M. Saber-Tehrani, M. Tabatabaee, A. Shirzadmehr, *Anal. Chim. Acta* **746** (2012) 98-106.

[15] B.C. Janegitz, L.H. Marcolino-Junior, S.P. Campana-Filho, R.C. Faria, O. Fatibello-Filho, *Sensor. Actuat. B-Chem.* **142** (2009) 260-266.

[16] Y. Wei, C. Gao, F.L. Meng, H.H. Li, L. Wang, J.H. Liu, X.J. Huang, *J. Phys.*

Chem. C **116** (2012) 1034-1041.

[17] L. Wu, X. Fu, H. Liu, J. Li, Y. Song, *Anal. Chim. Acta* **851** (2014) 43-48.

[18] J. Li, S. Guo, Y. Zhai, E. Wang, *Electrochem. Commun.* **11** (2009) 1085-1088.

[19] X. Li, H. Wen, Q. Fu, D. Peng, J. Yu, Q. Zhang, X. Huang, *Appl. Surf. Sci.* **363** (2016) 7-12

[20] A. Salimi, R. Hallaj, S. Soltanian, H. Mamkhezri, *Anal. Chim.* Acta **594** (2007) 24-31.

[21] N.O. Engin, A.C. Tas, *J. Eur. Ceram. Soc.* **19** (1999) 2569-2572.

[22] E. Garskaite, K.A. Gross, S.W. Yang, Thomas C.K. Yang, J.C. Yang, A. Kareiva, *Cryst. Eng. Commun.* **16** (2014) 3950-3959.

[23] S. Yao, G. Li, B. Li, Y. Zhao, L. Sun, P. Qu, *Mater. Res. Bull.* **64** (2015) 200-206.

[24] S. Wuytsa, D.E. De Vosa, F. Verpoortb, D. Deplac, R.D. Grysec, P.A. Jacobs, *J. Catal.* **219** (2003) 417-424.

[25] W. Suchanek, M. Yoshimura, *J. Mater. Res.* **13** (1998) 94-117.

[26] P. Pang, Y. Liu, Y. Zhang, Y. Gao, Q. Hu, *Sensor. Actuat. B-Chem.* **194** (2014) 397-403.

[27] Y. Zhang, W. Zhang, Q. Zhang, K. Li, W. Liu, Y. Liu, C.E. Banks, *Analyst* **139** (2014) 5362-5366.

[28] M.A. El Mhammedi, M. Achak, M. Bakasse, *Arab. J. Chem.* **6** (2013) 299.

[29] Y. Li, X. Liu, X. Zeng, Y. Liu, X. Liu, W. Wei, S. Luo, *Sensor. Actuat. B-Chem.* **139** (2009) 604-610.

[30] P.K. Kalambate, B.J. Sanghavi, S.P. Karna, A.K. Srivastava, *Sensor. Actuat. B-Chem.* **213** (2015) 285-294.

[31] I. Saidi, I. Soutrel, F. Fourcade, A. Amrane, N. Bellakhal, F. Geneste, *Electrochim. Acta,* **191** (2016) 821-831.

[32] A.C. Torres, M.M. Barsan, C.M.A. Brett, *Food Chem.* **149** (2014) 215-220.

[33] A. Babaei, A. R. Taheri, *Sensor. Actuat. B-Chem.* **176** (2013) 543-551.

[34] H. Tanaka, D. Ihata, *Mater. Res. Bull.* **45** (2010) 103-108.

[35] I. Mobasherpour, M. Soulati Heshajin, A. Kazemzadeh, M. Zakeri, *J. Alloy. Compd.* **430** (2007) 330-333.

[36] J. Wang, J. Lu, S.B. Hocevar, P. A. M. Farias, *Anal. Chem.* **72** (2000) 3218-3222.

[37] J. Wang, L. D. Hutchins-Kumar, *Anal. Chem.* **58** (1986) 402-407.

[38] D. Pan, Y. Wang, Z. Chen, T. Lou, W. Qin, *Anal. Chem.* **81** (2009) 5088-5094.

[39] E. Nurhayati, Y. Juang, C. Huanga, C. Hu, R. Muniyadi, *Sep. Purif. Technol.* (2015). DOI: 10.1016/j.seppur.2015.07.022.

[40] E. Li, X. Yao, Z. Guo, J. Liu, X. Huang, *J. Electroanal. Chem.* **749** (2015) 75-82.

[41] C. Hu, K. Wu, X. Dai, S. Hu, *Talanta* **60** (2003) 17-24.

[42] P.H. Zhang, S.I. Dong, G.Z. Gu, T. L. Bull. Korean Chem. Soc. **31** (2010) 2949-2954.

[43] I. Cesarino, G. Marino, J.D.R. Matos, E.T.G. Cavalheiro, *Talanta* **75** (2008) 15-21.

Chapter 3

Alkaline Phosphatase Mediated Synthesis of Carbon Nanotube-Hydroxyapatite Nanocomposite and its Application for Electrochemical Determination of Luteolin

3.1 Introduction

Flavonoids, a type of natural polyphenolic compounds that are abundant in fruits and vegetables, received great interest in the biochemical and pharmacological fields due to their antioxidant free-radical scavenging, anti-inflammatory, anti-carcinogenic and other beneficial properties [1]. The luteolin (3',4',5',7-tetrahydroxyflavone) is one of the most important flavonoids that can be obtained from in celery, green pepper, parsley, perilla leaf and chamomile tea. Recent studies have shown that this compound has significant biological effects including anti-inflammatory, anti-bacterial and anti-oxidant, as well as anti-proliferative activity against cancer cells [2-4]. The accurate and sensitive determination of luteolin is a critical step for the evaluation of its biological and medical effects. Up to date, various methods have been reported for the determination of luteolin, including high-performance liquid chromatography [5, 6], capillary electrophoresis [7, 8], spectrophotometry [9], et al.

However, these methods have their inherent shortcomings of time-consuming, low sensitivity, expensive instrument and/or complicate operation process. Recently, based on the excellent electrochemical activity of luteolin from the catechol group on B ring (3',4'-dihydroxyl), the electrochemical method receives considerable interest for luteolin determination due to its fascinating advantages of high sensitivity, rapid response, simplicity of operation and cost-effectiveness [10].

In this chapter, we report the synthesis of HAp-Carbon nanotubes (HAp-CNT) composite that mediated by alkaline phosphatase (ALP) and its application for the electrochemical detection of luteolin. It has been established that the surface of HAp possesses abundant of P-OH groups acting as adsorption sites for various molecules [11]. Nanostructured HAp particles with a higher surface area would be more desirable for their use in many fields. However, the conductivity of HAp crystals is too low for the material to be considered a candidate for its use in electrochemical devices [12, 13]. One approach to improve the conductivity of HAp is to dope the material with metal ions or electro-conductive nanoparticles [14, 15].

Carbon nanotubes (CNTs) with one-dimensional and hollow structure are one of the

most fascinating nanometer materials. Since the discovery by Iijima [16], CNTs have attracted worldwide interests in diverse areas including materials science [17], sensors [18, 19], transistors [20, 21], field-emission display [22], and energy storage [23, 24] due to their high mechanical strength, excellent thermal conductivity, unique electronic properties and thermal stability. These outstanding characters make CNTs ideal candidates to enhance stiffness, strength and electronic conductivity of the composite materials. As a consequence, the nanocomposite of CNT and HAp (CNT-HAp) received great interests, especially in electrochemical field. For example, Safari et al. [25] have synthesized the CNT-HAp through a microwave-assisted solid state metathesis reaction, and the electrochemical impedance spetroscoppy (EIS) result revealed that the composite had better charge transfer capacity than the pristine CNTs due to formation of organized electrical functions between the two components. Li et al. prepared a nanocomposite film of HAP-TiO$_2$-CNT via the ultrasonication mixing method, and used the nanocomposite as a platform to immobilize glucose oxidase for glucose sensing analysis [26]. However, it is difficult to precisely control the chemical and structural uniformity of CNT-HAp prepared by physical mixing or microwave assisted solid state metathesis in these work. The direct deposition of HAP on CNTs via liquid-phase reaction is a proper route to resolve this problem [27]. But because the CNTs are hydrophobic and easy to aggregate in aqueous solution, the functionalization of CNTs via strong acid oxidation to improve the dispersibility is necessary before the controllable deposition of HAp [28].

Herein, in this charpter, the nanocomposite of HAp-CNT was synthesized through a novel alkaline phosphatase (ALp) mediated transformation process using CNT-calcium phenyl phosphate (C$_6$H$_5$PO$_4$Ca· nH$_2$O: CaPP) as the source (Scheme 3.1). Firstly, the phenyl phosphoric acid was interacted with CNTs via π-π stacking and hydrophobic force to obtain a well dispersed phenyl phosphoric acid-introduced CNT solution. Secondly, the CaPP was prepared on CNT surface by reacting phenyl phosphoric acid on CNT with Ca^{2+} added in the solution. Followed by, the phenyl phosphoric acids in CaPP on CNT surface were hydrolyzed by adding alkaline phosphatase at 36.5 ℃ to recrystallize as HAp. Thus, the HAp particles were

generated and *in-situ* deposited on the surface of the CNT. The transformation process was characterized by powder X-ray diffraction (XRD), Fourier transform infrared (FTIR) and transmission electron microscope (TEM).

Moreover, based on its multiple active sites, high surface area and excellent conductivity, the nanocomposite was used as an electrochemical sensing material for the determination of luteolin. Under the optimum conditions, differential pulse voltammetry (DPV) showed a good correlation with the concentration of luteolin over the range from 4.0×10^{-7} to 1.2×10^{-5} M, and detection limit was estimated to be 8.0×10^{-8} M. This work opens a new way for the synthesis of HAp-CNT composite, and broadens its application in electrochemical field.
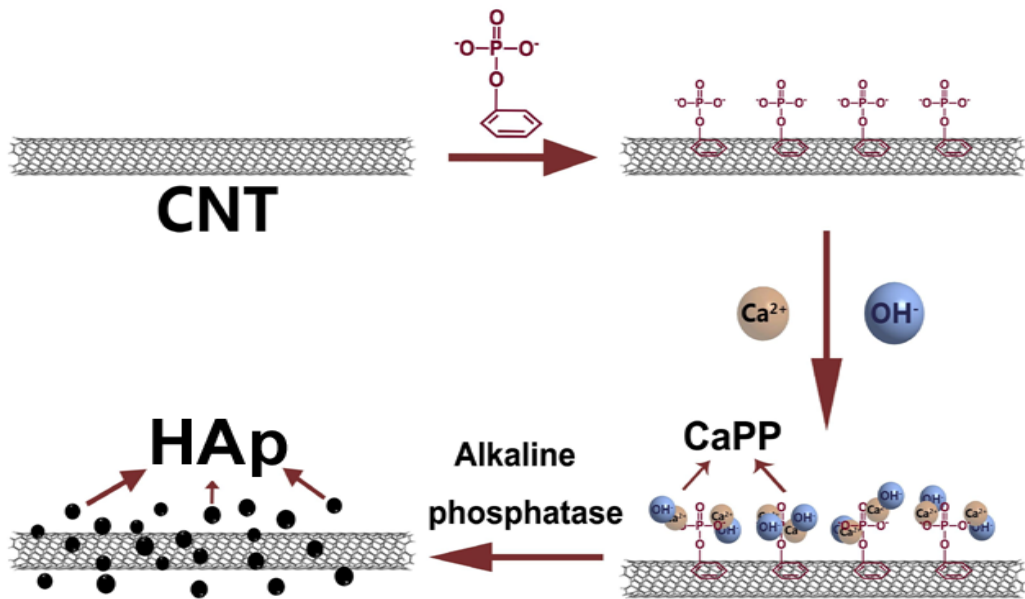
Scheme 3.1 Diagram for the transformation process from CaPP-CNT to
HAp-CNT with the assist of alkaline phosphatase.

3.2 Experimental

3.2.1 Materials and apparatus

Luteolin was purchased from Sigma-Aldrich Co., Ltd. (China). Multi-walled carbon nanotubes (diameter 40-60 nm) and $Ca(OH)_2$ were purchased from Wako Pure Chemical Industries Co., Ltd. (Japan). Phenyl phosphoric acid was purchased from Tokyo Chemical industry Co., Ltd. (Japan). Alkaline phosphatase (ALP) from bovine intestinal mucosa with specific enzyme activity of 1.5 units mg^{-1} was purchased from Biozyme Laboratories (Japan). Tris (hydroxymethyl) aminomethane (Tris) was provided by Xilong Chemical Company (China) and Tris-HCl buffer solution was prepared by adding appropriate HCl in 10 mM Tris. Phosphate buffer saline (PBS) with various pH was prepared through mixing 0.02 M NaCl and 0.05 M NaH_2PO_4-Na_2HPO_4 with different ratios. Britton-Robinson (B-R) buffer solution was prepared by adding 0.4 M acetic acid and 0.4 M boric acid into a solution of 0.4 M phosphoric acid. Chitosan (CS) was purchased from Aladdin Reagent Co., Ltd. (China). All the other chemicals were of analytical reagent grade and obtained commercially. Doubly distilled water was used throughout the experiments.

Powder X-ray diffraction (XRD) patterns of the materials were obtained from a Rigaku diffractometer with a Ni-filtered Cu k_α radiation (30 kV and 16mA, Japan). Particle morphology was observed by a TOPCON transmission electron microscope (TEM, Japan). Transmission IR spectra were recorded by a KBr method using a JASCO Fourier transform infrared (FTIR) spectrometer with a resolution of 4 cm^{-1} (Japan). Electrochemical measurements were carried out on a CHI 650C electrochemical analyzer (China) in connection with a conventional three-electrode system: a glassy carbon electrode (GCE diameter=2 mm) modified with different materials was used as the working electrode, Ag/AgCl electrode as the reference electrode, and Pt wire as the counter electrode.

3.2.2 ALP mediated synthesis of HAp-CNT

Firstly, the CaPP-CNT nanocomposite was prepared by a simple sonication method [29]. In brief, 10.0 mg CNTs were dispersed in 100 mL water free from CO_2 in a sealed polypropylene vessel and ultrasonicated for 2 h. Then 50.0 mL of 0.106 mM aqueous phenyl phosphoric acid solution was added. After the mixture was sonicated for 1 h, 100 mL of 8.85 mM $Ca(OH)_2$ was added, and then aged at 37°C for 24 h. Afterwards, the product were filtered, thoroughly washed with water and finally dried at 50°C in an air oven for 1 day, thus the sample of CaPP-CNT was obtained.

Transformation of HAp-CNT from CaPP-CNT was carried out as follows: 235 mg of the synthesized CaPP-CNT was dispersed into 210 mL of water free from CO_2 under stirring at room temperature. The aqueous solution including 15 mg alkaline phosphatase was then added into the solution suspending the CaPP-CNT particles. The pH of the suspension was adjusted to 9.6 by adding 1.0 M aqueous NH_3 solutions and the suspension was treated at 36.5^{o}C for 48 h in an incubator. After aging, the product was filtered, thoroughly washed with water and finally dried at 50°C in an air oven overnight, through which the transformation of HAp-CNT from CaPP-CNT was achieved and the target product of HAp-CNT was obtained.

For comparison, pure HAp was also prepared by the following simple method [30]: 0.039 mol of $Ca(OH)_2$ were dissolved into 2.0 L of deionized-distilled water free from CO_2 in a sealed Teflon vessel. After 1 h of string at room temperature, 16.7 mL 10% H_3PO_4 solution were added into the solution and the suspension formed was stirred for further 1 h at room temperature. This suspension was aged in an air oven at 85°C for 24 h. At last, the HAp particles generated were filtered off, thoroughly washed with distilled water and finally dried in an air oven at 85°C for 24 h.

3.2.3 Fabrication of the HAp-CNT modified electrode

Firstly, a GCE surface was polished to mirror-like with 1.0, 0.3, and 0.05 μm alumina slurry, respectively, and then sonicated in ethanol and water for 5 min to achieve a

cleaned GCE. The nanocomposite of CS and HAp-CNT (HAp-CNT-CS) was prepared as follows: 1.0 mg of CaPP-CNT was added into 10 mL 1.0% acetic acid solution containing 0.3 wt% CS, and then ultrasonicated for 1 h under 80 W to obtain a homogeneous well-dispersed solution. Here CS was added as a stabilizer to improve the mechanical stability of the HAp-CNT film electrode. Followed by, 10 μL of the prepared HAp-CNT-CS aqueous solution was cast onto the above cleaned GCE surface and dried at room temperature. Afterwards the modified electrode was carefully rinsed with water to remove the loosely absorbed material, and thus the modified electrode of HAp-CNT-CS/GCE was achieved. For comparison, the HAp-CS/GCE and CNT-CS/GCE were also prepared by the same method.

3.2.4 Electrochemical measurements

Electrochemical characterization of HAp-CNT-CS/GCE was carried out by cyclic voltammetry (CV) and electrochemical impedance spectra (EIS) in a mixture solution containing 1.0 mM $K_3[Fe(CN)_6]/K_4[Fe(CN)_6]$ and 0.1 M KCl. Electrochemical analysis of luteolin on HAp-CNT-CS/GCE was carried out in 0.2 M pH 2.0 PBS buffer solution. The CV was scanned within a potential range from 0.3 V to +0.9 V with a scan rate of 100 mV s^{-1}. The DPV was recorded within a potential range between 0.3 V and 0.9 V with pulse amplitude of 0.05 V, pulse width of 0.05 s and pulse period of 0.2 s. After each measurement, the modified electrode was washed with water and scanned in blank PBS until the electrochemical signal of luteolin was totally disappeared.

3.3 Results and discussion

3.3.1 Characterization of HAp-CNT nanocomposite

The synthesis of HAp-CNT was first characterized by TEM. Fig. 3.1A showed the nano-sized regular fusiform-like particles of pure HAp with an average length of 100 nm and width of 20 nm. Fig. 3.1B showed the characteristic one-dimension

wire-shaped and intertwined CNT. The smooth surface of the CNT wire suggested the single-constitution of CNT. After the CNT was mixed with phenyl phosphoric acid, we found that the CNT remains the same TEM result of pure CNT (data not shown). But the dispersion efficiency of CNT in water was greatly improved when phenyl phosphoric acid was present as observed by visual observation. Inset of Fig. 3.1B shows the electronic photographs of aqueous solution of pristine CNT (1) and its mixture with phenyl phosphoric acid (2) after sonication for 30 min. Obviously, the CNT completely settled at the bottom of vial within 30 min, suggesting inferior dispersibility of pristine CNT. This could be ascribed to the aggregation between CNTs caused by the strong π-π stacking and/or Van der Waals force. However, a homogeneous black solution was observed for the mixture solution of CNT and phenyl phosphoric acid. The reason may lies in the fact that the phenyl phosphoric acid was attached on the wall of CNT via the π-π stacking, and the negatively charged phosphate group made the composite particles keeps away from each other through the electrostatic repulsion, preventing the aggregation of CNTs. Through such a comparison, it could be concluded that the dispersibility and water-solubility of CNTs could be greatly improved by introducing the hydrophilic phenyl phosphoric acid onto their surface. This case is also very helpful for the following homogeneous *in-situ* adsorption of Ca^{2+}, and the transformation two HAp. The TEM image of CNT-CaPP showed that many particles were visible on the wall surface of CNTs (Fig. 3.1C), indicating that the insoluble CaPP particles were formed on the surface of CNT. Interestingly, after the CaPP-CNT was treated with alkaline phosphatase, it was found that the amount of particles adsorbed on the surface of CNT increased greatly (Fig. 3.1D). This indicated that the aggregated and insoluble HAp particles were formed and directly deposited on the surface of CNT, resulting in the composite of HAp-CNT. This result also meant that alkaline phosphatase played an important role for the transformation of CaPP to HAp.
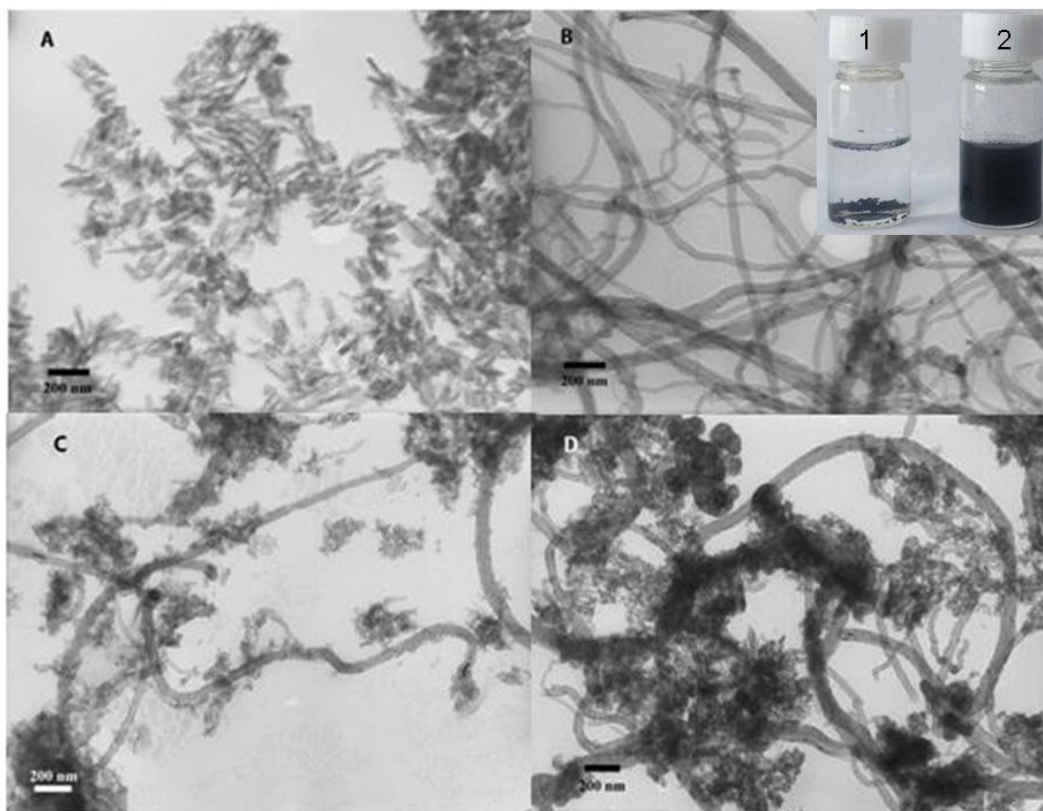
Fig. 3.1 TEM images of HAps (A), pristine CNTs (B), CaPP-CNT (C) and HAp-CNT (D). Inset of (B) is the electronic photographs of CNT aqueous solution in the absence (1) and presence of phenyl phosphoric acid (2).

The product was further characterized by XRD and the results were shown in Fig. 3.2. Fig. 3.2a illustrated the XRD pattern of CNTs. It was obvious that CNTs had the typical characteristic peaks at the position of $2\theta=26.6^{\circ}$, which was consistent with results of literature previously reported [34]. The intermediate product CaPP-CNT not only had the typical peaks of CNT, but also possessed some new diffraction peaks at $2\theta=6.6^{\circ}, 13.3^{\circ}, 20.0^{\circ}, 26.0^{\circ}$ and 29.1° (Fig. 3.2b). According to literature [30], the newly appeared peaks proved the formation of CaPP. After CaPP-CNT was treated with alkaline phosphatase, the XRD pattern was drastically changed (Fig. 3.2c). It was obviously observed that the peaks at $2\theta=6.6^{\circ}, 13.3^{\circ}, 20.0^{\circ},$ and 26.0° of CaPP were disappeared, and only the strong peak corresponding to the CNT remained, indicating that the CaPP has been hydrolyzed and transformed. It was noticeable that in the XRD pattern of HAp-CNT, no obvious diffraction peak corresponding to HAp was observed, which suggested that the HAp synthesized in this work was amorphous.
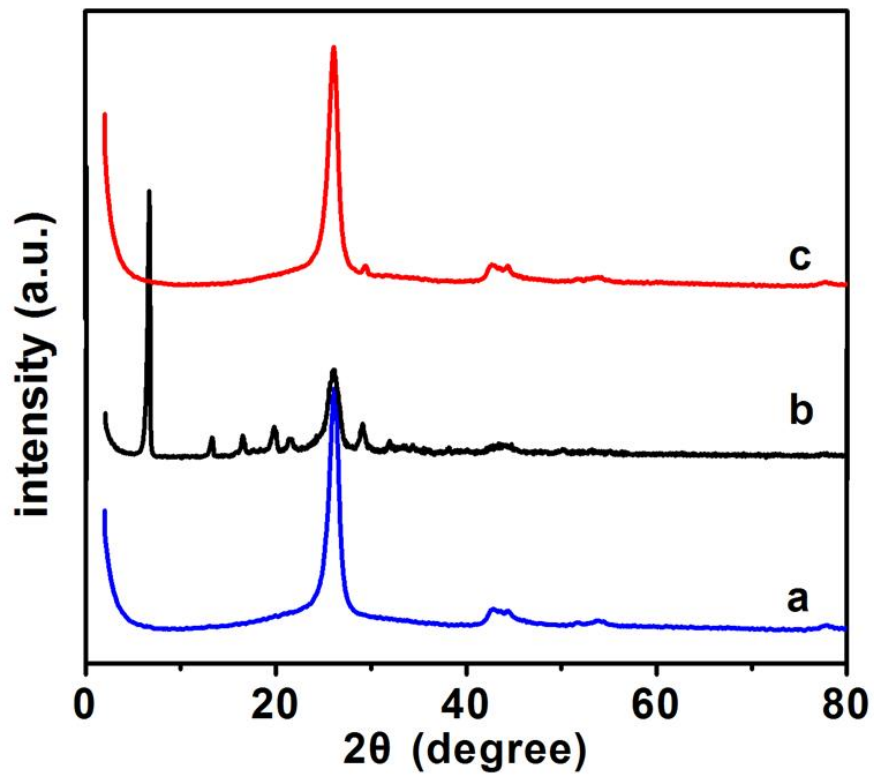
Fig. 3.2 XRD patterns of (a) CNT, (b) CaPP-CNT and (c) as-prepared HAp-CNT.

The formation of HAp-CNT nanocomposite was further identified by FTIR, and the results were displayed in Fig. 3.3. From the spectrum, one could see that the CNTs possessed the bands at 1396 cm^{-1} (Fig. 3.3a), which could be assigned to the absorption of C=C bond [28]. For the CaPP-CNT (Fig. 3.3b), the 1592 and 1490 cm^{-1} bands were assigned to the ring stretching vibration mode of phenyl groups. The bands at 1224, 1114 and 1028 cm^{-1} were the P-O stretching vibration mode of P-O-P group. The bands at 782 and 696 cm^{-1} were respectively to the deformation vibration modes of H-C-H and C-C-C groups of phenyl groups. These results suggested that the composite of CaPP-CNT had been successfully formed by the first step. After treating the CaPP-CNT with alkaline phosphatase, the bands for phenyl and P-O-C groups were completely diminished, suggesting the successful cleavage of phosphate group from the benzene ring. In addition, the new bands at 1097, 1036, 604 and 570 cm^{-1} appeared (Fig. 3.3c), that were in good accordance with pure HAp (Fig. 3.3d). According to the literature previously reported [32], the former two bands were assignable to the P-O stretching vibration mode of inorganic phosphate species, and the latter two were to the deformation vibration mode of O-P-O groups. These results proved that the transformation from the intermediate product of CaPP to HAp was achieved, and HAp-CNT nanocomposite was obtained at last.
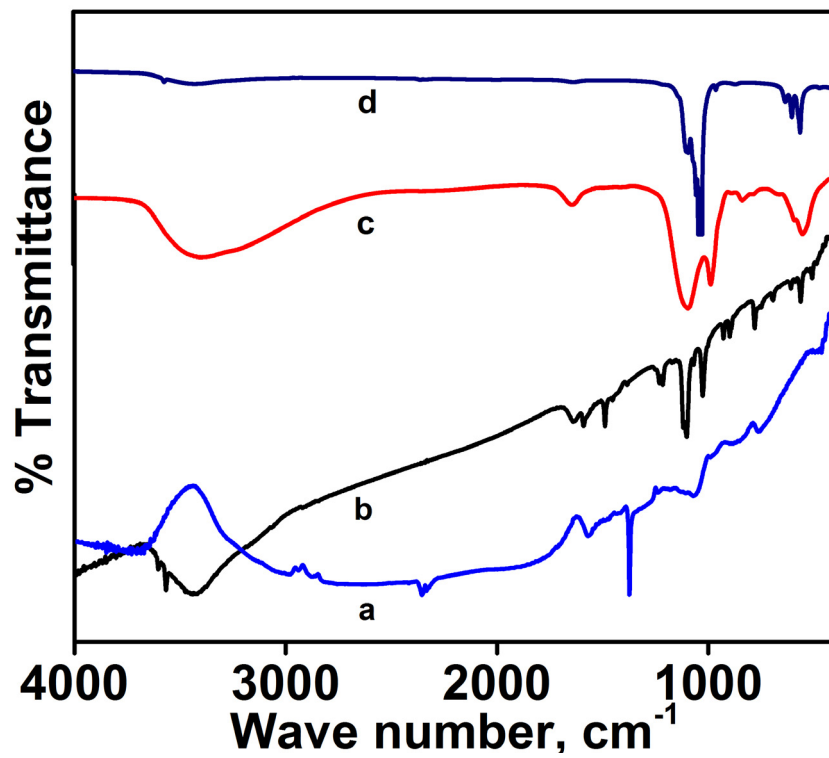
Fig. 3.3 IR spectra of (a) CNT, (b) CaPP-CNT, (c) as prepared HAp-CNT and (d) pure HAp.

3.3.2 Electrochemical behaviors of the modified electrodes

The electrochemical properties of the HAp-CNT were characterized through cyclic voltammograms (CV) and electrochemical impedance spectroscopy (EIS) using $[Fe(CN)_6]^{3-/4-}$ as the redox probe. Fig. 3.4A showed the CVs of different modified electrodes in 1.0 mM $[Fe(CN)_6]^{3-/4-}$ and 0.1 M KCl mixture solution. As seen, a pair of well-defined redox peaks corresponding to $[Fe(CN)_6]^{3-/4-}$ couple was observed on bare GCE (curve a) with a small peak-to-peak separation (ΔE_P) of 113 mV, showing that the cleaned GCE behaves as a good electron transfer interface. On HAp-CS/GCE, it was observed that the redox peaks of $[Fe(CN)_6]^{3-/4-}$ decreased and the peak-to-peak separation was enlarged obviously (curve b), indicating that HAp-CS has blocking effect toward the electrochemical reaction of $[Fe(CN)_6]^{3-/4-}$ due to their inferior electron conductivity, and the electrostatic repulsion of negative PO_4^{3-} and OH^- on HAp toward $[Fe(CN)_6]^{3-/4-}$. However, when HAp-CNT-CS/GCE was applied, it was found that the electrochemical response of $[Fe(CN)_6]^{3-/4-}$ apparently increased (curve c), demonstrating that the presence of CNT in the composite could improve the electron transfer rate of $[Fe(CN)_6]^{3-/4-}$.

Electrochemical impendence spectroscopy (EIS) is a convenient and sensitive method for monitoring the impedance change of the surface during the process of frequency variation, which offers various information of the interface between the electrode and the solution, including the electrode impedance, the capacity of the electric double layer, and the surface electron transfer resistance (R_{et}) [33]. A typical Nyquist plot commonly consisted of a semicircle portion at the higher frequencies relating to the electron transfer-limited process and a linear part at the lower frequencies corresponding to the diffusion process. The electron transfer resistance (R_{et}) could be directly reflected by the diameter of the semicircle in the higher frequency region. Fig. 3.4B showed the EIS of different electrodes in 1.0 mM $[Fe(CN)_6]^{3-/4-}$ and 0.1 M KCl solution. As well seen, a small R_{et} value of 630 Ω was obtained at bare GCE (curve a). When HAp-CS was modified on the electrode surface, the R_{et} value was significantly increased to 1462 Ω (curve b), indicating that the electron transfer

process of $[Fe(CN)_6]^{3-/4-}$ on the electrode surface was weakened by the HAp-CS film. When HAp-CNT-CS/GCE was applied, the R_{et} was dramatically decreased to 330 Ω (curve c), demonstrating the great enhancement of the electron transfer kinetic of the modified electrode due to the excellent electric conductivity of CNT. These results were in good accordance with those obtained from the CV experiments.
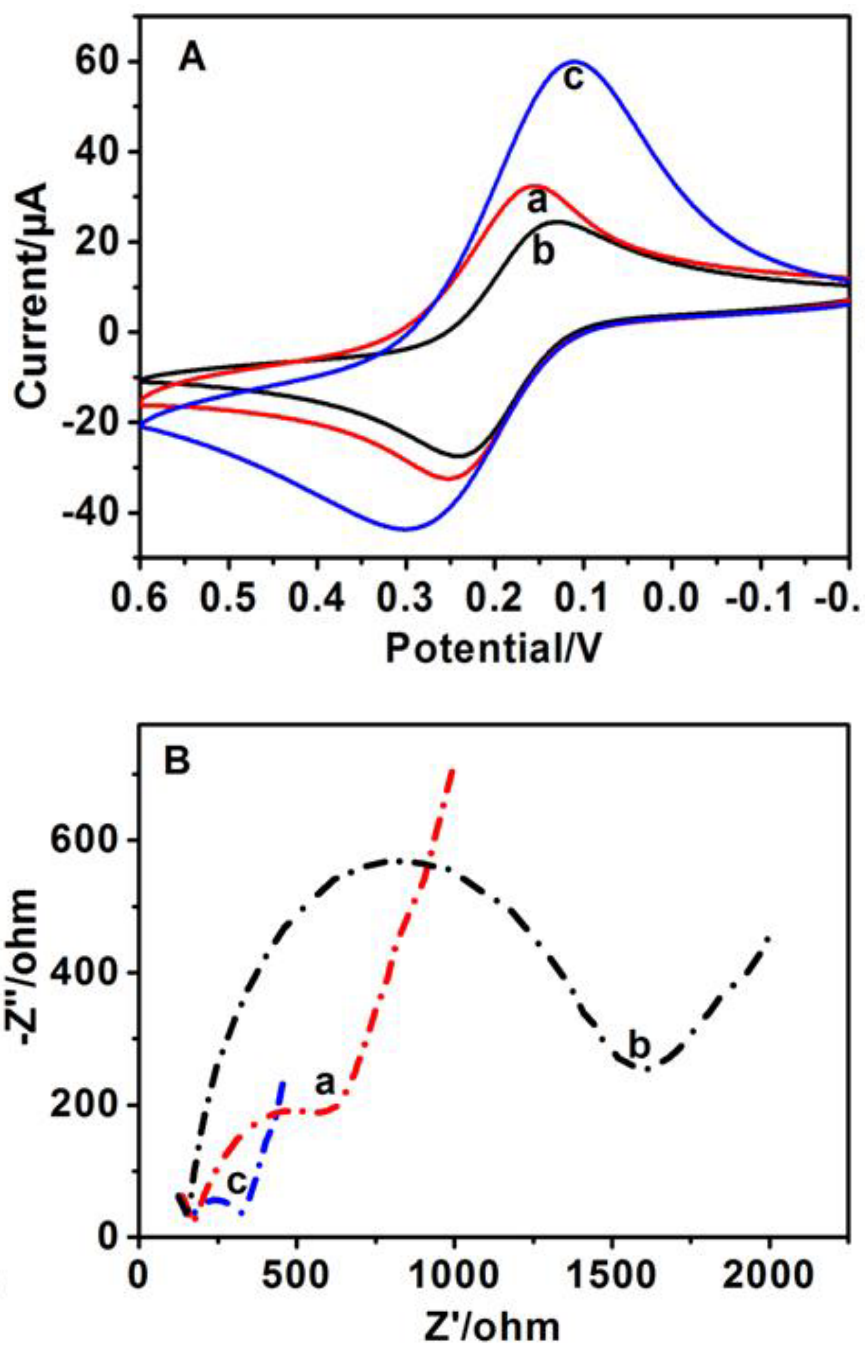
Fig. 3.4 CVs (A) and EIS (B) of (a) bare GCE, (b) HAp-CS/GCE and (c) HAp-CNT-CS/GCE in 1.0 mM $[Fe(CN)6]^{3-/4-}$ and 0.1 M KCl mixture.

3.3.3 Electrochemical behaviors of luteolin

Cyclic voltammograms of 3.0×10^{-6} M luteolin on different electrodes were recorded with the results shown in Fig. 3.5. It could be seen that a pair of well-defined redox peaks obtained on these different electrodes for luteolin solution, indicating that the redox reaction of LU had took place on these electrodes. Compared with the redox peak currents on bare GCE (curve a), the electrochemical responses on HAp-CS/GCE (curve b) was smaller, which indicated that the single HAp had blocking influence of luteolin because of its poor electron conductivity. However on CNT-CS/GCE (curve c), a large electrochemical response corresponding to the redox of luteolin appeared owning to the excellent electron conductivity of CNT. Interestingly, when HAp-CNT-CS/GCE was applied, it was found that the electrochemical signals of luteolin showed a further increase. This suggested that the CNT and HAp had a synergic effect on the signal amplification of luteolin, which could be explained by the bifunctional properties of HAp-CNT nanocomposite include high specific surface areas, particular multi-adsorbing sites, uniform and tailored nanostructure and excellent electrochemical properties. The oxidation peak potential (E_{pa}) and reduction peak potential (E_{pc}) were located at 0.584 V and 0.537 V, respectively. Then according to the formula of $\Delta E_p = |E_{pa} - E_{pc}| = 0.058/n$ V, the electron transfer number of luteolin at the electrode surface was calculated to be $1.2 \approx 1.0$, suggesting that luteolin underwent a single electron transfer process in this work.

In addition, the surface adsorption amounts of CNT-CS/GCE, HAp-CS/GCE, and HAp-CNT-CS/GCE were calculated according to charge integration of cathodic peak in the CV and following Laviron's equation (1) [34]:

$$I_p = \frac{n^2 F^2 v A \Gamma}{4RT} = \frac{nFQv}{4RT} \tag{1}$$

where Γ is the surface adsorption amount, Q the charge of the reduction process, n the electron transfer number, F the Faraday, A the electrode geometric area and the Γ values of luteolin on the CNT-CS/GCE ($I_p = 2.27$ μA), HAp-CS/GCE ($I_p = 0.57$ μA), and

HAp-CNT-CS/GCE (I_p=4.1 μA) were estimated to be 3.85×10^{-9} mol cm^{-2}, 0.86×10^{-9} mol cm^{-2} and 7.47×10^{-9} mol cm^{-2}. Through comparison, it was very clearly that the Γ on HAp-CNT-CS/GCE was about two times of that on CNT-CS/GCE. It was further confirmed that the multiple adsorption sites of HAp could greatly improve the adsorption amount of luteolin, and as a consequence, the electrochemical response of luteolin on HAp-CNT-CS/GCE was greatly enhanced.
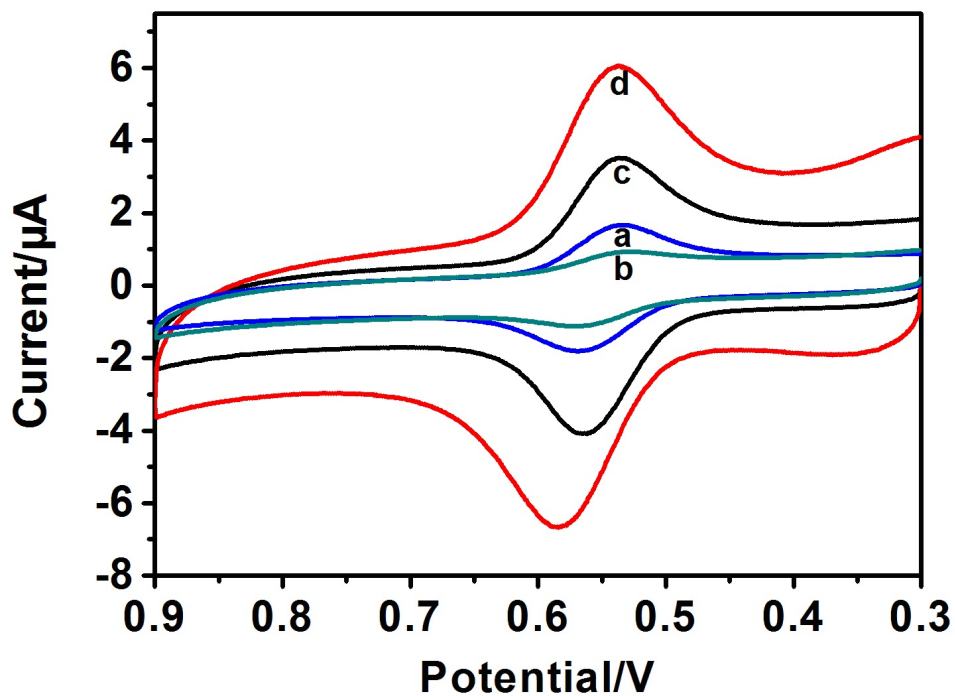
Fig. 3.5 CVs of 3.0×10⁻⁶ M luteolin at (a) bare GCE, (b) HAp-CS/GCE, (c) CNT-CS/GCE and (d) HAp-CNT-CS/GCE in pH 2.0 PBS. Scan rate: 0.1 V s⁻¹.

3.3.4 Optimization of the experimental conditions

In order to obtain optimal electrochemical response of luteolin on HAp-CNT-CS/GCE, several conditions that could influence the electrochemical behavior of luteolin were optimized. Fig. 3.6A showed the oxidation peak currents of luteolin in different supporting electrolytes including Tris-HCl, B-R and PBS. It was found luteolin had the largest reduction peak current in PBS solution as compared to B-R and Tris-HCl buffer solution with the same pH value and concentration. Therefore, PBS was used as the supporting electrolyte in this experiment. Fig. 3.6B displayed the relationship between reduction peak currents and accumulation potential (E) ranging from 0.1 V to 0.6 V. Obviously, when the potential increased to 0.4 V the peak current value reached the maximum value and hardly changed with further increase of the potential. So, 0.4 V was selected as the optimal potential for detection in the following experiments. The optimal accumulation time (t) of the modified electrode with luteolin was also investigated and the results were shown in Fig. 3.6C. It was clear that for the first 150 s, the peak current value changed sharply, and after this point the peak current increased very little, which indicated that the accumulation saturation could be completed within about 150 s. Therefore, 150 s was chosen as the accumulation time.
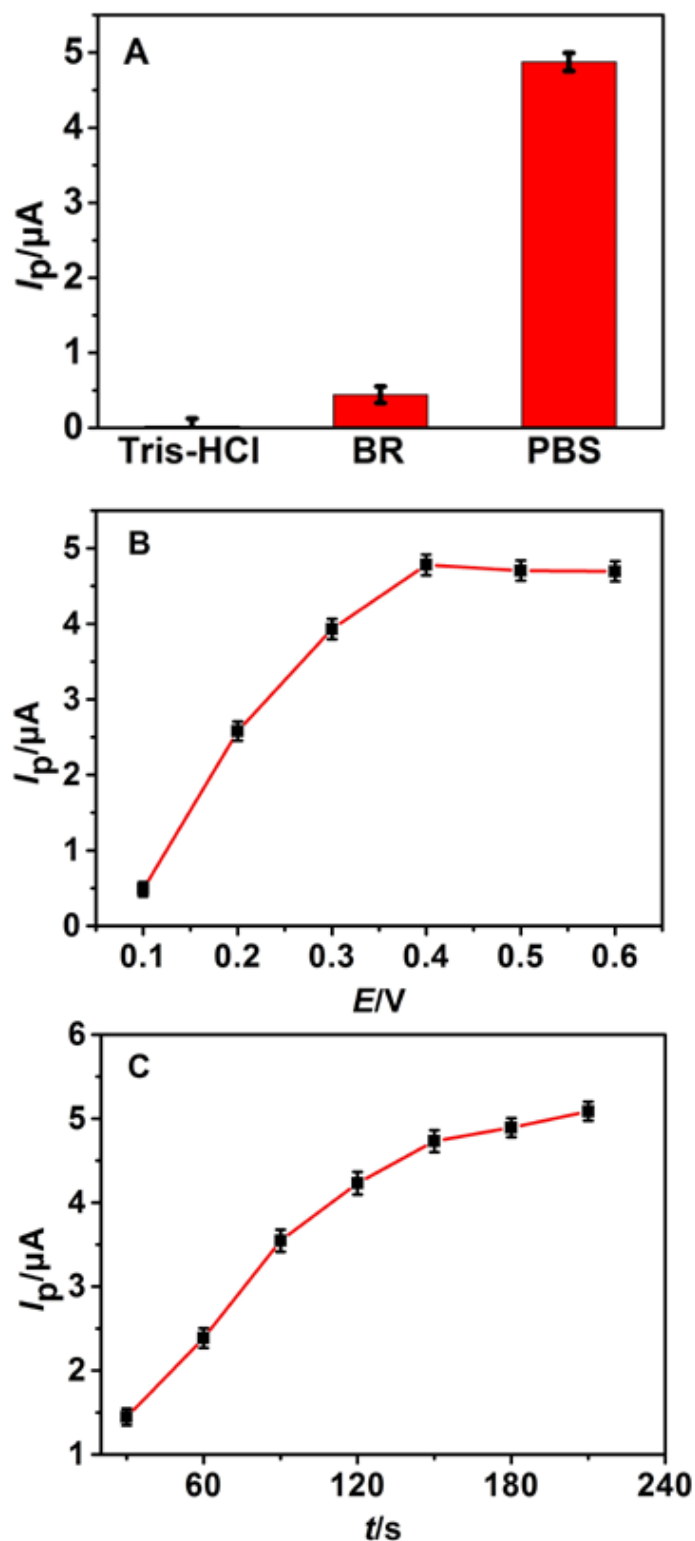
 Fig. 3.6 The reduction peak current (I_p) of $3.0×10^{-6}$ M luteolin in different

supporting electrolytes including Tris-HCl, B-R and PBS (A).

Relationships of I_p with E (B) and t (C).

In this work, the effect of the pH values of the PBS buffer on the electrochemical behaviors of 3.0×10^{-6} M luteolin were also investigated and the results were shown in Fig. 3.7A. Fig. 3.7B showed the relationships between the reduction peak current and the formal potential with buffer pH. It could be seen clearly that the reduction peak currents (I_p) increased with the decrease the pH values until it reached 2.0 and then decreased when the pH was further decreased. Therefore, pH 2.0 was selected as the optimal pH for detection in the following experiments. And the redox peak potential shifted to the negative direction with the increase of buffer pH, indicating that protons took part in the electrode reaction. The relation between the formal peak potential ($E^{0'}$) and pH was calculated as $E^{0'}/V=0.67-0.069$ pH ($r=0.998$). The slope value of -69 mV/pH was close to theoretical value of -59 mV/pH, indicating that the ratio of electron and proton number taking part in the electrode reaction was 1:1. So it could be concluded that underwent a one-electron and one proton in the acid medium, which was consistent with the result reported in the literature [10]. Therefore the electrochemical reaction mechanism of luteolin on the fabricated electrode could be described as the following Scheme 3.2.
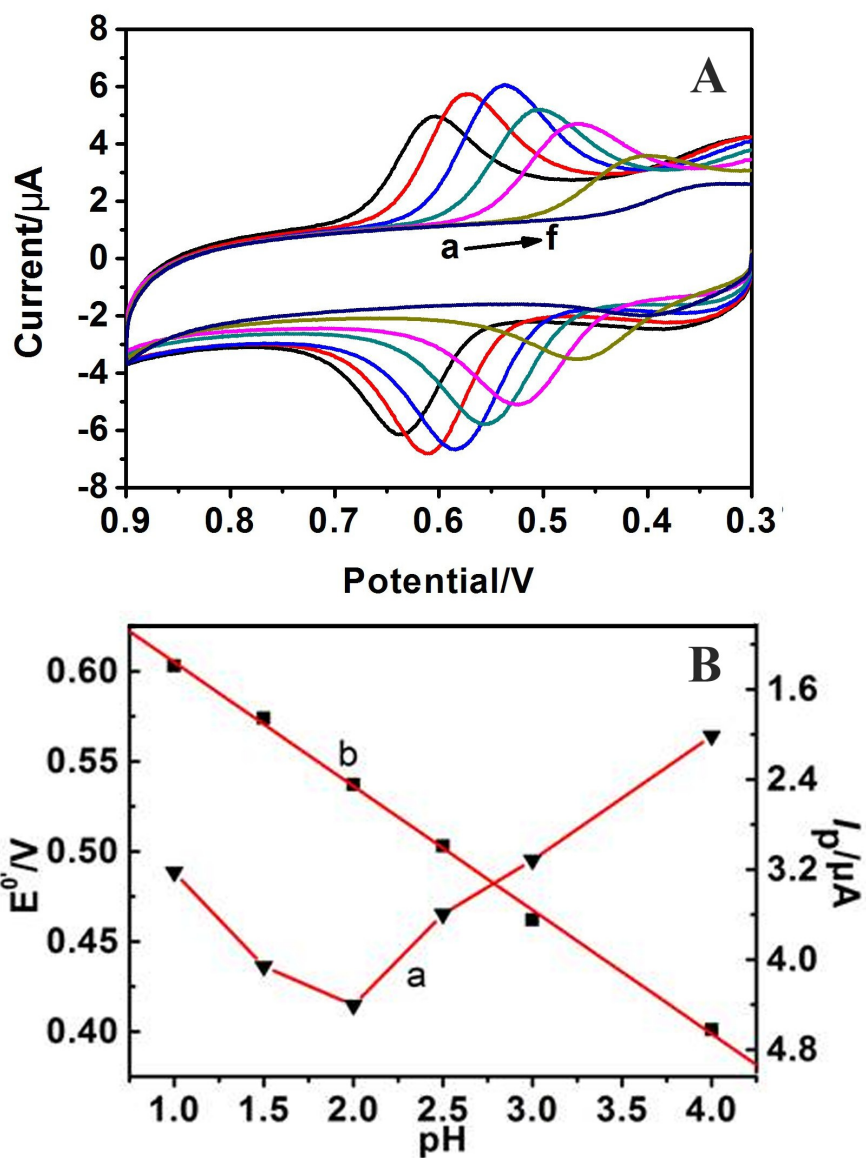
Fig. 3.7 Cyclic voltammograms of 3.0×10^{-6} mol L^{-1} luteolin on HAp-CNTs-CS/GCE with different pH PBS (from a to f are 1.0, 1.5, 2.0, 2.5, 3.0, 4.0, and 5.0, respectively) (A), Inset: the relationship between the formal potential ($E^{0'}$) and I_p versus pH (B).
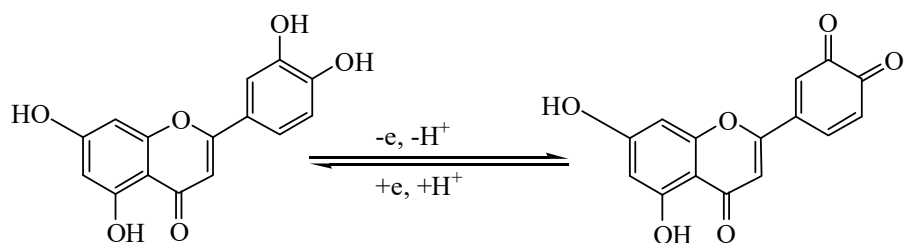
Scheme 3.2 Chemical structure and oxidation mechanism of luteolin.

3.3.5 Electrochemical parameters of luteolin at HAp-CNT-CS/GCE

The influence of scan rate on the electrochemical response of 3.0×10^{-6} M luteolin on HAp-CNT-CS/GCE was recorded with the results shown in Fig. 3.8. The redox peak current increased gradually with the increase of scan rate in the range from 0.01 to 0.50 mV s^{-1} along with the shift of redox peak potential, suggesting the quasi-reversible electrochemical process of luteolin at the modified electrode. Good linear relationships between the redox peak currents (I_p) and the scan rate (v) were plotted (Fig. 3.9) with the regression equations of I_{pa}/μA=-26.21 v/(V s^{-1})-0.69 and I_{pc}/μA=24.80 v/(V s^{-1})+0.23 with the correlation coefficients (r) of 0.995 and 0.998, respectively. These results indicated that the electrochemical behavior of luteolin on the modified electrode was a typical thin layer surface-controlled process.

Additionally, the relationships of the redox peak potentials (E_p) with the scan rate were applied to calculate the electron transfer kinetic parameters with the following Laviron's equations (2-4) [34]:

$$E_{pa} = E^{0'}+2.3RT/(1-\alpha)nF \log v \tag{2}$$

$$E_{pc} = E^{0'}-2.3RT/\alpha nF \log v \tag{3}$$

$$\log k_s = \alpha\log (1-\alpha)+ (1-\alpha)\log \alpha - \log (RT/nF)-(1-\alpha) \alpha nF\Delta E_p/2.3RT \tag{4}$$

Where k_s is standard electron transfer rate constant, α the electron transfer co-efficient, and the other symbols are the same to equation (1). The linear relationships between the E_{pa} and E_{pc} with the log v were established to be E_{pa}/V=0.01015 log v/(V s^{-1})+0.58905 (r=0.988) and E_{pc}/V=-0.00863 log v/(V s^{-1})+0.52924 (r=0.991) (Fig. 3.10). Then according to equations (1) and (2), the α could be calculated as 0.54. Further, based on the equation (3), the value of k_s was calculated to be 3.4 s^{-1}.
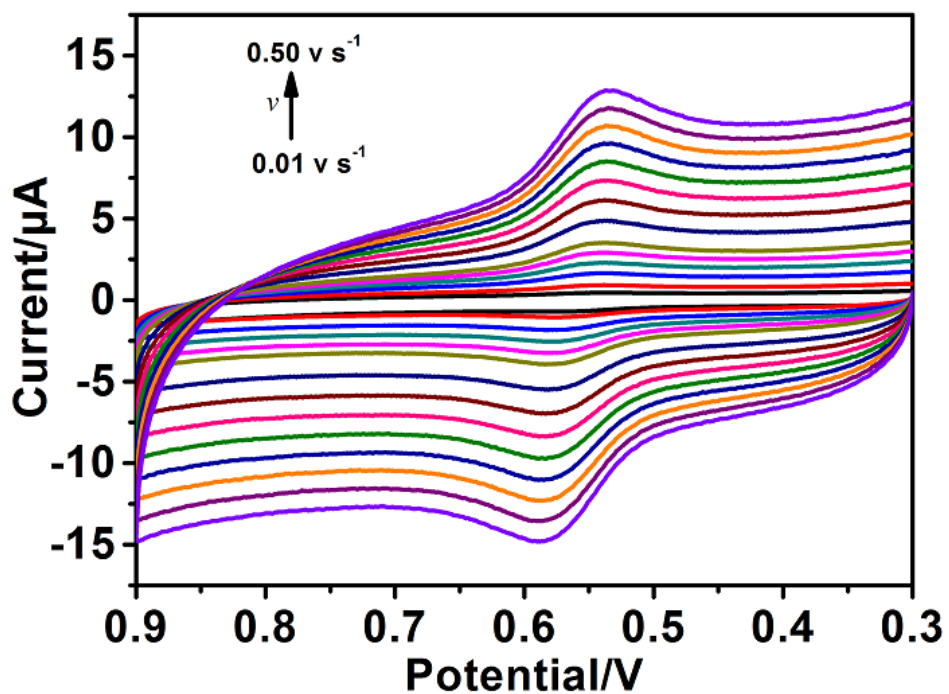
Fig. 3.8 Cyclic voltammograms of 3.0×10^{-6} M luteolin with different scan rate (v) on HAp-CNTs-CS/GCE in pH 2.0 PBS (from a to n are 10, 20, 40, 60, 80, 100, 150, 200, 250, 300, 350, 400, 450, 500 mV/s, respectively.
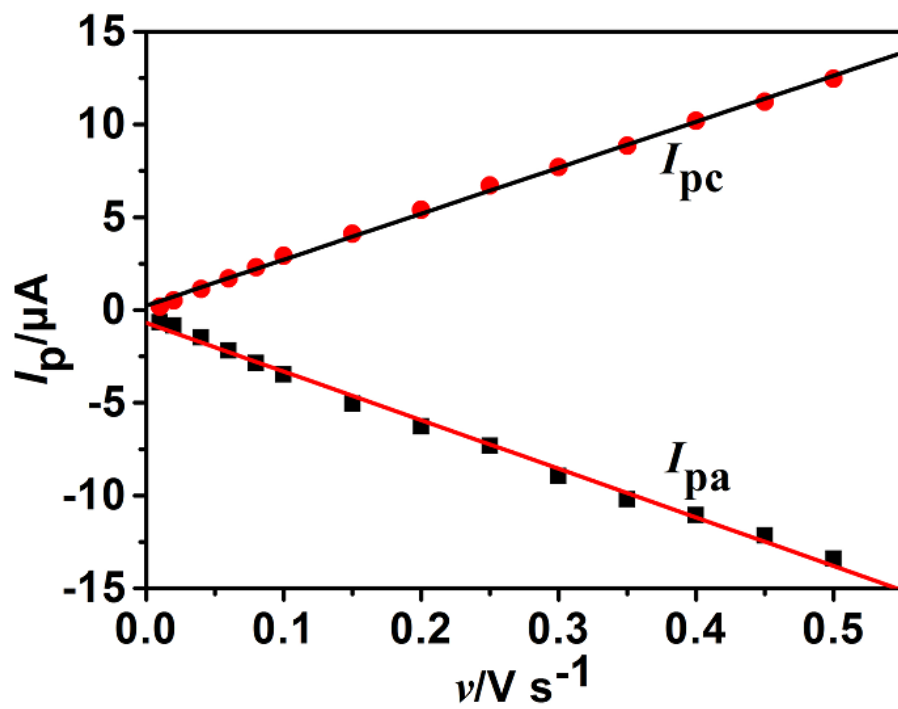
Fig. 3.9 Linear relationships of (I_{pc}) and (I_{pa}) versus v.
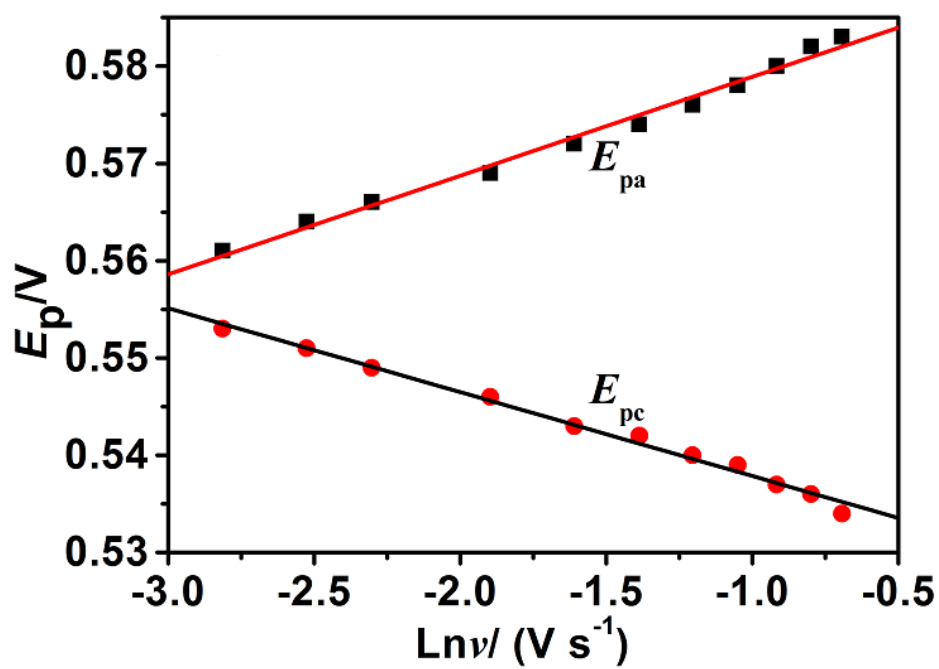
Fig. 3.10 Linear relationships of the peak potential E_{pa} and E_{pc} versus Lnv.

3.3.6 Analytical performance

DPV is a convenient electrochemical technique, which offers more advantages for the quantitative analysis than CV due to its merits of lower capacitative and smaller background currents, as well as the higher current sensitivity [35]. Therefore, in order to probe the analytical performance of the modified electrode, DPV was applied in the following quantitative tests. Fig. 3.11A showed the dependence of the DPVs on the concentrations of luteolin ([luteolin]) under the optimal conditions. It was found that the reduction peak increased gradually with the increase of the luteolin concentrations, and a good linearity was observed between I_{pc} and [luteolin] over the rang from 4.0×10^{-7} M to 1.2×10^{-5} M, $I_{pa}/\mu A = 0.8148$ [luteolin]$/\mu M - 0.1783$ (r=0.992) (Fig. 3.11B). Based on the signal-to-noise ratio (S/N) of 3, the detection limit was estimated to be 8.0×10^{-8} M.

Additionally, a relative standard deviation of 8.5% for 3.0×10^{-6} M luteolin (n=5) suggested that the HAp-CNT-CS modified electrode possess good reproducibility. Six electrodes fabricated independently were used to determine 3.0×10^{-6} M luteolin, and relative standard deviation was 7.0%, revealing an excellent repeatability of the electrode preparation. The stability of the film electrode was evaluated by measuring the peak current of 3.0×10^{-6} M luteolin repeatedly. It was found that after 50-times test, the peak current deviated from its original response only 6.6%.
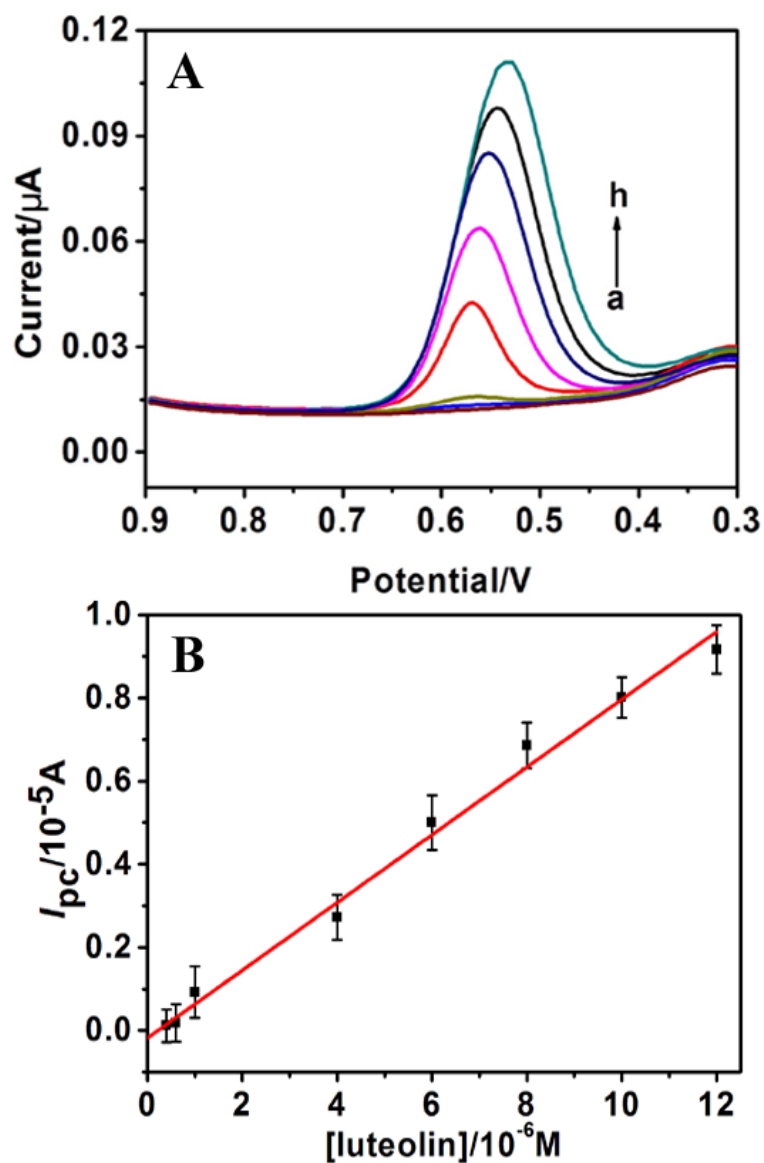
Fig. 3.11 DPVs of 0 (a), 0.4×10^{-6} M (b), 1.0×10^{-6} M (c), 4.0×10^{-6} M (d), 6.0×10^{-5} M (e), 8.0×10^{-6} M (f), 1.0×10^{-5} M (g), 1.2×10^{-5} M (h) luteolin in pH 2.0 PBS on HAp-CNTs-CS/GCE. (B) Linear relationship between I_p and the concentrations of luteolin [luteolin].

3.3.7 Interference study

The potential interference for the determination of luteolin was studied. Under the optimized conditions, the oxidation peak of 3.0×10^{-6} M luteolin was individually measured in the presence of different concentrations of the common interferents, and then the change of peak current was checked. It was found that 1.0×10^{-5} M K^+, 1.0×10^{-5} M Na^+, 1.0×10^{-5} M Cd^{2+}, 1.0×10^{-5} M Mg^{2+}, 1.0×10^{-5} M Ca^{2+}, 1.0×10^{-5} M Cu^{2+}, 1.0×10^{-5} M Mn^{2+}, 1.0×10^{-5} Cl^-, 1.0×10^{-5} NO_3^-, 1.0×10^{-5} M CO_3^{2-}, 1.0×10^{-5} SO_4^{2-}, 1.0×10^{-5} citric acid, 1.0×10^{-5} glycine, 1.0×10^{-5} lysine, 1.0×10^{-5} folic acid, 1.0×10^{-5} gluconic acid almost have no influence on the detection of luteolin since the peak current change was below 5%, revealing that this sensor has good selectivity for luteolin determination.

3.4 Conclusions

In this chapter, the nanocomposite of HAp-CNT was synthesized by an alkaline phosphatase assisted hydrolysis reaction. Then the GCE interface anchored with a nanocomposite of HAp-CNT-CS was developed for examining the electrochemical behaviors of luteolin. Electrochemical characterization experiments showed that HAp-CNT-CS/GCE could greatly enhance the electrochemical signal of luteolin as compared to bare GCE and other modified electrodes. This work opens a new way for the synthesis of HAp-CNT composite and broadens the application of the composite material.

3.5 References

[1] A.Y. Tesioa, A.M. Graneroa, N.R. Vettorazzia, N.F. Ferreyrab, G.A. Rivasb, H. Fernándeza and M.A. Zona, *Micro. Chem. J.* **115** (2014) 100-105.

[2] M.L. Neuhouser, *Nutr. Cancer* **50** (2004) 1-7.

[3] C.J. Wruck, M. Claussen, G. Fuhrmann, L. Römer, A. Schulz, T. Pufe, V. Waetzig, M. Peipp, T. Herdegen and M.E. Götz, *J. Neural Transm.* **72** (2007) 57-67.

[4] Y. Lin, R. Shi, X. Wang and H.M. Shen, *Curr. Cancer Drug Targets* **8** (2008) 634-646.

[5] L.P. Li, H.D. Jiang, H.H. Wu and S. Zeng, *J. Pharm. Biomed. Anal.* **37** (2005) 615-620.

[6] S.A.O. Santos, C.S.R. Freire, M.R.M. Domingues, A.J.D. Silvestre and C.P. Neto, *J. Agric. Food. Chem.* **59** (2011) 9386-9393.

[7] Y.Y. Li, Q.F. Zhang, H.Y. Sun, N.K. Cheung and H.Y. Cheung, *Talanta* **105** (2013) 393-402.

[8] Y.Y. Peng, J.N. Ye and J.L. Kong, *J. Agr. Food Chem.* **53** (2005) 8141-8147.

[9] I. Baranowska and D. Raróg, *Talanta* **55** (2001) 209-212.

[10] P. Pang, Y. Liu, Y. Zhang, Y. Gao and Q. Hu, *Sens. Actuators B Chem.* **194** (2014) 397-403.

[11] K. Kandori, A. Yasukawa and T. Ishikawa, *Chem. Mater.* **1** (1995) 26-32.

[12] J.P. Gittings, C.R. Bowen, A.C.E. Dent, I.G. Turner, F.R. Baxter and J.B. Chaudhuri, *Acta Biomater.* **5** (2009) 743-754.

[13] B. Singh, S. Kumar, B. Basu and R. Gupta, *Mater. Lett.* **95** (2013) 100-102.

[14] A.A. White and S.M. Best, *International Journal of Applied Ceramic Technology*, **4** (2007) 1-13.

[15] X. Wei and M.Z. Yates, *Chem. Mat.*, **24** (2012) 1738-1743.

[16] S. Iijima, *Nature*, **354** (1991) 56-58.

[17] H. Tak, C.S. Ha, H.J. Lee, H.W. Lee, Y.K. Jeong and M.C. Kang, *Trans. Nonferrous Met. Soc. China* **21** (2011) 28-32.

[18] H. S. Han, J.M. You, H. Seol, H. Jeong and S. Jeon, *Sensor. Actuat. B-Chem.* **194**

(2014) 460-469.

[19] M. Cui, J. Huang, Y. Wang, Y. Wu and X. Luo, *Biosens. Bioelectron.* **68** (2015) 563-569.

[20] C. Chen, W. Zhang, B. Zhao and Y. Zhang, *Physics Letters A*, **374** (2009) 309-312.

[21] H. Ishiwara, *Curr. Appl. Phys.* **9** (2009) S2-S6.

[22] N. Doostani, S. Darbari, S. Mohajerzadeh and M.K. Moravvej-Farshi, *Sensor. Actuat. A-Phys.* **201** (2013) 310-315.

[23] Z. Ozturk, C. Baykasoglu, A. T. Celebi, M. Kirca, A. Mugan and A. C. To, *Int. J. Hydrogen. Energ.* **40** (2015) 403-411.

[24] A. Ranjbar, M. Ismail, Z.P. Guo, X.B. Yu and H.K. Liu, *Int. J. Hydrogen. Energ.* **35** (2010) 7821-7826.

[25] A. Safavi, M. Sorouri and P. Khanipour, *Electroanal.* **26** (2014) 359-365.

[26] J. Li , D. Kuang, Y. Feng, F. Zhang and M. Liu, *Microchimi. Acta* **176** (2012) 73-80.

[27] H.Y. Zhao, H.M. Zhou, J.X. Zhang, W. Zheng and Y.F. Zheng, *Biosens. Bioelectron.* **25** (2009) 463-468.

[28] S. Mukherjeea, B. Kundub, A. Chandac and S. Senc, *Ceram. Int.* **41** (2015) 3766-3774.

[29] H. Tanaka and D. Ihata, *Mater. Res. Bull.* **45** (2010) 103-108.

[30] J.A.S. Bett, L. G. Christner and W.K. Hall, *J. Am. Chem. Soc.*, **89** (1967) 5535-5541.

[31] J. Rodrigues, D. Mata, A. Pimentel, D. Nunes, R. Martins, E. Fortunato, A.J. Neves, T. Monteiro and F.M. Costa, *Mat. Sci. Eng. B* **195** (2015) 38-44.

[32] V.B. Buenoa, R. Bentinia, L.H. Catalania, L.R.S. Barbosab and D.F.S. Petria, *Mat. Sci. Eng. B* **37** (2014) 195-203.

[33] G. Li, X. Li, J. Wan and S. Zhang, *Biosens. Bioelectron.* **24** (2009) 3281-3287.

[34] E. Laviron, *J. Electroanal. Chem. Interfac.* **101** (1979) 19-28.

[35] E. Laborda and F. Martínez-Ortiz, Á. Molina, *Electrochim. Acta* **56** (2011) 5335-5342.

Chapter 4

Hydroxyapatite Synthesis-triggered Reduction of Graphene Oxide under Moderate Temperature Environment and the Electrochemical Sensing Application of Their Composite

4.1 Introduction

As a major component of biological hard tissues in animal organism, HAp has multiple unique properties, such as good biocompatibility/bioactivity, abundant adsorption site, strong adhesive ability, diverse preparation route, and so on. In view of these merits, much effort has been made to broaden the application of HAp, especially in biological, medical and chemical areas [1-3]. But, the poor tensile strength, fracture toughness, and low electronic conductivity of pure HAp crystals limit their application in wider fields. In order to address these problems, a number of other materials, such as polymers [4], carbonaceous nanomaterial [5], metal/metal oxide [6, 7], or organic molecule [8] have been used as modifier to improve the performance of HAp.

Carbonaceous materials, from fullerene to carbon nanotubes, and then to graphene, are always the research concerns in the fields of chemistry, physics and medicine in the past decades, due to their merits of low toxicity, abundance in earth, and outstanding optical and electrochemcial properties [9, 10]. Graphene oxide (GO), a two-dimensional (2D) nanostructure that is first prepared about 150 years ago [11], is particularly attractive for both theoretical and the experimental scientists, especially after the discovery of graphene in 2004 [12]. Their excellent hydrophility, high surface-to-volume ratio, easy preparation route, rich functional groups and outstanding optical property endow them many emerging applications, such as biomolecule sensing [13], drug screening and delivery [14,15], energy storage/conversion [16] and cell imaging [17]. Besides these, the researchers have also applied GO as the biosensing platforms based on the fact that its bearing groups of carboxyl, hydroxy, and epoxy, facilitate it to graft the biorecognition or biocatalytic elements such as DNA [18], aptamers [19] and enzymes [20]. However, the pristine GO has large amounts of disrupted sp^2 bonding networks because of the derivative oxygen-bearing groups, leading to poor electronic conductivity, especially in comparison with its reduction form (rGO). This defect seriously blocks the practical application of the material, especially in the electrochemical field.

Up to date, lots of strategies including as electrochemical reduction [21, 22], microwave irradiation [23], photocatalytic reduction [24], thermal treatment [25] and chemical reaction [26-31] have been developed for the transformation of GO to the reduced counterpart. Among these methods, the chemical reduction based on the reducing agents of hydrazine or hydrazine hydrate is mostly utilized, since the synthesis route of such method is mature, and the reduction efficiency by the method is relatively high. Nevertheless, because the reducing agents of hydrazine and its derivative are highly toxic and explosive, a mountain of work have been done by researchers to screen the safe, environmental-friendly and energy-efficient reduction reagents. For example, Chen et al. [26] have studied the feasibility of a series of sulfur-containing compounds for the reduction of GO, and have found that the less toxic and nonvolatile $NaHSO_3$ can also be an effective reducing agent to prepare rGO. In addition to this, the other reagents such as amino acid [27], hydroquinone [28], lithium aluminium hydride (LAH) [29], sodium borohydride ($NaBH_4$) [30] and ascorbic acid [31] have also been studied. These protocols are all promising to reduce GO as the alternatives of hydrazine reduction, but they still have some disadvantages. For example, the reducing ability of hydroquinone and amino acid are relatively weak, which decreases the efficiency for reduction reaction. In contrast, the extremely strong reducing reagents of LAH and $NaBH_4$ should have excellent ability for GO reduction, but the side reactions of these reducing agents with solvents (commonly water) remain a great challenge for their practical operation [32].

On the other hand, the simple reduction of GO by these chemical reducing agents only leads to the single-component rGO material, which has several structure and property defects. First, the sp^3 structure on pristine GO is changed to the sp^2 bonding networks through the chemical reduction process, and thus the strong π-staking and/or van der Waals interactions among the rGO sheets easily results in their tendency to irreversibly aggregate and even restore to graphite in solvents. Second, the lack of the functional groups on the pure rGO greatly limits its extending in functionality, such as absorptive capacity to small molecules and grafting ability to the biomolecules. It is fortunate that both of the two disadvantages of single-component rGO can be well

addressed through chemical modification of rGO with functional materials/molecules of metal nanoparticles [33, 34], polymers [35], aromatic molecules [36], and biomolecules [37]. These molecules, covalently or non-covalently bound on the surface of rGO, can act as an effective protector to prevent the aggregation of rGO, to enhance the dispersing ability of rGO. Furthermore, the functionality of the rGO can be further extended by the addition of these functional molecules, which is very beneficial to improve application of rGO in the fields of catalysis, biosensing, bioimaging, drug delivery, and so on [38]. But almost all the rGO-based nanocomposites are synthesized through two strategies, *i.e.*, (1) the chemical grafting or physical adsorption of functional molecules on GO surface, and then reduction of GO to rGO form under the assist of reducing agents; (2) the GO is reduced first, and is then interacts with functional molecules via the non-covalent interaction. Therefore, the pre- or post- reduction of GO is indispensable in these approaches, which increases the time- and labor- consumption for the synthesis of the rGO-based nanocomposites.

Herein, we reported that when HAp was to be *in-situ* prepared on GO surface through chemical wet-method under a relatively low temperature situation (85 °C), the GO was unexpectedly changed to rGO without adding any reducing reagent or high-temperature thermal treatment, and the nanocomposite of HAp-rGO was synchronously formed (Scheme 4.1). The process and product were systematically testified by the techniques of X-ray diffraction (XRD), Raman, Fourier transform infrared (FTIR), and electrochemistry. To further explore the potential application of the HAp-rGO composite, the obtained composite material was cast on a glassy carbon electrode (GCE) to prepare a modified electrode, and then used as an electrochemical sensor for the determination of hydrazine (Scheme 4.2). The control experiments showed that the composite modified electrode presented higher catalytic activity toward the oxidation of hydrazine than the single-component counterpart of HAp and GO, suggesting that the composite combined the advantages of HAp with rich active sites strong adsorbing ability and rGO with large surface area and high electronic conductivity. The constructed sensor has also revealed excellent anti-inference ability

and fast electrochemical response in chronoamperometry, showing great promising of the sensor for the detection of hydrazine.
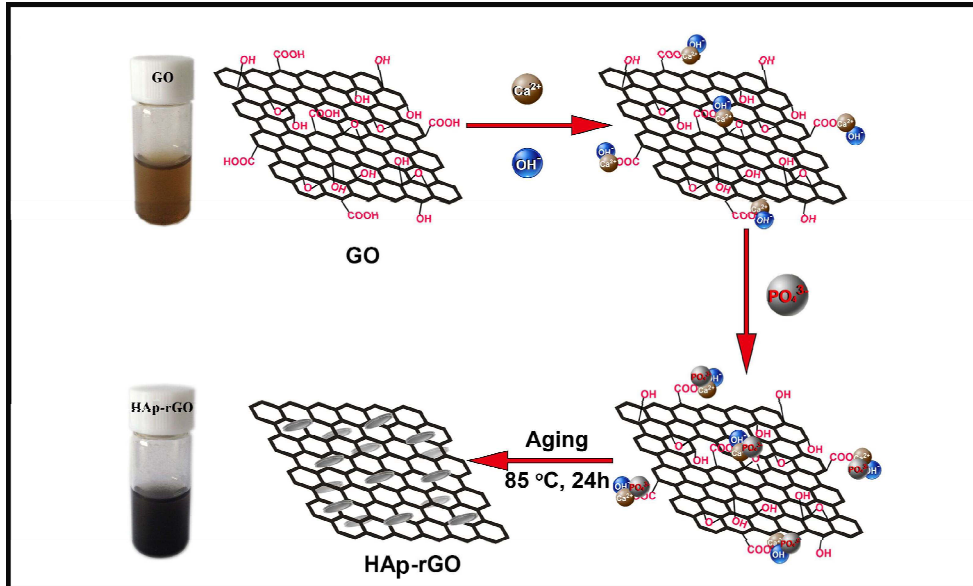
Scheme 4.1 Diagram for the synthesis process of HAp-rGO.
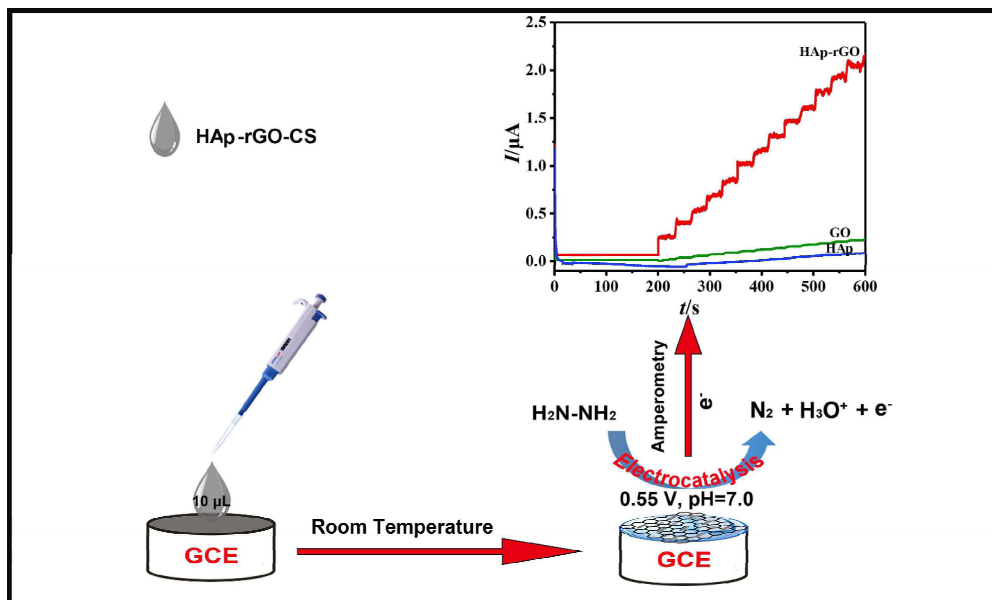
Scheme 4.2 Diagram for the application of HAp-rGO for electrochemical sensing detection of hydrazine.

4.2 Experimental

4.2.1 Materials and apparatus

Hydrazine was purchased from Sigma-Aldrich Co., Ltd. (China). Calcium hydroxide ($Ca(OH)_2$) and phosphoric acid (H_3PO_4) were provided by Wako Pure Chemical Industries Co., Ltd. (Japan). Glucose, acetic acid (AcA), methanol, hydrogen peroxide (H_2O_2), formic acid (FA), ethanol, $K_3(Fe(CN)_6)$, $K_4(Fe(CN)_6)$, KCl, graphite, $NaNO_3$, $KMnO_4$ were obtained from Xilong Chemical Co., Ltd. (China). Ascorbic Acid (AA) was purchased from Sinopharm Chemical Reagent Co., Ltd. (China). Uric Acid (UA) was supplied by Sangon Bioengineering Co. Ltd. (China). Glutathione (GSH) was purchased from Tokyo Chemical Industry (Japan). 25 mM phosphate buffered solution (PBS, pH 7.0) was purchased from Shanghai KangYi Instruments Co., Ltd. (China). Dopamine hydrochloride (DA), citric acid (CA), chitosan (CS) and urea were purchased from Aladdin Reagent Co., Ltd. (China). All the other chemicals were of analytical reagent grade and obtained commercially. Doubly distilled water was used throughout the experiments.

Powder X-ray diffraction (XRD) patterns of the materials were recorded on a Rigaku diffractometer with a Ni-filtered Cu K_α radiation (30 kV and 16 mA, Japan). Morphologies of the synthesized materials were observed by a TOPCON transmission electron microscope (TEM, Japan). Transmission IR spectra were recorded by a KBr method using a JASCO Fourier transform infrared (FTIR) spectrometer with a resolution of 4 cm^{-1} (Japan). Raman spectra were collected at a confocal Raman microscopy system (inVia Renishaw, UK). Electrochemical measurements were carried out on a CHI 650C electrochemical analyzer (China) in connection with a conventional three-electrode system: a glassy carbon electrode (GCE, diameter=2 mm) modified with different materials was used as the working electrode, Ag/AgCl electrode as the reference electrode, and Pt wire as the counter electrode.

4.2.2 Preparation of HAp-rGO nanocomposite

The GO was first prepared according to a modified Hummer's method using graphite power as starting material, and the detailed synthesis process has been given in our previous literature [39]. Then 0.125 mg GO was dispersed in 2.0 L doubly distilled water free from CO_2 in a sealed polypropylene vessel and ultrasonicated for 2 h to obtain the homogeneous dispersion. Followed by, 2.889 g (0.039 mol) of $Ca(OH)_2$ were added into the dispersion, and after 1 h of stirring at room temperature, 16.7 mL 10% H_3PO_4 solution were further added. The mixture was further stirred for 1 h at room temperature, and then aged in an air oven at 85 °C for 24 h. Finally, the precipitate was filtered off, thoroughly washed with doubly distilled water and dried in an air oven at 85 °C overnight to obtain the product. For comparison, pure HAp was also prepared by the similar method, but without adding GO during the synthesis process.

4.2.3 Fabrication of HAp-rGO modified electrode

A GCE surface was polished to mirror-like with 1.0, 0.3, and 0.05 μm alumina slurry, and then sonicated in ethanol and doubly distilled water for 5 min to achieve a cleaned GCE. The nanocomposite of (Chitosan) CS and HAp-rGO (HAp-rGO-CS) was prepared by adding 1.0 mg of HAp-rGO into 10 mL 1.0% AcA solution containing 0.3 wt% CS, and then ultrasonicating for 1 h under 80 W. Followed by, 10 μL of the prepared homogeneous HAp-rGO-CS dispersion was cast onto the above cleaned GCE surface. After dryness under room temperature, the modified electrode was carefully rinsed with doubly distilled water to remove the loosely adsorbed material, and thus the modified electrode of HAp-rGO-CS/GCE was achieved. For comparison, the control electrodes of HAp-CS/GCE and GO-CS/GCE were also prepared by the same procedures.

4.3 Results and discussion

4.3.1 Characterization of HAp-rGO nanocomposite

The phase composition and structure of the product obtained from *in-situ* synthesis of HAp on the surface of GO were characterized by XRD, FT-IR and Raman spectra. Fig. 4.1 shows the typical XRD pattern of GO, HAp and their composite. As seen, the GO synthesized through chemical oxidation method has a typical characteristic peak at $2\theta=10.17°$ (pattern a), attributing to the (002) lattice plane [40]. Another peak at $2\theta=23.5°$ is ascribed to the natural graphite, showing incomplete oxidation of graphite as reported in literature [40]. The XRD pattern of pure HAp presents several sharp and strong Bragg diffraction peaks (pattern c), suggesting high degree of crystallinity of the synthesized HAp powder by the wet-synthesis method. The diffraction peaks and the corresponding crystal planes, $2\theta=25.9°$ (002), $28.2°$ (210), $29.0°$ (210), $31.4°$ (211), $34.15°$ (202), $39.8°$ (310), $49.5°$ (213), and $53.3°$ (004) are well consistent with the results of PDF card number 09-0432 [41], proving the successful synthesis of HAp. It is interesting that when GO was utilized as a supporting platform to synthesize HAp, the sharp and intense diffraction peak at $2\theta=10.17°$ corresponding to the characteristic plane (002) of GO was totally disappeared, indicating that the oxygen-containing functional groups on GO has been removed likely due to the reduction process (pattern b). But the peak at $2\theta=23.5°$ is still present, showing that honeycomb-like carbon backbone of the two-dimension carbon material is remained. In addition, one can clearly observe that all the characteristic peaks ascribing to HAp are also visible in the XRD pattern of the composite, confirming that HAp has been successful grown on the rGO surface to form their composite.
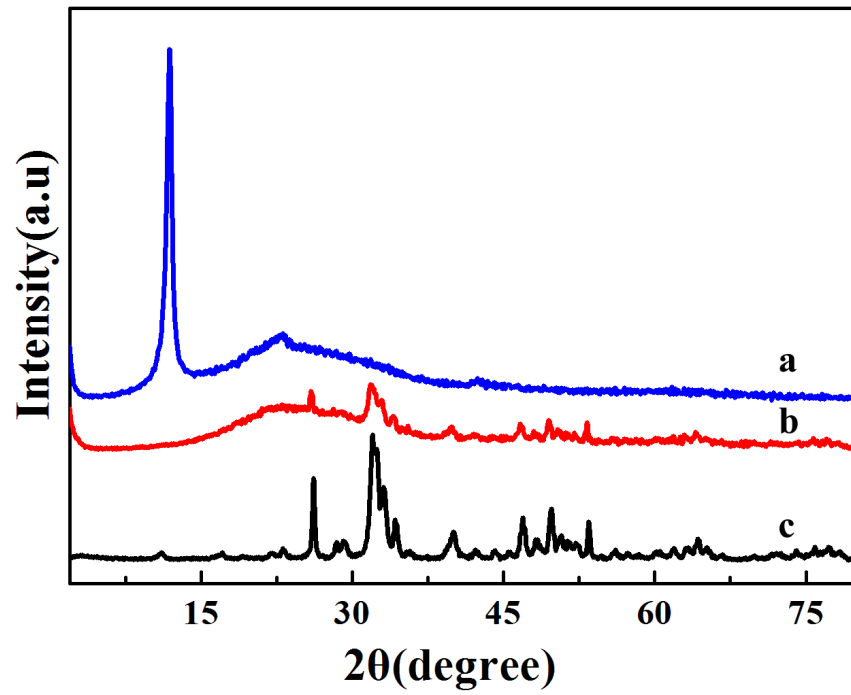
Fig. 4.1 XRD patterns of GO (a), HAp-rGO (b) and HAp (c).

To further testify that the direct reduction of GO was triggered by the synthesis of HAp without the assistance of any other reduction agent, the synthesized nanocomposite was further characterized by Raman analysis. As shown in Fig. 4.2, the pure HAp has not obvious peak on the measured Raman shift range (spectrum c). Both the pristine GO (spectrum a) and its composite with synthesized HAp (spectrum b) has two characteristic peaks at 1335 cm^{-1} (D band) and 1597 cm^{-1} (G band), respectively. The G band corresponding to an E_{2g} mode of graphite is usually related to the vibration of the sp^2-bonded carbon atoms in a 2D hexagonal lattice, while the D band is a sign of disorder of GO, originating from vacancies-associated defects. The intensity ratio of the two bands (I_D/I_G) is usually employed to judge the graphitization degree of carbonaceous materials and the defect density [42]. From Fig. 4.2, the ratio of I_D/I_G for pristine GO was determined to be 0.82 (spectrum a), suggesting relatively high structure defection of the synthesized GO. However for the composite, the ratio of I_D/I_G was increased to be 0.93 (spectrum b), demonstrating the decrease of the defect degree of GO. This change also confirms that GO has been transformed to the reduction form (rGO) during the synthesis of HAp. In addition, the 2D peak located at approximately 2668 cm^{-1} that sensitive to the layer number of graphene shows insignificant change in pristine GO and the composite, suggesting that the π-stacking of the reduced GO has not happened during the HAp growth-induced reduction process, which is likely due to the protection of the graphene surface from aggregation by the adsorbed HAp.
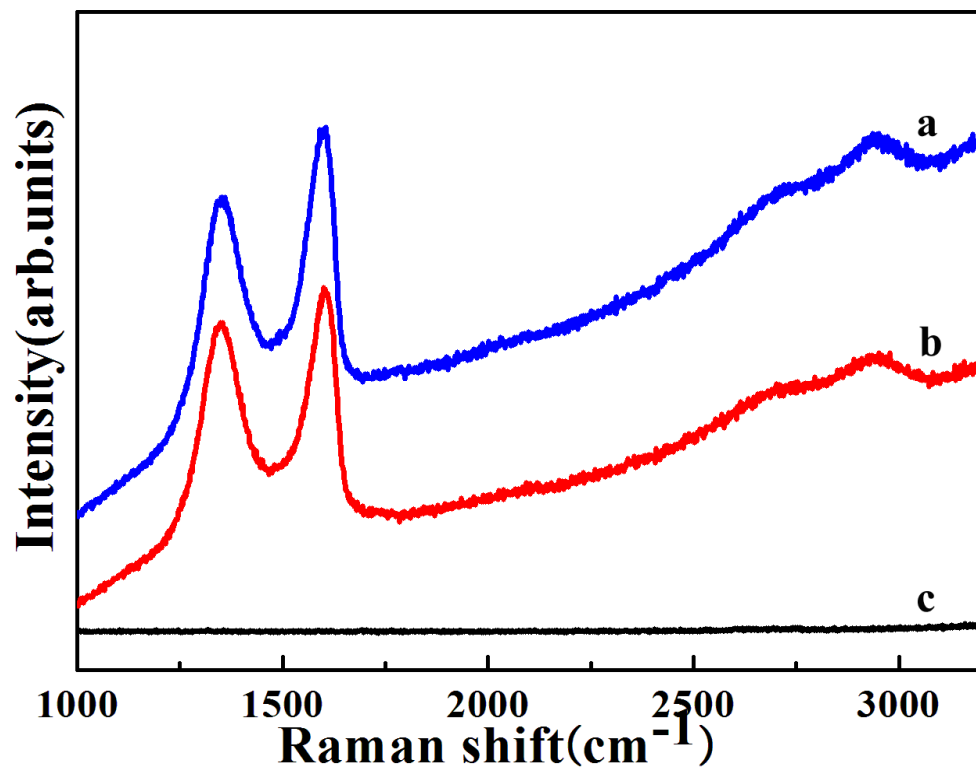
Fig. 4.2 Raman spectra of GO (a), HAp-rGO (b) and HAp (c).

The product was further examined by FTIR and the results are shown in Fig. 4.3. The broad adsorption band at approximately 3380 cm^{-1} for pristine GO is assigned to the hydroxyl group (-OH) stretching vibration (spectrum a). The bands at 1730 cm^{-1} and 1623 cm^{-1} are attributed to the stretching vibrations of the carboxyl group (-COOH) on the edge of the basal planes and the sp^2 hybridized C=C vibration stretching, respectively. The characteristic epoxy bond (C-O-C) in GO is clearly visible at 1055 cm^{-1}. For the pure HAp (spectrum c), the adsorption bands at 1093 cm^{-1}, 1044 cm^{-1} and 962 cm^{-1} are respectively assigned to the asymmetric and symmetric stretching vibration modes of PO$_4^{3-}$, whereas those at 602 cm^{-1} and 563 cm^{-1} are to the asymmetric bending vibration of PO$_4^{3-}$. Also a band at around 3370 cm^{-1} was visible, which is attributed to the OH$^-$ group of HAp. For the composite (spectrum b), it is found that the main characteristic peaks (1044 cm^{-1}, 1093 cm^{-1}, 602 cm^{-1}, 563 cm^{-1}) of HAp are still present, confirming that HAp has been formed on the composite material. But in comparison with GO, all the oxygen-containing groups from pristine GO are totally disappeared, except for the featured band at 1623 cm^{-1} arising from the C=C stretching vibration of the graphite layer backbone. The result testifies that GO has been reduced that triggered by the growth of HAp on its surface.
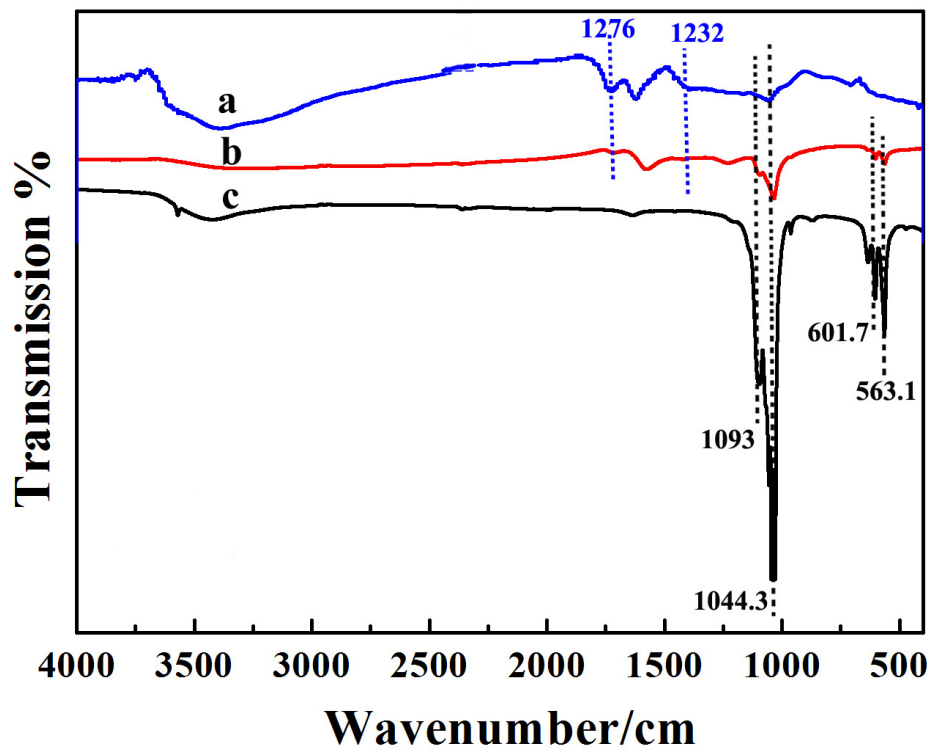
Fig. 4.3 FTIR spectra of GO (a), HAp-rGO (b) and HAp (c).

The morphology of the synthesized product was then recorded by TEM. Fig. 4.4A shows that the prepared GO presents its inherent thin film and wrinkle structure as reported in previous literature [43], showing that GO has been well prepared from graphite through the modified Hummer's method. The typical TEM image of pure HAp is displayed in Fig. 4.4B, from which one can see that the synthesized HAp particles present uniform rod-like shape with a length of *ca.* 100 nm and a width of *ca.* 20 nm. The TEM image of the HAp-rGO composite (Fig. 4.4C) indicates that some rod-like HAp particles (Yellow arrows) are well distributed on the sheet-like film of rGO material (Red arrows). This result clearly demonstrates that GO acts as an effective supporting platform for the growth of HAp nanorods to form their nanocomposite. The UV-vis absorption spectra as showed in Fig. 4.5 show that the pristine GO dispersion has a strong characteristic adsorption peak at 220 nm and a broad peak centered at 300 nm ascribing to the $\pi \rightarrow \pi^*$ transition of unoxidized aromatic C=C bonds and n $\rightarrow \pi^*$ transitions of C=O bonds [44], respectively. However, after *in-situ* synthesis of HAp on GO, it is found that the characteristic absorption peaks of GO disappeared absolutely, proving that the structure of GO has been changed. The electronic photographs of the pristine GO solution and the synthesized HAp-rGO dispersion as displayed in inset of Fig. 4.5, which further revealed that, after growth of HAp on the GO skeleton, the original tan solution of GO becomes black, which also indirectly testify that the GO has been reduced to the reduction form via the deoxygenation process.
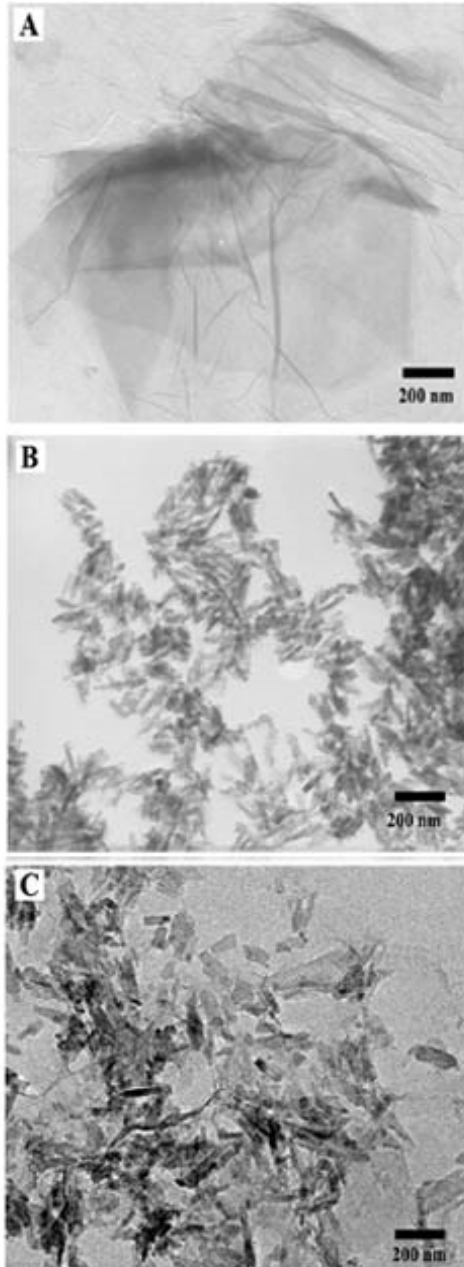
Fig. 4.4 TEM images of pure GO (A), HAp (B) and synthesized HAp-rGO (C).
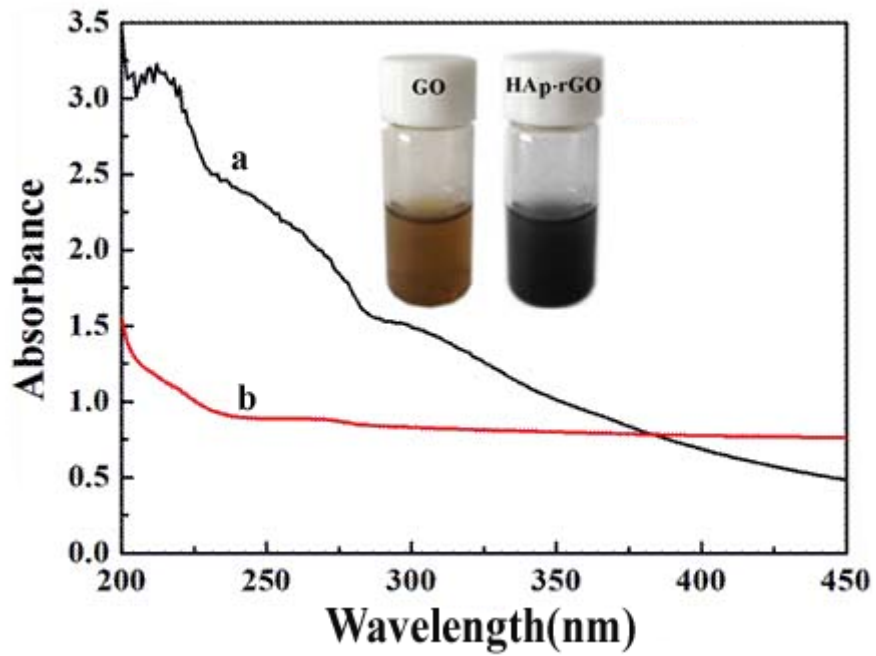
Fig. 4.5 UV-vis absorption spectra of GO (a) and HAp-rGO (b) dispersion. Inset is the electronic photos of aqueous dispersion of GO and HAp-rGO.

4.3.2 Electrochemical behavior of the HAp-rGO

To probe the effect of GO reduction on the electrochemical property of the material, the modified electrodes of HAp-rGO-CS/GCE, GO-CS/GCE and HAp-CS/GCE were fabricated, and their electrochemical behaviors in $[Fe(CN)_6]^{3-/4-}$ solution were characterized and compared by CV. Fig. 4.6 represents the CVs of (a) bare GCE, (b) HAp-rGO-CS/GCE, (c) GO-CS/GCE and (d) HAP-CS/GCE in 1 mM $[Fe(CN)_6]^{3-/4-}$ solution containing 0.1 M KCl at 0.1 mV s$^{-1}$. As shown, a pair of well-defined redox peaks ascribing to electron-transfer of Fe^{III}/Fe^{II} couple was observed at bare GCE (curve a). However, when GO-CS (curve c) and HAp-CS (curve d) modified electrodes were tested, the redox peaks of $[Fe(CN)_6]^{3-/4-}$ on these two electrodes both decrease significantly in relative to bare GCE, suggesting that materials of GO-CS and HAp-CS barrier the electron transfer of $[Fe(CN)_6]^{3-/4-}$ due to their non-conductive property and their electrostatic repulsion toward $[Fe(CN)_6]^{3-/4-}$. Interestingly, when the synthesized composite of HAp-rGO was used as the electrode modifier for electrochemical test, the redox peaks in the CV of $[Fe(CN)_6]^{3-/4-}$ enhance dramatically in comparison with single-component material (HAp or GO) modified electrode discussed above. What's more, the capacitance-determined background currents also increase greatly. These two changes clearly suggest that the synthesized HAp-rGO has better electronic conductivity and larger effective surface area to promote the electrochemical response of the electroactive probe, which also testifies that the reduced form of GO (rGO) has been formed during synthesis of HAp.

The modified electrodes of HAp-rGO-CS/GCE, GO-CS/GCE and HAp-CS/GCE were fabricated, and their electrochemical behaviors in $[Fe(CN)_6]^{3-/4-}$ solution were also characterized and compared by EIS. Fig. 4.7 shows the Nyquist plots (Z_{im} *vs.* Z_{re}) of bare GCE (curve a), HAp-rGO-CS/GCE (curve b), GO-CS/GCE (curve c), HAp-CS/GCE (curve d) in mixture of 1 mM $[Fe(CN)_6]^{3-/4-}$ and 0.1 M KCl. The corresponding electrical equivalent circuit is given as inset of the Fig. 4.7, in which the symbol of R_s represents the solution-diffusion resistance and R_{ct} is the charge-transfer resistance of counterion at the film-electrolyte interface. The diffusion resistance of

$[Fe(CN)_6]^{3-/4-}$ within the modified film and the double-layer capacitance in the equivalent circuit are symbolized by Warburg element (W) and Q_{dl} respectively. From the Figure, it can be obtained that the fitting results (solid lines) from the equivalent circuit model are in good agreement with the real experimental data (dotted curves), suggesting that the proposed equivalent circuit is reasonable. Through fitting the experimental data by the circuit, the values of all the elements are yielded and listed in Table 4.1. As seen, the R_s components corresponding to the solution-diffusion resistance keep stable in the range between 10.57 and 14.02 $\Omega\,cm^2$, which are reasonable since the measurements of the electrodes are under same conditions. In addition, the bare GCE shows relatively small R_{ct} value (5.20 $\Omega\,cm^2$), indicating the used bare GCE is capable of acting as a good basal electrode. However, when the bare GCE was modified with the material of GO-CS (curve c) or HAp-CS (curve d), the sharply increased R_{ct} values of 208.5 $\Omega\,cm^2$ and 350.3 $\Omega\,cm^2$ were generated, suggesting that the electron-transfer process of $[Fe(CN)_6]^{3-/4-}$ was blocked by GO and HAp due to their inferior electronic conductivity. Alternatively, when the HAp-rGO was cast on GCE, the R_{ct} value was dramatically decreased to 127.3 $\Omega\,cm^2$ (curve b), further proving that HAp-rGO nanocomposite provides excellent electron transfer pathways between basal electrode and the electrochemical probe because of the high electronic conductivity of rGO in the composite film. In addition to this, it is found that the HAp-rGO modified electrode has the largest Q_{dl} value among all the electrodes, which confirms that this electrode has the largest effective surface area to produce largest double-layer capacitance.
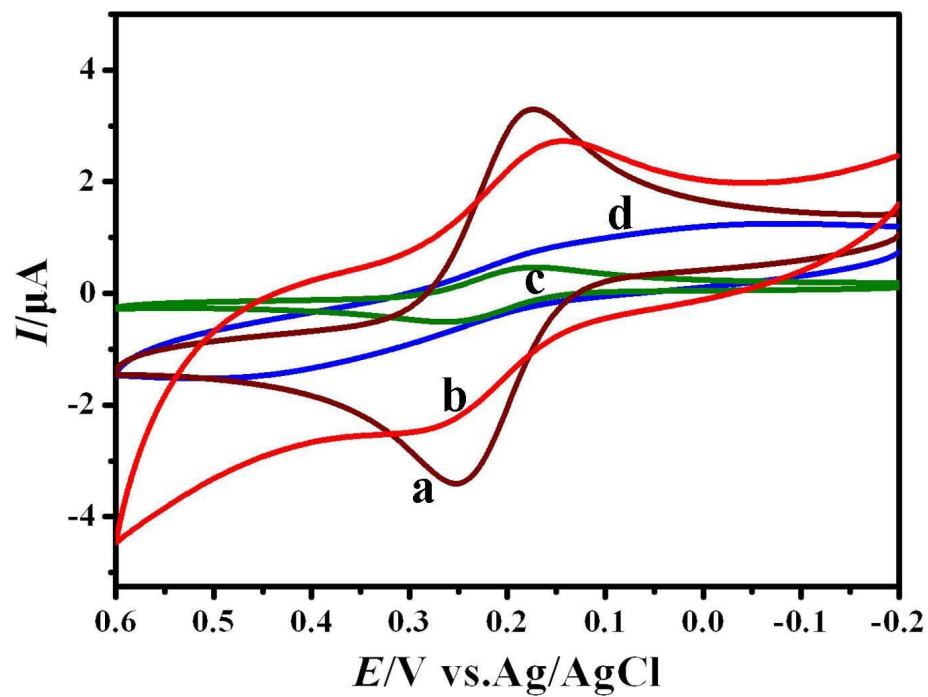
Fig. 4.6 CVs of (a) bare GCE, (b) HAp-rGO-CS/GCE, (c) GO-CS/GCE and (d) HAp-CS/GCE in 1 mM $(Fe(CN)_6)^{3-/4-}$ solution containing 0.1 M KCl.
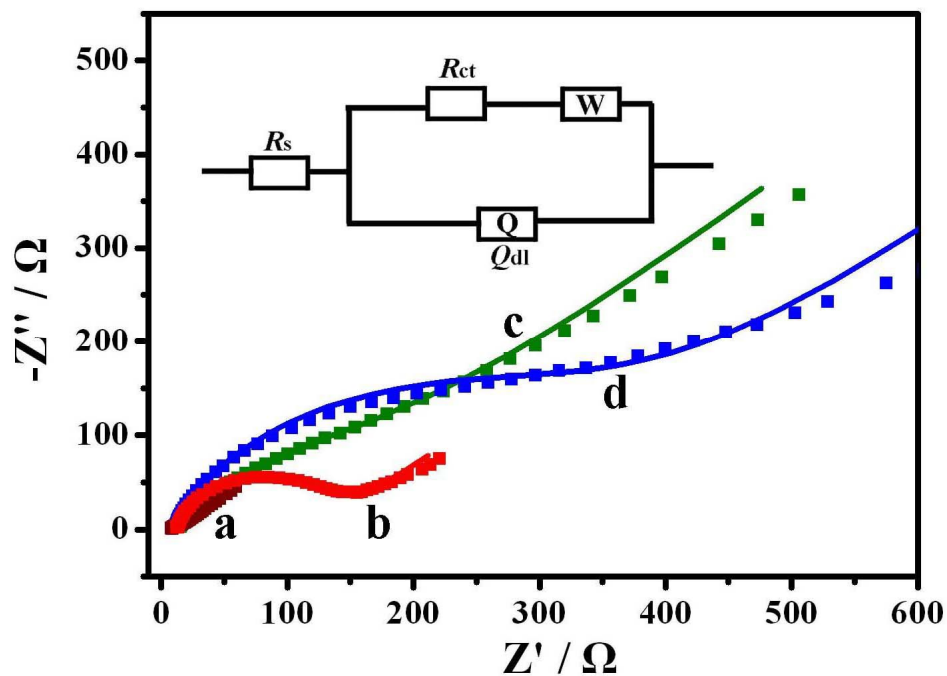
Fig. 4.7 Nyquist plots of (a) bare GCE, (b) HAp-rGO-CS/GCE, (c) GO-CS/GCE and (d) HAp-CS/GCE in 1 mM $(Fe(CN)_6)^{3-/4-}$ solution containing 0.1 M KCl. Inset shows the corresponding electrical equivalent circuit during electrochemical impendence spectra tests.

Table 4.1 Simulated Values of the Equivalent Circuit Elements for the Different Modified Electrodes

Electrode	R_s (Ω cm^2)	Q_{dl} (μF cm^2)	n	R_{ct} (Ω cm^2)	W (mΩ cm^2)
GCE	11.43	44.72	0.93	5.20	5.86
GO-CS/GCE	14.02	71.83	0.72	208.5	0.69
HAp-CS/GCE	10.57	28.11	0.80	350.3	0.90
HAp-rGO-CS/GCE	12.95	19.65	0.88	127.3	3.44

4.3.3 Electrocatalysis of HAp-rGO toward oxidation of hydrazine

Hydrazine and its derivatives are well known for their widespread industrial and pharmaceutical applications, such as corrosion inhibitors, plastic blowing agents, oxygen scavengers, rocket propellant, explosives, herbicides, photographic chemicals and catalysts [45, 46]. Despite their extensive applications, they are classified as group B2 human carcinogens by World Health Organization (WHO) and United States Environmental Protection Agency (USEPA) due to their high toxicity [47]. Hence the rapid and sensitive determination of hydrazine is incredibly important for both body safety and environmental pollution monitoring. Soundly, it is found that the obtained HAp-rGO nanocomposite shows obvious electrocatalysis toward the oxidation of hydrazine. Fig. 4.8A shows the CVs of GO-CS/GCE (a, a'), HAp-CS/GCE (b, b') and HAp-rGO-CS/GCE (c, c') in 25 mM PBS (pH 7.0) containing 0 (a, b, c) and 0.2 mM (a', b', c') hydrazine at a scan rate of 0.1 V s^{-1}. The corresponding currents at 0.8 V of different electrodes are depicted in Fig. 4.8B. As seen, when GO-CS/GCE and HAp-CS/GCE were applied for determination, only small current enhancements (4.54 µA for GO-CS/GCE, 6.36 µA for HAp-CS/GCE) were observed upon addition of 0.2 mM hydrazine, indicating that both GO-CS/GCE and HAp-CS/GCE had limited electrocatalysis toward hydrazine oxidation. In contrast, a dramatic increase of current (26.4 µA) was obtained for HAp-rGO-CS/GCE when 0.2 mM hydrazine was added, demonstrating its superior electrocatalytic activity and kinetics toward hydrazine oxidation compared with the other two samples modified GCE. The outstanding electrochemical response mechanism of hydrazine on HAp-rGO-CS/GCE can be explained by kinetic adsorption of hydrazine on the electrode surface and the following thermodynamic decomposition that catalyzed by sensing film as displayed below [48]:

$$N_2H_4(\text{solution}) + \text{HAP-rGO-CS} \xrightarrow{Adsorption} N_2H_4(\text{Surface})\text{-HAP-rGO-CS} \tag{1}$$

$$N_2H_4(\text{Surface})\text{-HAP-rGO-CS} + 4OH^- \xrightarrow{Electro\text{-}oxidation} N_2\uparrow + 4H_2O + 4e^- + \text{HAP-rGO-CS} \tag{2}$$
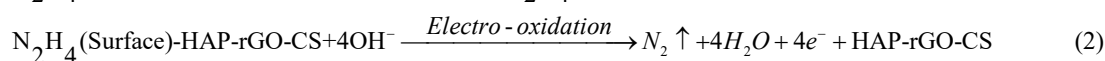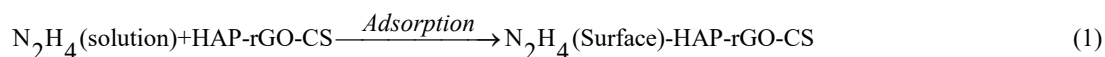
The different electrocatalytic activity of GO, HAp and HAp-rGO toward hydrazine was further investigated through the amperometric techniques. Fig. 4.9 shows the

typical amperometric curve of the three modified electrode in stirring 25 mM PBS (pH 7.0) at an applied potential of 0.55 V upon successive additions of hydrazine. It is clearly found that the addition of hydrazine produces insignificant increase of catalytic current at HAp-CS/GCE (curve a) and GO-CS/GCE (curve b), also showing their low electrocatalysis toward hydrazine oxidation. However, when hydrazine was successively injected into PBS and detected by HAp-rGO-CS/GCE, obvious ladder-shaped increases in current was generated (curve c), and the steady current can be obtained within 2 s upon each injection. These phenomenons definitely show that HAp-rGO has fast and significant electrocatalytic effect on the oxidation of hydrazine, reflecting its potential for the real-time monitoring of hydrazine.
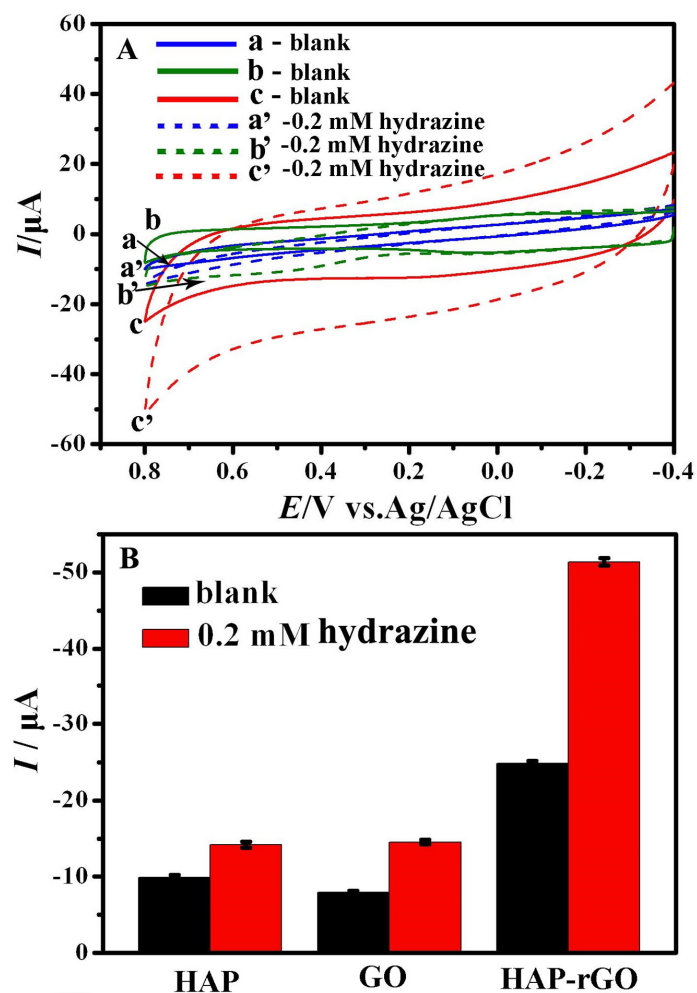
Fig. 4.8 (A) CVs and (B) the corresponding current values (at 0.8 V) of GO-CS/GCE (a', a,), HAp-CS/GCE (b', b,), HAp-rGO-CS/GCE (c', c,) in 25 mM PBS (pH 7.0) containing 0 (a, b, c) and 0.2 mM hydrazine (a', b', c') at scan rates of 0.1 V s^{-1}.
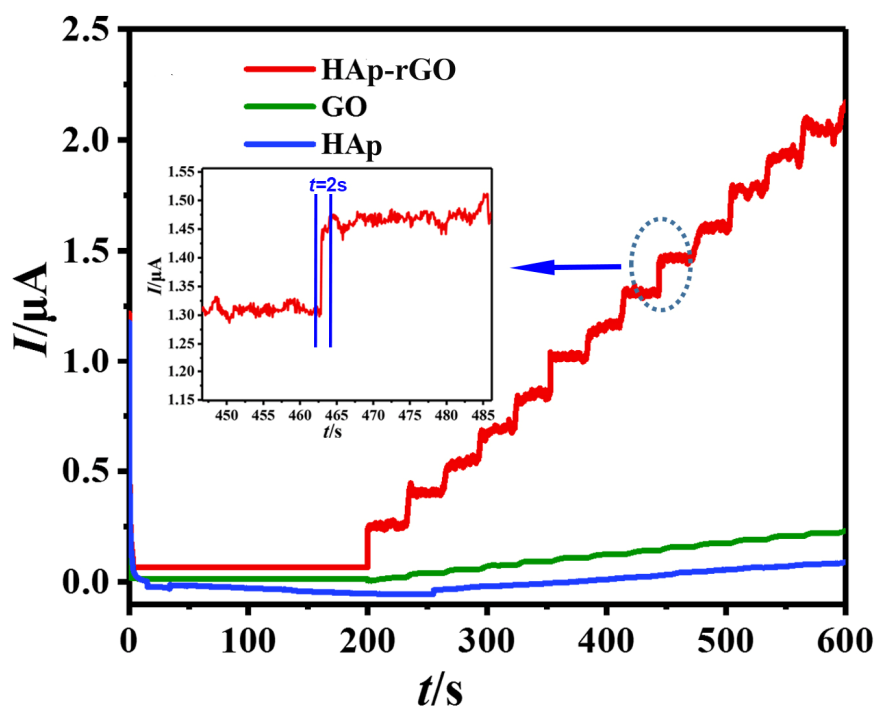
Fig. 4.9 Chronoamperometric curves of HAp-CS/GCE (a), GO-CS/GCE (b) and HAp-rGO-CS/GCE (c) in 25 mM PBS (pH 7.0) upon injection of hydrazine. Inset is the response time of a single injection of hydrazine.

The electrocatalytic parameters of the sensing interface towards hydrazine was further investigated by chronoamperometry. Fig. 4.10A shows the chronoamperometric response for the HAp-rGO-CS/GCE in the absence (curve a) and presence of various concentrations (from 0.10 to 0.80 mM) (curve b-e) of hydrazine at the applied potential of 0.55 V. As seen the steady currents enhance with the increase of added hydrazine concentrations. Then, the catalytic rate constant (K_{cat}) was estimated according to Cottrell equation [49]:

$$I_{cat}/I_L = (\pi K_{cat} C_0 t)^{1/2} \qquad (3)$$

Where I_{cat} and I_L are the current of HAp-rGO-CS/GCE in presence and absence of hydrazine, respectively, K_{cat} is the catalytic rate constant. Clearly, plotting the I_{cat}/I_L versus $t^{1/2}$ produces straight lines as displayed in Fig. 4.10B. From the slopes of I_{cat}/I_L-$t^{1/2}$, the average value of K_{cat} was calculated to be 7.70×10^3 M^{-1} s^{-1}, which is larger than the previously reported values of 5.1×10^3 M^{-1} s^{-1} on benzothiazole-iron oxide nanoparticles modified carbon paste electrode [50], 2.2×10^3 M^{-1} s^{-1} on cobalt pentacyanonitrosyl ferrate modified GCE [51] and 1.9×10^3 M^{-1} s^{-1} on ellagic acid-carbon nanotubes modified GCE [52], experimentally indicating that the HAp-rGO-CS has an excellent electrocatalytic activity for the oxidation of hydrazine. In addition, the diffusion coefficient (D) of hydrazine in the system was determined according to the following equation [49]:

$$I_{cat} = nFAD^{1/2}C_0\pi^{-1/2}t^{-1/2} \qquad (2)$$

Where A the electrode area, and the other symbols are the same with the aforementioned equations. The plot of I_{cat} versus the inverse square root of time elapsed ($t^{-1/2}$) is displayed in Fig. 4.10C. From the slope of the plot, the value of D was calculated to be 5.35×10^{-6} cm^{-1} s^{-1}, which is very close to the values in previous reports [53, 54].
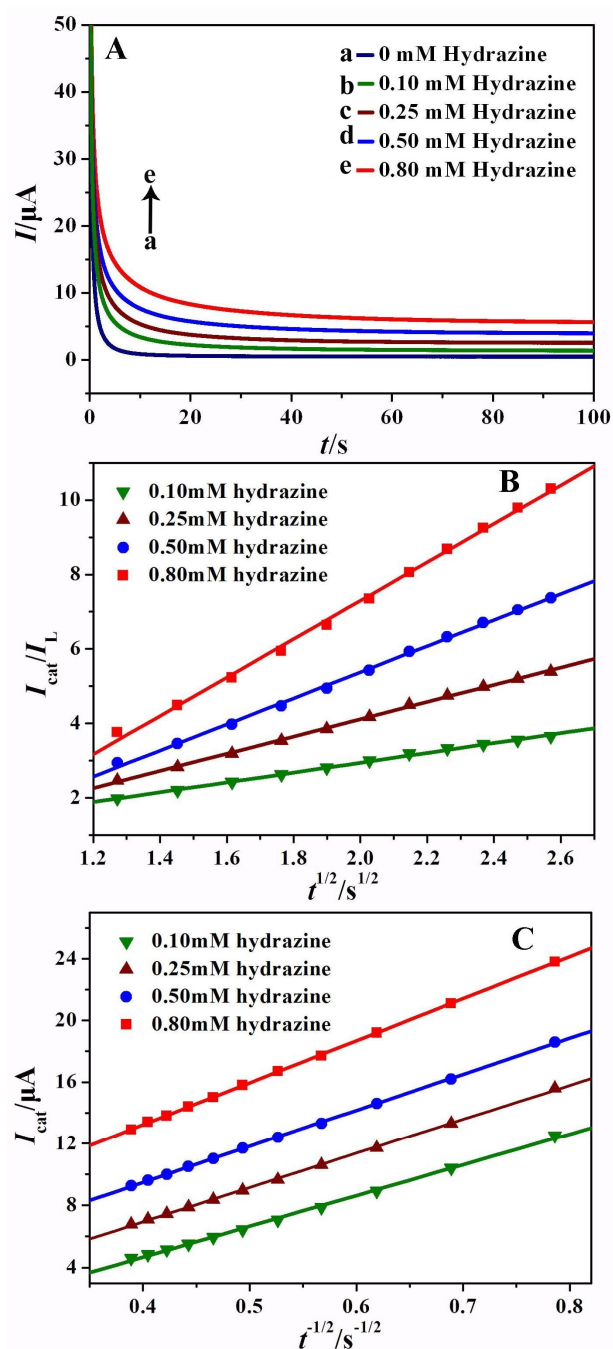
Fig. 4.10 (A) Chronoamperometric response of HAp/GO-CS/GCE in 25 mM PBS (pH 7.0) without (curve a) and with (curve b-e) of various concentration (from 0.10 to 0.80 mM) of hydrazine at the applied potential of 0.55 V. (B) The plot of I_{cat} vs. $t^{-1/2}$. (C) The plot of I_{cat}/I_L vs. $t^{1/2}$.

4.3.4 Quantitative analysis

Prior to the quantitative analysis of hydrazine by the developed electrode of HAp-rGO-CS/GCE, the applied potential (E_α) that has been reported to closely related to the sensitivity, stability and selectivity of sensors has been optimized. Fig. 4.11 shows the chronoamperometric curves of HAp-rGO-CS/GCE in PBS upon successive addition of hydrazine under the various applied potentials and the corresponding relationship of sensitivity versus applied potentials (Inset). The results show that when the applied potential was changed from 0.40 V to 0.55 V, the current response in the chronoamperometric curves and the sensitivity of sensor both increase accordingly, showing that the electrocatalysis of the sensor toward hydrazine enhanced with increase of the applied potential. Nonetheless, when the applied potential was further increased to 0.60 V, the stability of current response and the sensitivity of the analysis decrease slightly. This might be related to the interference of N_2 that produced from the oxidation of hydrazine. Therefore, 0.55 V was choose as the optimal applied potential in this work.

Under the optimal applied potential, the quantitative analysis performance of the constructed sensor to hydrazine was assessed by amperometry. Fig. 4.12A presents the typical amperometric curve at HAp-rGO-CS/GCE with consecutive injection of various concentrations of hydrazine into 25 mM PBS (pH 7.0) solution. The result shows that each injection of hydrazine can cause the increase of the catalytic current, even its concentration down to µM order. The corresponding calibration curve of catalytic current (I) versus hydrazine concentration (C) is depicted in Fig. 4.12B. It is observed that two calibration curves are obtained in hydrazine concentrations ranging from 2.5 µM to 0.26 mM and from 0.26 mM to 1.16 mM, respectively. The corresponding linear regression equations are as follows:

$I/\mu A = 132.27 (C/mM) - 0.0687$ (r=0.994);

$I/\mu A = 50.79(C/mM) + 23.81$ (r=0.995) .

The limit of detection (LOD) was then calculated to be 0.43 µM, based on three times of the standard deviation for the average measurements of blank samples

(LOD=3×RSD/Slope). In addition, from the regression equations, we can find that the sensor presents higher sensitivity (4.21 $\mu A\ \mu M^{-1}\ cm^{-2}$) for hydrazine in the lower concentration region (2.5 μM~0.26 mM) than that (1.61 $\mu A\ \mu M^{-1}\ cm^{-2}$) at the higher region (0.26 mM~1.16 mM). This phenomenon can be ascribed to the different oxidation kinetic process of hydrazine at different concentrations [55]. In the low concentration region of hydrazine, the electrocatalytic oxidation process is dominated by the adsorption of hydrazine on the sensing interface, leading to a high sensitivity; whereas, with increase of hydrazine in solution, the electrocatalytic activation of hydrazine on the electrode surface becomes rate-determining step, therefore leading to the decrease of the analytical sensitivity.
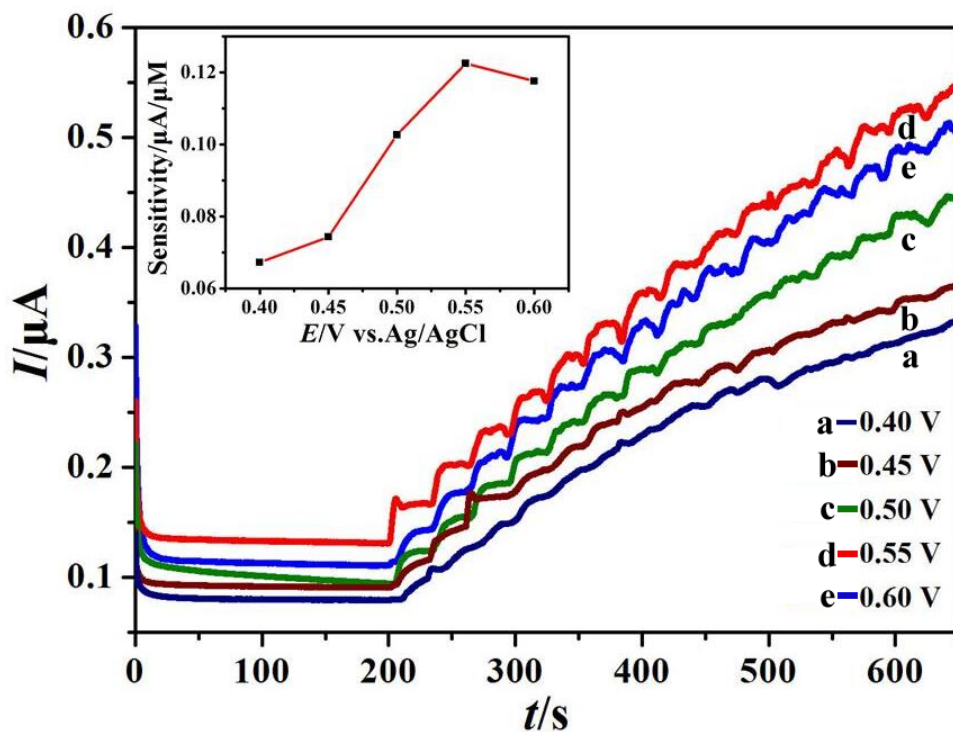
Fig. 4.11 Amperometric current response of HAp/GO-CS/GCE at different potentials in 0.1 M NaOH with successive addition of 0.2 mM H_2O_2. The insert reveals the sensitivity of different potentials.
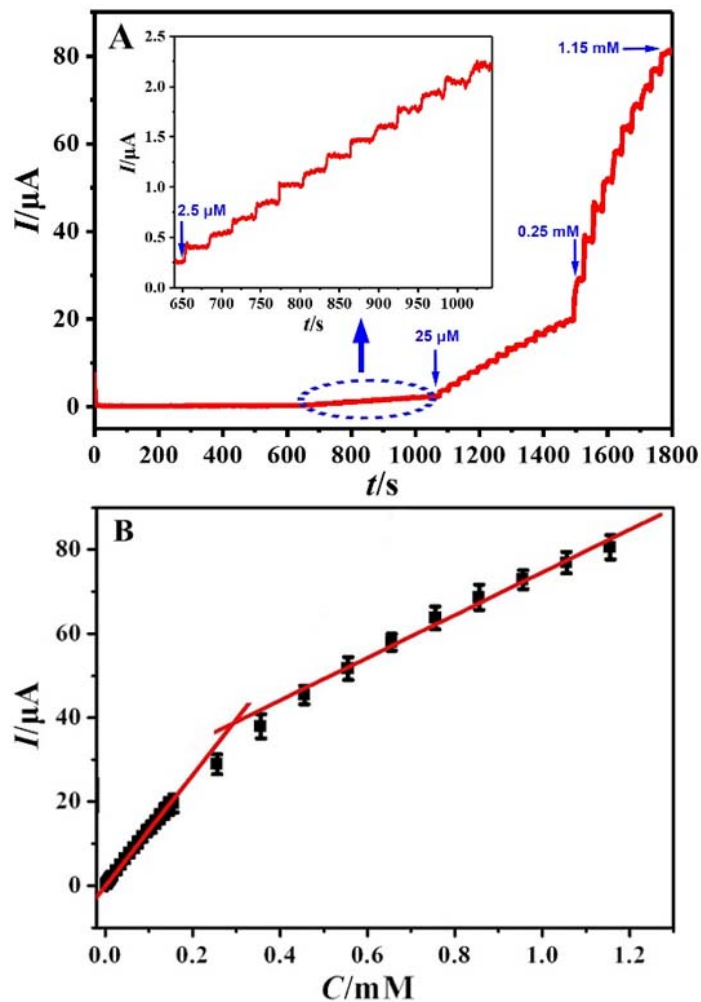
Fig. 4.12 (A) Chronoamperometric responses of HAp-rGO-CS/GCE 25 mM PBS (pH 7.0) upon successive additions of hydrazine at the applied potential of 0.55 V. (B) Calibration plots of catalytic current (*I*) with the concentration of hydrazine (*C*).

The analytical performances of the developed sensor to hydrazine, such as linear range, LOD and sensitivity were also compared with some other nanocomposite-based sensors, and the results are listed in Table 4.2. It can be found that our sensor exhibits comparable and even better performance in the indexes of linear range, LOD and sensitivity for the determination of hydrazine relative to the materials of multi-walled carbon nanotubes (MWCNTs)/chlorogenic [56], GO/chitosan/Pt [57] and curcumin/MWCNTs [58], showing that the synthesized HAp-rGO is more suitable to be used as a highly sensitive platform for hydrazine detection. In addition, although the achieved LOD is little higher than that obtained on the hydrazine sensors based on nitrogen-doped graphene-polyvinylpyrrolidone (NG-PVP)/gold nanoparticles (AuNPs) [59], Au/ZnO [60], AuNPs-HAp [61], and MnO_2–vulcan carbon@Ag [62], the HAp-rGO used in this work is more environmental-friendly, dispensable with precious metal and easier for preparation, making the sensor developed in this work more promising for widespread practical application. According to the structural and morphologic characteristic of the sensing material of HAp-rGO, we speculated that the outstanding sensing performance mentioned above should be attributed to the following reasons: (1) the rich active sites (OH^-, PO_4^{3-}) of HAp allow sufficient and strong adsorption and contact of hydrazine at the electrolyte/electrode sensing interface; (2) The loose and porous structure of HAp-rGO nancomposite facilitates the transport of hydrazine molecules within sensing interface; (3) the excellent conductivity of rGO promotes fast electron transfer and high catalytic current for the electro-oxidation of hydrazine.

Table 4.2 Comparisons of analytical performance of hydrazine at HAp-rGO-CS/GCE with some other electrochesensors.

Sensing film	Technology	Sensitivity($\mu A\,\mu M^{-1}\,cm^{-2}$)	Linear range (μM)	LOD (μM)	Refs.
MWCNTs/Chlo	I-t	0.0041	2.5–5000	8	[63]
GO/CTS/Pt	I-t	0.1046	20–10000	3.6	[64]
CCM/MWCNTs	I-t	0.0229 $\mu A\,\mu M^{-1}$	2–44	1.4	[65]
AuNPs	I-t	1.117 $\mu A\,\mu M^{-1}$	500–4000	42	[66]
NG-PVP/AuNPs	SWV	1.370	2–300	0.07	[67]
Au/ZnO	I-t	0.873	0.2–14.2	0.242	[68]
AuNPs/TiO$_2$	CV	N. A.	2.5–500	0.5	[69]
AuNPs-HAp	I-t	0.5	0.5-1429	0.017	[70]
MnO$_2$–VC@Ag	CV	0.33	0.1–350	0.1	[71]
HAp-rGO-CS/GCE	I-t	4.21; 1.61	2.5 -260; 260-1160	0.43	This work

Note: MWCNTs=muti-walled carbon nanotubes; CTS=chitosan; Chlo=chlorogenic; CCM=curcumin; NG-PVP=nitrogen-doped graphene-polyvinylpyrrolidone; SWV=squarewave voltammetry; VC=vulcan carbon.

4.3.5 Anti-interference, stability, and reproducibility

The an-interference capacity is an important aspect for practical application of a sensor, which can be assessed by studying the sensor response variation in the presence of some possibly-coexisted substances. Fig. 4.13 shows the chronoamperometric response of HAp-rGO-CS/GCE in PBS upon injection of hydrazine and other interfering species. As seen, when 0.01 mM and 0.02 mM hydrazine were successively injected into the buffer solution in the beginning stage, obvious increases in current responses are observed in the chronoamperometric curve. Then, when the control substances of H_2O_2, glucose (Glu), glutathione (GSH), dopamine (DA), urea, ethanol, methanol, ascorbic acid (AA), acetic acid (AcA), formic acid (FA), citric acid (CA), and uric acid (UA) with concentration of 0.01 mM were respectively injected, almost these is not any variation, except a slight increase for DA. But the increase amplitude of current response for DA is still negligible in comparison with the case of hydrazine. Moreover, when hydrazine was further injected into the solution containing above added substances, the catalytic current increases again, and which confirmed that the HAp-rGO-based electrochemical sensor has good selectivity and anti-interference ability for the detection of hydrazine.

The stability of HAp-rGO-CS/GCE was examined by monitoring the electrocatalytic current of the prepared sensor to hydrazine after storage at 4 °C for different periods. It is found that the sensor has not apparent catalytic current change for hydrazine oxidation in the first 5 days, and shows only 8% attenuation in current after 30 days storage (inset of Fig. 4.14), demonstrating that the developed sensor has outstanding stability after long-term storage. The test stability of the sensor was also investigated by continue monitoring the steady-state current response over a period of 5000 s in hydrazine solution. The result shows that, after 5000 s test, the current remains 98.1% of the initial value (Fig. 4.14), which further reveals that the sensor has high stability for continues test in hydrazine sample. Reproducibility assays show that when five HAp-rGO-CS modified electrodes were fabricated and applied for detection of hydrazine, good reproductivity with the relative standard deviation (RSD) of 5.2% was

achieved. Also, when one electrode was utilized for determination of hydrazine for five times, the RSD value is determined to be 4.1%, demonstrating good repeatability of developed sensor.
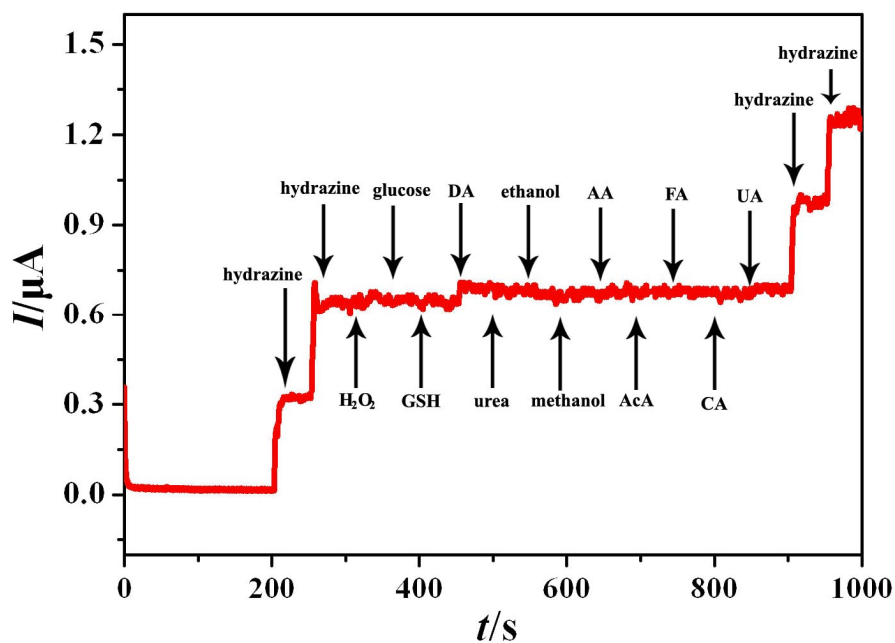
Fig. 4.13 Chronoamperometric responses of the HAp-rGO-CS/GCE on the successive addition of 0.01 mM hydrazine (twice), 0.01 mM H_2O_2, 0.01 mM glucose, 0.01 mM glutathione (GSH), 0.01 mM dopamine (DA), 0.01 mM urea, 0.01 mM ethanol, 0.01 mM methanol, 0.01 mM ascorbic acid (AA), 0.01 mM acetic acid (AcA), 0.01 mM formic acid, 0.01 mM citric acid (CA), 0.01 mM uric acid (UA) and 0.01 mM hydrazine (twice) into PBS (7.0) at 0.55 V.
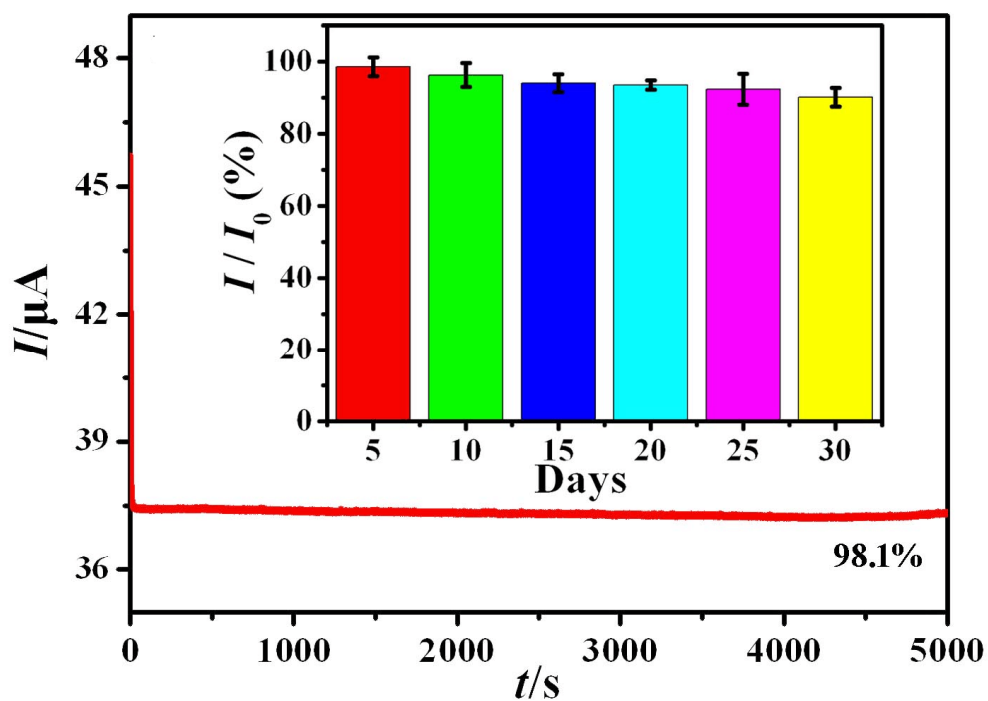
Fig. 4.14 Test stability of HAp-rGO-CS/GCE in hydrazine solution for 5000 s. Inset is the current retention ratio (I/I_0) for hydrazine detection after storage of the sensor for different period.

4.3.6 Analysis of hydrazine in industrial wastewater samples

In order to assess the feasibility of the developed sensor for the determination of hydrazine in real sample, the industrial wastewater after filtration with 0.2 μm film was adopted as model of real sample for analysis. Fig. 4.15 shows the typical chronoamperometric response of HAp-rGO-CS/GCE in PBS (7.0) upon successive injection with appropriate amount of filtrated industrial wastewater and hydrazine standard solution with interval of 100 s. From the result, one can see that the addition of industrial wastewater induce slight increase of the steady-state current, suggesting that the small amount of hydrazine is present in the sample. After the hydrazine standard solution was continuously added, the current response increases accordingly. The recoveries ratios were calculated to be 97.0-100% with RSDs in the range of 1.8-5.2% (Table 4.3), suggesting that the sensor is reliable for the determination of hydrazine in real water sample. In addition, according to the standard addition plot as depicted in inset of Fig. 4.15, the content of hydrazine in the wastewater was estimated to be 1.3 μM, showing that the wastewater contains trace hydrazine.
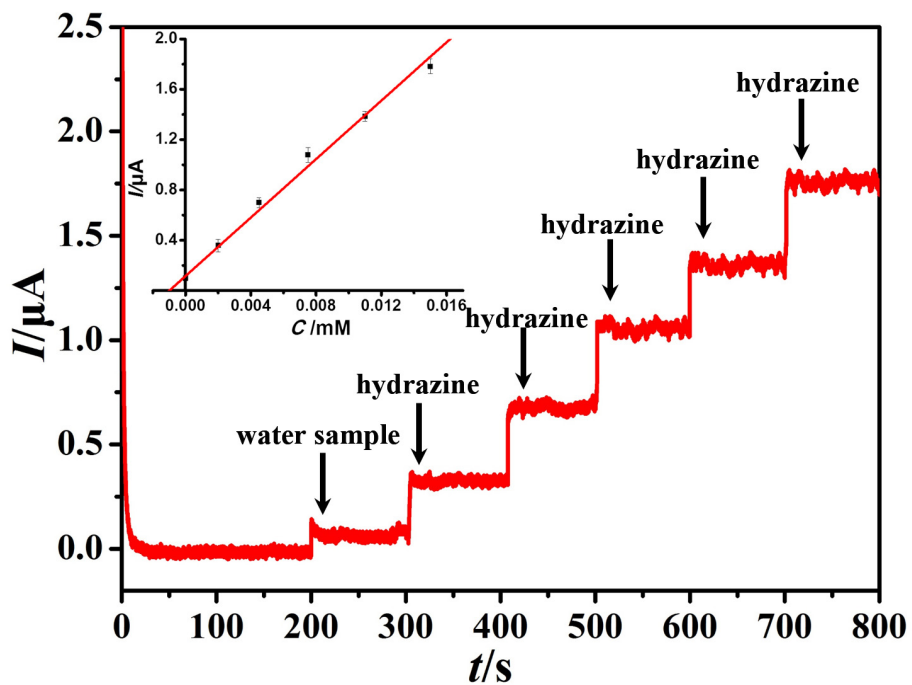
Fig. 4.15 Chronoamperometric curve of HAp-rGO-CS/GCE in 25 mM PBS (pH 7.0) upon injection with filtrated industrial wastewater and hydrazine standard solution. Inset shows the corresponding standard addition curve for determination of hydrazine in real sample.

Table 4.3 Recovery results of hydrazine standard solution injected into the industrial wastewater

Added (μM)	Found (μM)	Recovery (%)	RSD (%)
0	1.3	-	3.4
2.0	1.91	97.0	1.8
4.5	4.50	100	3.3
7.5	7.45	99.3	2.1
10.0	9.72	97.3	5.2
12.5	12.7	97.7	2.7

4.4 Conclusions

In this chapter, we unexpectedly found that the *in-situ* synthesis of HAp on GO surface can trigger the reduction of GO. The process can be completed under a moderate temperature (85 °C) situation, without the assistance of any and extra reducing agent. Electrochemical assays further showed that the formed HAp-rGO nanocomposite exhibited an outstanding performance for electrocatalytic oxidation of hydrazine. Satisfactory results were achieved when the sensor was utilized for hydrazine detection in real sample of industrial wastewater. This study opens a new avenue for the synthesis of HAp-rGO composites and their electrochemical sensing application.

4.5 References

[1] R. Socrates, N. Sakthivel, A. Rajaram, U. Ramamoorthy and S. N. Kalkura, *Mater. Lett.*, **161**, 759 (2015).

[2] H. L. Zhai, Z. S. Zhang, Y. L. Li, X. R. Xu and R. K. Tang, *ACS Appl. Mater. Interface*, **8**, 29997 (2016).

[3] H. Funao, S. Nagai, A. Sasaki, T. Hoshikawa, T. Tsuji, Y. Okada, S. Koyasu, Y. Toyama, M. Nakamura, M. Aizawa, M. Matsumoto and K. Ishii, *Sci. Rep.,* **6**, 23238 (2016).

[4] F. Gao, N. N. Gao, A. Nishitani and H. Tanaka, *J. Electroanal. Chem.,* **775**, 212 (2016).

[5] F. Gao, X. Q. Chen, H. Tanaka, A. Nishitani and Q. X. Wang, *Adv. Powder Technol.*, **27**, 921 (2016).

[6] A. Safavi, A. Abbaspour, M. Sorouri and A. Mohammadi, *ChemElectroChem,* **3**, 558 (2016).

[7] P. Kanchana, S. Radhakrishnan, M. Navaneethan, M. Arivanandhan, Y. Hayakawa and C. Sekar, *J. Nanosci. Nanotechnol.,* **15**, 1 (2015).

[8] K. Kandori, S. Tsuyama, H. Tanaka and T. Ishikawa, *Colloid Surface B,* **58**, 98 (2007).

[9] G. V. Dubacheva, C. K. Liang and D. M. *Coordin, Chem. Rev.,* **256**, 2628 (2012).

[10] D. Jariwala, V. K. Sangwan, L. J. Lauhon, T. J. Marks and M. C. Hersam, *Chem. Soc. Rev.,* **42**, 2824 (2013).

[11] B. C. Brodie, *Ann. Chim. Phys.,* **59**, 466 (1860).

[12] K. S. Novoselov, A. K. Geim, S. V. Morozov, D. Jiang, Y. Zhang, S. V. Dubonos, I. V. Grigorieva and A. A. Firsov, *Science,* **306**, 666 (2004).

[13] Y. V. Stebunov, O. A. Aftenieva, A. V. Arsenin and V. S. Volkov, *ACS Appl. Mater. Interfaces,* **7**, 21727 (2015).

[14] Y. Liu, Y. Li, J. Y. Liu, C. H. Deng and X. M. Zhang, *J. Am. Soc. Mass. Spectr.,* **22**, 2188 (2011).

[15] F. Nasrollahi, J. Varshosaz, A. A. Khodadadi, S. Lim and A. J. Najafabadi, *ACS*

Appl. Mater. Interface, **8**, 13282 (2016).

[16] F. Li, X. Jiang, J. J. Zhao and S. B. Zhang, *Nano Energy*, **16**, 488 (2015).

[17] P. Kalluru, R. Vankayala, C. S. Chiang and K. C. Hwang, *Biomaterials,* **95**, 1 (2016).

[18] F. Gao, X. L. Cai, H. Tanaka, Q. H. Zhu, F. Gao and Q. X. Wang, *J. Electrochem. Soc.,* **162**, B291 (2015).

[19] B. Gulbakan, E. Yasun, M. Shukoor, Z. Zhu, M. You, X. Tan, H. Sanchez, D. H. Powell, H. Dai and W. Tan, *J. Am. Chem. Soc.,* **132**, 17408 (2010).

[20] Y. Liu, D. S. Yu, C. Zeng, Z. C. Miao amd L. M. Da, *Langmuir,* **26**, 6158 (2010).

[21] P. Olejnik, A. Świetlikowska, M. Gniadek and B. Pałys, *J. Phys. Chem. C.* **118,** 29731 (2014).

[22] X. Wang, Q. X. Wang, Q. H. Wang, F. Gao, F. Gao, Y. Z. Yang and H. X. Guo, *ACS Appl. Mater. Interfaces,* **6**, 11573 (2014).

[23] W. F. Chen, L. F. Yan, P. R. Bangal, *Carbon*, **48**, 1146 (2010).

[24] G. Williams, B. Seger and P. V. Kamat. *ACS Nano,* **2**, 1487 (2008).

[25] D. H. Du, P. C. Li and J. Y. Ouyang, *ACS Appl. Mater. Interfaces,* **7**, 26952 (2015).

[26] W. F. Chen, L. F. Yan and P. R. Bangal, *J. Phys. Chem. C* **114**, 19885 (2010).

[27] J. Gao, F. Liu, Y. L. Liu, N. Ma, Z. Q. Wang and X. Zhang, *Chem. Mater.,* **22**, 2213 (2010).

[28] G. X. Wang, J. Yang, J. Park, X. L. Gou, B. Wang, H. Liu and J. Yao, *J. Phys. Chem. C* **112**, 8192 (2008).

[29] A. Ambrosi, C. K. Chua, A. Bonanni and M. Pumera, *Chem. Mater.,* **24**, 2292 (2012).

[30] J. D. Qiu, G. C. Wang, R. P. Liang, X. H. Xia and H. W. Yu, *J. Phys. Chem. C* **115**, 15639 (2011).

[31] V. Dua, S. P. Surwade, S. Ammu, S. R. Agnihotra, S. Jain, K. E. Roberts, S. Park, R. S. Ruoff and R. S. S. K. Manohar, *Angew. Chem. Int. Ed.,* **49**, 2154 (2010).

[32] D. R. Dreyer, S. J. Park, C. W. Bielawski and R. S. Ruoff, *Chem. Soc. Rev.,* **39**, 228 (2010).

[33] Q. W. Chen, L. Y. Zhang and G. Chen, *Anal. Chem.,* **84**, 171 (2012).

[34] D. Li, J. S. Zhou, X. H. Chen and H. H. Song, *ACS Appl. Mater. Interfaces,* **8**, 30899 (2016).

[35] H. Kim, A. A. Abdala and C. W. Macosko, *Macromolecules,* **43**, 6515 (2010).

[36] X. Zhang, F. Gao, X. L. Cai, M. X. Zheng, F. Gao, S. L. Jiang and Q. X. Wang, *Mater. Sci. Eng., C,* **33**, 3851 (2013).

[37] D. Joseph, S. Seo, D. R. Williams and K. E. Geckeler, *ACS Appl. Mater. Interfaces,* **6**, 3347 (2014).

[38] H. Y. Mao, Y. H. Lu, J. D. Lin, S. Zhong, A. T. S. Wee and W. Chen, *Prog. Surf. Sci.,* **88**, 132 (2013).

[39] F. Gao, X. L. Cai, X. Wang, C. Gao, S. L. Liu, F. Gao and Q. X. Wang, *Sens. Actuators B: Chem.,* **186**, 380 (2013).

[40] H. Y. Liu, P. X. Xi, G. Q. Xie, Y. J. Shi, F. P. Hou, L. Huang, F. J. Chen, Z. Z. Zeng, C. W. Shao and J. Wang, *J. Phys. Chem. C,* **116**, 3334 (2012).

[41] G. Ciobanu, S. Ilisei and C. Luca, *Mater. Sci. Eng. C,* **35**, 36 (2014).

[42] W. F. Zhao, M. Fang, F. R. Wu, H. Wu, L. W. Wang and G. H. Chen, *J. Mater. Chem.,* **20**, 5817 (2010).

[43] Y. Liu, J. Huang and H. Li, *J. Mater. Chem. B,* **1**, 1826 (2013).

[44] D. Li, M. B. Muller, S. Gilje, R. B. Kaner and G. G. Wallace, *Nat. Nanotechnol.,* **3**, 101 (2008).

[45] A. Serov, C. Kwak, *Appl. Catal. B: Environ.,* **98**, 1 (2010).

[46] J. E. Troyan, *Ind. Eng. Chem.,* **45**, 2608 (1953).

[47] M. D. Bethesda, US Department of Health and Human Services (1993)

[48] A. Umar, S. K. Kansal and S. K. Mehta, *Sens. Actuators B: Chem.,* **188**, 372 (2013).

[49] A. J. Bard, L. R. Faulkner, Wiley, New York, 28 (2001).

[50] A. Benvidi, S. Jahanbani, B. F. Mirjalili and R. Zare, *Chin. J. Catal.,* **37**, 549 (2016).

[51] M. H. Pournaghi–Azar, R. Sabzi, *J. Electroanal. Chem.,* **543**, 115 (2003).

[52] A. S. Kumar, R. Shanmugam, N. Vishnu, K. C. Pillai and S. Kamaraj, *J.*

Electroanal. Chem., **782**, 215 (2016).

[53] L. Zheng, J. F. Song, *Sens. Actuators B: Chem.,* **135**, 650 (2009).

[54] S. Zhao, L. L. Wang, T. T. Wang, Q. H. Han and S. K. Xu, *Appl. Surf. Sci.,* **369**, 36 (2016).

[55] H. Y. Zhu, A. Sigdel, S. Zhang, D. Su, Z. Xi, Q. Li and S. H. Sun, *Angew. Chem.,* **126**, 12716 (2014).

[56] A. Salimi, L. Miranzadeh and R. Hallaj, *Talanta,* **75**, 147 (2008).

[57] D. J. Rao, Q. L. Sheng and J. B. Zheng, *Sens. Actuators B: Chem.,* **236**, 192 (2016).

[58] L. Zheng, J. F. Song, *Sens. Actuators B: Chem.,* **135**, 650 (2009).

[59] C. Saengsookwaow, R. Rangkupan, O. Chailapakul and N. Rodthongkum, *Sens. Actuators B: Chem.,* **227**, 524 (2016).

[60] A. A. Ismail, F. A. Harraz, M. Faisal, A. M. E. Toni, A. A. Hajry and M. S. A. Assiri, *Mater. Design.,* **109**, 530 (2016).

[61] G. Bharath, A. Naldoni, K. H. Ramsait, A. A. Wahab, R. Madhu, E. Alsharaeh and N. Ponpandian, *J. Mater. Chem. A*, **4**, 6385 (2016).

[62] J. Babu, A. Zahoor, K. S. Nahm, M. A. Aziz, P. Vengadesh and G. G. Kumar, *New J. Chem.,* **40**, 7711 (2016).

[63] A. Salimi, L. Miranzadeh and R. Hallaj, *Talanta*. **75**, 147 (2008).

[64] D. J. Rao, Q. L. Sheng and J. B. Zheng, *Sens. Actuators B. Chem.,* **236**, 192 (2016).

[65] L. Zheng, J. F. Song, *Sens. Actuators B. Chem.,* **135**, 650 (2009).

[66] Q. F. Yi, W. Q. Yu, *J. Electroanal. Chem.,* **633**, 159 (2009).

[67] C. Saengsookwaow, R. Rangkupan, O. Chailapakul and N. Rodthongkum, *Sens. Actuators, B*, **227**, 524 (2016).

[68] A. A. Ismail, F. A. Harraz, M. Faisal, A. M. E. Toni, A. A. Hajry and M. S. A. Assiri, *Materials. Design.*, **109**, 530 (2016).

[69] G. F. Wang, C. H. Zhang, X. P. He, Z. J. Li, X. J. Zhang, L. Wang and B. Fang, *Electrochimica Acta.*, **55**, 7204 (2010).

[70] G. Bharath, A. Naldoni, K. H. Ramsait, A. A. Wahab, R. Madhu, E. Alsharaeh and

N. Ponpandian, *J. Mater. Chem. A*, **4**, 6385 (2016).

[71] J. Babu, A. Zahoor, K. S. Nahm, M. A. Aziz, P. Vengadesh and G. G. Kumar, *New J. Chem.*, **40**, 7711 (2016).

Chapter 5

General Conclusions and Scope

Chapter 5.1

General Conclusions

Chapter 2: Rod-like Hydroxyapatite and Nafion Nanocomposite as an Electrochemical Matrix for Simultaneous and Sensitive Detection of Hg^{2+}, Cu^{2+}, Pb^{2+} and Cd^{2+}

The rod-like HAp was synthesized by a facile wet method, and the morphology and structure of the obtained HAp were characterized. Then HAp-Nafion composite was prepared and used for the fabrication of modified electrode for detecting of Hg^{2+}, Cu^{2+}, Pb^{2+} and Cd^{2+} by differential pulse anodic stripping voltammetry. The results show that the four heavy metal ions present independent and strong stripping peaks on the HAp-Nafion modified electrode, suggesting that the obtained electrode is capable of being used for the simultaneous and sensitive detection of the four ions. It can be ascribed to the large specific surface area, rich active sites, and strong adsorption property of the composite. Based on a signal-to-noise ratio equal to 3 (S/N=3), the detection limits of Hg^{2+}, Cu^{2+}, Pb^{2+}, and Cd^{2+} were estimated to be 0.03 μM, 0.021 μM, 0.049 μM and 0.035 μM, respectively. Moreover, when the tap water was used as the model for the analysis, high recoveries for the four ions are obtained, demonstrating that the HAp-Nafion modified electrode is promising for monitoring of heavy metal ions in real samples.

Chapter 3: Alkaline Phosphatase Mediated Synthesis of Carbon Nanotube-Hydroxyapatite Nanocomposite and its Application for Electrochemical Determination of Luteolin

The nanocomposite of HAp-CNT was synthesized by an alkaline phosphatase assisted hydrolysis reaction. Then the GCE interface anchored with a nanocomposite of HAp-CNT-CS was developed for examining the electrochemical behaviors of luteolin. Electrochemical characterization experiments showed that

HAp-CNT-CS/GCE could greatly enhance the electrochemical signal of luteolin as compared to bare GCE and other modified electrodes, which could be ascribed to the synergistic amplification effects of HAp-CNT-CS nanocomposite film. Under the optimal conditions, the electrochemical behaviors of luteolin on HAp-CNT-CS/GCE were investigated by DPV. A good linear relationship of peak currents with the concentrations of luteolin ranging from 4.0×10^{-7} M to 1.2×10^{-5} M and a low detection limit of 8.0×10^{-8} M were obtained. This work opens a new way for the synthesis of HAp-CNT composite and broadens the application of the composite material.

Chapter 4: Hydroxyapatite Synthesis-triggered Reduction of Graphene Oxide under Moderate Temperature Environment and the Electrochemical Sensing Application of Their Composite

The reduced graphene oxide (rGO) is usually obtained by chemical reduction or thermal treatment. But these methods are either depending on toxic/hazardous reducing agents, or large energy consumption. In this chapter, we unexpectedly found that the *in-situ* synthesis of HAp on GO surface can trigger the reduction of GO. The process can be completed under a moderate temperature (85 °C) situation, without the assistance of any and extra reducing agent. Electrochemical assays further showed that the formed HAp-rGO nanocomposite exhibited an outstanding performance for electrocatalytic oxidation of hydrazine, due to the synergic effect of HAp with rich active site for hydrazine adsorption and rGO with large surface area and high electronic conductivity. When HAp-rGO modified electrode was utilized as an electrochemical for detection of hydrazine, wide linear ranges from 2.50×10^{-6} M to 2.56×10^{-4} M and from 2.56×10^{-4} M to 1.16×10^{-3} M, and low detection limit of 4.27×10^{-7} M were achieved. In addition, the sensor demonstrated an excellent anti-interference ability against common interfering species such as UA, AA, and Glu etc. Based on the above performance, satisfactory results were achieved when the sensor was utilized for hydrazine detection in real sample of industrial wastewater.

This study opens a new avenue for the synthesis of HAp-rGO composites and their electrochemical sensing application.

Chapter 5.2

Scope

Recently, much effort has been devoted to developing advanced materials with outstanding electrochemical properties to modify common working electrodes. HAp and HAp-based nanocomposite have many excellent properties such as easy preparation, stereoscopic structure, excellent biocompatibility, rich active sites, good ion-exchange and adsorption capacity, which enable them to be acted as advanced functional materials for electrochemical sensor fabrication.

In chapter 2, the author has synthesized pure nanoscale HAp and applied it as sensing material for the adsorption and voltammetric stripping analysis of four heavy metal ions. From the result, it was obtained that HAp nanoparticles can effectively adsorb metal ions by their rich active sites such as -OH and $-PO_4^{3-}$. However the weak electronic conductivity of HAp inhibits the electrochemical response intensity during analysis. But this also inspired a new idea to us, i.e., relying on the strong adsorption ability of HAp toward metal ions and its porous structure characteristic, the composites of metal/metal oxides/metal sulfides and HAp could be synthesized through two steps. First, the HAp is utilized as adsorbant for metal ions, especially the transition metal ions, then the hybrid material of metal ion/HAp can be further calcined to transfer the metial ions to the metal/metal oxides/metal sulfides nanoparticles under different conditions. Thus the nanocomposites of HAp with metal/metal oxides/metal sulfides are obtained. Then based on the excellent electronic conductivity of metal/metal oxides/metal sulfides in the composites, the electrochemical property of HAp can be further enhanced.

In addition, the single-component of HAp is redox-inactive in electrochemistry since it has not redox-active element, which limits its application in electrocatalysis. But when the electroactive metal/metal oxides/metal sulfides were doped into the HAp,

the excellent electroactivity of these metal-based materials such as Ni, NiS, CuO, CuSm MnO$_2$ coulping with good biocompatibility of HAp will enable the composites to be used as electrocatalyts for the non-enzymatic detection of some small biomolecules such as H$_2$O$_2$, dopamine, uric acid, and so on, which will dramatically broaden the application of the HAp-based nanomaterials. To verify this experimental idea, further experimental are required.

In Chapters 3-4, the author prepared HAp-CNT and HAp-GR composites. Due to the synergy of between HAp and the carbon nanomaterials (CNT and GR), the composites could greatly increase the electrochemical signals of drug molecule luteolin and organic pollutant hydrazine. However, in these systems, the good biocompatibility of HAp has not been fully considered and utilized. Therefore in the future research, more HAp-based nanocomposites are planned to be synthesized through hybridizing with other functional materials such as gold nanoparticles, carbon nanomaterials, and so on. Then using these materials as sensing materials to detect the biological macromolecules such as redox-proteins (hemoglobin, myohemoglobin), enzymes (glucose oxidase, horse radish peroxidase), and DNA.

Acknowledgments

Appendix

List of Figures

Chapter 3

Chapter 4

Fig. 4.2, Raman spectra of GO (a), HAp-rGO (b) and HAp (c).

Fig. 4.3 FT-IR spectra of GO (a), HAp-rGO (b) and HAp (c).

Fig. 4.4 TEM images of pure GO (A), HAp (B) and synthesized HAp-rGO (C).

Fig. 4.5 UV-vis absorption spectra of GO and rGO-HAp dispersion. Inset is the electronic photos of aqueous dispersion of GO and rGO-HAp.

Fig. 4.6 CVs of (a) bare GCE, (b) HAp-rGO-CS/GCE, (c) GO-CS/GCE and (d) HAp-CS/GCE in 1 mM $(Fe(CN)_6)^{3-/4-}$ solution containing 0.1 M KCl.

Fig. 4.7 Nyquist plots of (a) bare GCE, (b) HAp-rGO-CS/GCE, (c) GO-CS/GCE and (d) HAp-CS/GCE in 1 mM $(Fe(CN)_6)^{3-/4-}$ solution containing 0.1 M KCl. Inset shows the corresponding electrical equivalent circuit during electrochemical impendence spectra tests.

Fig. 4.8 (A) CVs and (B) the corresponding current values (at 0.8 V) of GO-CS/GCE (a', a,), HAp-CS/GCE (b', b,), HAp-rGO-CS/GCE (c', c,) in 25 mM PBS (pH 7.0) containing 0 (a, b, c) and 0.2 mM hydrazine (a', b', c') at scan rates of 0.1 V s^{-1}.

Fig. 4.9 (C) Chronoamperometric curves of GO-CS/GCE (a), HAp-CS/GCE (b) and HAp-rGO-CS/GCE (c) in 25 mM PBS (pH 7.0) upon injection of hydrazine. Inset of (C) is the response time of a single injection of hydrazine.

Fig. 4.10 (A) Chronoamperometric response of HAp/GO-CS/GCE in 25 mM PBS (pH 7.0) without (a) and with (b) of various concentration (from 0.10 to 0.80 mM) of hydrazine at the applied potential of 0.55 V. (B) The plot of I_{cat} vs. $t^{-1/2}$. (C) The plot of I_{cat}/I_L vs. $t^{1/2}$.

Fig. 4.11 Amperometric current response of HAp/GO-CS/GCE at different potentials in 0.1 M NaOH with successive addition of 0.2 mM H_2O_2. The insert reveals the sensitivity of different potentials.

Fig. 4.12 (A) Chronoamperometric responses of HAp-rGO-CS/GCE 25 mM PBS (pH 7.0) upon successive additions of hydrazine at the applied potential of 0.55 V. (B) Calibration plots of catalytic current (I) with the concentration of hydrazine (C).

Fig. 4.13 Chronoamperometric responses of the HAp-rGO-CS/GCE on the successive addition of 0.01 mM hydrazine (twice), 0.01 mM H_2O_2, 0.01 mM glucose, 0.01 mM glutathione (GSH), 0.01 mM dopamine (DA), 0.01 mM urea, 0.01 mM ethanol, 0.01

mM methanol, 0.01 mM ascorbic acid (AA), 0.01 mM acetic acid (AcA), 0.01 mM formic acid, 0.01 mM citric acid (CA), 0.01 mM uric acid (UA) and 0.01 mM hydrazine (twice) into PBS (7.0) at 0.55 V.

Fig. 4.14 Test stability of HAp-rGO-CS/GCE in hydrazine solution for 5000 s. Inset is the current retention ratio (I/I_0) for hydrazine detection after storage of the sensor for different period.

Fig. 4.15 Chronoamperometric curve of HAp-rGO-CS/GCE in 25 mM PBS (pH 7.0) upon injection with filtrated industrial wastewater and hydrazine standard solution. Inset shows the corresponding standard addition curve for determination of hydrazine in real sample.

List of Tables

List of Schemes

Chapter 1

Scheme 1.1 Illustration for the constitution and working principle of an electrochemical sensor.

Chapter 3

Scheme 3.1 Diagram for the transformation process from CaPP-CNT to HAp-CNT with the assist of alkaline phosphatase.

Scheme 3.2 Chemical structure and oxidation mechanism of luteolin.

Chapter 4

Scheme 4.1 Diagram for the synthesis process of HAp-rGO.

Scheme 4.2 Diagram for the application of HAp-rGO for electrochemical sensing detection of hydrazine.

List of Publications

Original Papers

(1) Alkaline phosphotase mediated synthesis of carbon nanotube-hydroxyapatite nanocomposite and its application for electrochemical determination of luteolin

<u>F. Gao</u>, X. Chen, H. Tanaka, A. Nishitani, Q. Wang,

Advanced Power Technology, **27**, 921-928 (2015).

(2) Rod-like hydroxyapatite and Nafion nanocomposite as an electrochemical matrix for simultaneous and sensitive detection of Hg^{2+}, Cu^{2+}, Pb^{2+} and Cd^{2+}

<u>F. Gao</u>, N. Gao, A. Nishitani, H. Tanaka

Journal of of Electroanalytical Chem., Vol. **775**, 212-218 (2016).

(3) Hydroxyapatite/chemically reduced graphene oxide composite: Environment–friendly synthesis and high-performance electrochemical sensing for hydrazine

<u>F. Gao</u>, Q. Wang, N. Gao, Y. Yang, F. Cai, M. Yamane, F. Gao, H. Tanaka

Submitted to *Biosensors and Bioelectronics,* **97**, 238-245 (2017).

Related Papers

(1) An Electrochemical sensor for gallic acid based on Fe_2O_3/electro-reduced graphene oxide composite: Estimation for the antioxidant capacity iIndex of wines

F. Gao, D. Zheng, H. Tanaka, F. Zhan, X. Yuan, F. Gao, Q. Wang

Materials Science and Engineering C, **57**, 279-287 (2015).

(2) A sensitive DNA biosensor using graphene oxide as the multi-site platform for probe DNA immobilization

F. Gao, X. Cai, H. Tanaka, Q. Zhu, F. Gao, Q. Wang

Journal of the Electrchemical Society, **162**, B291-B297 (2015).

(3) Graphene oxide directed in-situ deposition of electroactive silver nanoparticles and iIts electrochemical sensing application for DNA analysis

N. Gao, F. Gao, S. He, Q. Zhu, J. Huang, H. Tanaka, Q. Wang

Analytica Chimica Acta, **951**, 58-67 (2017).